Sister Rod Destructive Examinations (FY19)

Spent Fuel and Waste Disposition

Prepared for
US Department of Energy

Spent Fuel and Waste Science and Technology

Oak Ridge National Laboratory
Rose Montgomery, Robert N. Morris, Ralph Ilgner, Benjamin Roach Jy-An Wang, Zachary Burns, James T. Dixon, Stephanie M. Curlin

September 27, 2019

M2SF-19OR010201026

ORNL/SPR-2019/1251 Revision 1

This report was prepared as an account of work sponsored by an agency of the United States Government. Neither the United States Government nor any agency thereof, nor any of their employees, makes any warranty, express or implied, or assumes any legal liability or responsibility for the accuracy, completeness, or usefulness of any information, apparatus, product, or process disclosed, or represents that its use would not infringe privately owned rights. Reference herein to any specific commercial product, process, or service by trade name, trademark, manufacturer, or otherwise, does not necessarily constitute or imply its endorsement, recommendation, or favoring by the United States Government or any agency thereof. The views and opinions of authors expressed herein do not necessarily state or reflect those of the United States Government or any agency thereof.

SUMMARY

This report documents work performed under the Spent Fuel and Waste Disposition, Spent Fuel and Waste Science and Technology program for the US Department of Energy (DOE) Office of Nuclear Energy (NE). This work was performed to fulfill Level 2 Milestone M2SF-19ORO010201026 within work package SF-19OR01020102 and is an update to the work reported in M2SF-19OR010201028 and M3SF-19OR010201027. The document incorporates comments received with respect to the previous reports and incorporates additional test results.

As a part of the US Department of Energy (DOE) Office of Nuclear Energy (NE) High Burnup Spent Fuel Data Project, Oak Ridge National Laboratory (ORNL) is performing destructive examinations (DEs) of high burnup (HBU) (>45 gigawatt days per metric ton uranium) spent nuclear fuel (SNF) rods from the North Anna Nuclear Power Station operated by Dominion Energy. The SNF rods, called the "sister rods," are all HBU and include four different kinds of fuel rod cladding: standard Zircaloy-4 (Zirc-4), low-tin Zircaloy-4 (LT Zirc-4), ZIRLO®, and M5®. The DEs are being conducted to obtain a baseline of the HBU rod's condition prior to dry storage and are focused on understanding overall SNF rod strength and durability. Both composite fuel and empty cladding will be tested to derive material properties. While the data generated can be used for multiple purposes, a primary goal for obtaining the post-irradiation examination data and the associated measured mechanical properties is to support SNF dry storage licensing and relicensing activities by (1) addressing identified knowledge gaps and (2) enhancing the technical basis for post-storage transportation, handling, and consolidation activities.

This report documents the status of the ORNL Phase I DEs of 8 sister rods and outlines the DE tasks performed and the data collected to date, as guided by the sister rod test plans. The DEs are performed using a phased approach, and the Phase 1 DEs being performed at ORNL include:

- full-length rod heat treatments (FHT) of 3 selected sister rods to examine the effects of temperatures reached during dry storage preparation,
- rod internal pressure and void volume measurements of the 3 FHT rods and 3 corresponding baseline rods, as well as 2 additional rods selected for depressurization/gas transmission tests and fatigue lifetime tests,
- fission gas sampling and analysis,
- depressurization and gas transmission tests,
- rough segmentation of the selected rods for mechanical tests and rod characterization,
- fuel sampling and burnup analysis,
- metallography,
- cladding total hydrogen measurements,
- mechanical testing, including fatigue lifetime (CIRFT), four-point bend, axial tension, microhardness, ring compression, and burst tests.

Table S-1 provides a summary of the DE status. The mechanical testing will be performed using fueled segments and is expected to complement previous and current mechanical test results using defueled cladding segments.

Table S-1. DE Status.

Planned DE		Status	Comments
FHT	Heat treat whole rods to 400°C, cool at ≤5°C/hr 1 ZIRLO, 1 M5 and 1 Zirc-4 rod	Complete	Three fuel rods have been heat-treated: one Zirc-4-clad (F35P17), one ZIRLO-clad (3F9N05), and one M5-clad (30AE14) rod. The target heat-up rates, soak temperatures and times, and cool-down rates were successfully achieved with the exception of the spent fuel rod heat treatment oven (SFRHTO) Zone 1 for rod 30AE14 (the upper ~550 mm), which reached temperatures as high as 485°C for approximately 1.75 h during the thermal soak. 30AE14's Zone 1 average temperature during the soak period was 452°C. At the higher average temperature imposed, the pressure was ~7.6 MPa, about 8% higher than planned. The maximum pressure during the soak was estimated as 8.0 MPa at the 485°C peak temperature for ~1.75 h. The rod's temperature was corrected prior to cool-down, and cool-down was as expected.
RS	Segment 3 baseline and 3 FHT rods, and segment 1 additional ZIRLO rod to provide additional CIRFT specimens.	Complete	Initial test segments have been rough cut from 7 Phase 1 sister rods and placed into individual storage capsules. The segments are taken from the initial 4 baseline rods (1 of which provides additional ZIRLO CIRFT specimens only) and 3 heat-treated rods. The rough segments are stored in labeled aluminum capsules in the hot cell; they are not stored in an inert gas atmosphere. The segments are further sectioned in preparation for testing as needed.
DEF	Defuel segments for ANL	Complete	Twelve segments slated for testing at Argonne National Laboratory (ANL) have been defueled and shipped.
AERO	Collect aerosol particles released during selected tests	In progress	An aerosol collection system with fixturing and sampling devices was designed to characterize and quantify the respirable fraction of UO_2 particles released during rod fracture. The fixture is used in conjunction with four-point bend tests. The aerosol collection system is currently being tested out of cell and is expected to be ready for use when four-point bend tests begin.
DE.01	Measure internal pressure of 5 baseline and 3 heat treated rods	Complete	The rod internal pressure and the void volume available inside the rod were measured for 8 sister rods at room temperature, and all pressures are within the publicly available database envelope. There is a clear correlation between the post-irradiated rod internal pressure and the as-designed fill pressure. The fission gas partial pressure trends well with the rod average burnup. The pressure and void volumes measured are consistent for rods from the same fuel vendor. The product of the partial pressure of the

Planned DE		Status	Comments
			fission gas and the void volume, P_fV, is consistent from lab to lab for sister rods from the same assembly, except for the two rods from assembly F35. A comparison of P_fV indicates the ZIRLO-clad rods may have experienced some change in pressure, void volume, or both due to the heat treatment applied, but the M5-clad rods do not exhibit the same effects. Comparisons with predictions from fuel rod performance codes FAST and BISON indicate a tendency for FAST to underpredict pressure and BISON to overpredict pressure.
	Measure rod void volume of 5 baseline and 3 heat treated rods	Complete	Eight rods have been measured. All measured volumes are on the lower side of the publicly available database envelope but are consistent with other rods of their design type. Comparing the measured volumes of the baseline and heat-treated ZIRLO-clad rods, as well as the P_fV for all ZIRLO-clad sister rods, it appears that the heat treatment resulted in an increase in void volume. The heat-treated M5-clad rod is within measurement uncertainty of the baseline rod, and the heat-treatment did not appear to affect the void volume. No conclusions could be made about the effects of the heat-treatment on the Zirc-4-clad rod based on a comparison with the LT Zirc-4 baseline rod or the PNNL Zirc-4-clad rod. Comparisons with predictions from fuel rod performance codes FAST and BISON indicate a tendency for FAST to overpredict void volume and BISON to underpredict void volume.
	Measure the transmissibility of gas along the pellet stack	Complete	Pellet stack gas transmissibility at room temperature was measured using depressurization tests on eight rods and transmission tests on three rods. In all cases, gas was transmissible through the pellet stack at room temperature, requiring between 30 min and 24 h to reach equilibrium conditions, depending upon the pressure differential applied. The data correlates well using the Muskat-Poiseuille porous media method. The permeability of the pellet stack varied over less than an order of magnitude for this set of rods and may indicate some common feature about HBU fuel. Graphs of the data with burnup, lifetime maximum HDCI, and operating lifetime average assembly middle-of-cycle predicted fuel temperature appear to indicate that the derived permeability is correlated to fuel operating temperature and maximum HDCI but is not correlated to the rod average burnup. The permeability does appear to be closely related to the rod's manufacturer and it seems that the pellet

Planned DE		Status	Comments
			manufacturing process may be important in determining the permeability of the pellet stack. While the flow regimes associated with the pellet stack transmissibility did not change significantly for the heat-treated fuel rods, it appears that the heat treatments may have induced a shift to higher evaluated permeability. The role of the cladding in the resulting permeability shift is unclear.
	Collect fission gas samples and analyze	Complete	Fission gas samples have been collected and analyzed. Results are consistent with publicly available database. Code-predicted fission gas production is not available; therefore, the fission gas release ratio is not available. ORNL and Pacific Northwest National Laboratory (PNNL) fission gas analyses are consistent with one another, and the data are as expected when differences in fission gas partial pressure are considered.
DE.02	Perform optical microscopy (MET)	In progress	Fueled and defueled specimens are being prepared for MET views. The Phase 1 specimens have been cut and specimen preparation/polishing is in progress. Cladding/pellet views are available of 1 M5-clad baseline rod, 1 M5-clad heat-treated rod, 1 heat-treated ZIRLO-clad rod, and 1 heat-treated Zirc-4 rod. Although some of the views are not as polished as intended, it is possible to see the cladding hydrides and fuel pellet high burnup (HBU) rims. Radial hydrides are visible in the heat-treated M5 and ZIRLO cladding and some radial hydrides located at the cladding inner diameter may have nucleated at a pellet crack. Measurements of the waterside oxide, pellet-side oxide, remaining cladding thickness, and HBU pellet rim are provided for the specimens available.
DE.03	Measure hydrogen content	In progress	Specimen preparation is in progress, and it involves dissolving the fuel from the cladding. A dissolution column has been designed and installed in the Irradiated Fuels Examination Laboratory (IFEL) hot cell and 13 specimens have been defueled.
DE.05	Perform CIRFT tests to determine static, dynamic, and cumulative effects and fatigue lifetime	In progress	Tests using the Cyclic Integrated Reversible-Bending Fatigue Tester (CIRFT) were completed on 13 specimens. The preliminary results indicate that the baseline sister rod's fatigue lifetime is consistent with other rods of the same type that were tested in the past. The 17x17 sister rods fall on the lower side of the existing CIRFT database.

Planned DE		Status	Comments
			It appears that the heat treatments resulted in a shorter fatigue lifetime, as the results for the heat-treated rods resulted in a shorter fatigue lifetime for all three heat-treated test specimens. A test on a specimen with a grid-to-rod-fretting (GTRF) mark in the maximum strain location did not result in a reduced fatigue lifetime. A specimen having multiple pellet-pellet gaps will be tested to determine if they have an impact on the fatigue lifetime. The initial flexural rigidity measured for the sister rods are consistent with previously tested 17x17 specimens and do not appear to be a function of burnup, at least over the range of available data. Data reduction on the available test datasets is in progress. Specimens from other Phase 1 sister rods are being prepared. The cumulative effects test fixture is being evaluated out of cell.
DE.07	Conduct 4-point bend tests	Not started	The Instron load frame has not yet been installed into the hot cell. All preparatory activities, including calibration and verification tests are complete.
DE.08	Conduct axial tensile tests	Not started	The Instron load frame has not yet been installed into the hot cell. All preparatory activities, including calibration and verification tests are complete.
DE.09	Test for ASTM microhardness	Not started	The microhardness tester has been installed and is ready to begin testing. Specimen preparation is in progress.
DE.10	Conduct RCTs	Not started	The Instron load frame has not yet been installed into the hot cell. All preparatory activities, including calibration and verification tests are complete.
DE.14	Perform burst tests	Not started	The existing in-cell equipment that was proposed for this purpose was evaluated and it was found that it is not capable of reaching predicted burst pressures at the temperatures of interest. Additional equipment will need to be developed to perform in-cell burst tests on fueled specimens.

This page is intentionally left blank.

ACKNOWLEDGMENTS

Many thanks to our US Department of Energy Office of Nuclear Energy sponsor, Ned Larson, along with the Spent Fuel and Waste Science and Technology (SFWST) storage and transportation program leadership for their continued support. We are particularly grateful for the invaluable support, guidance, and leadership of Bruce Bevard and John Scaglione of the Oak Ridge National Laboratory (ORNL) Used Fuel Systems team. The sister rod project would not have been possible without the vision and support of the Electric Power Research Institute, Westinghouse, Framatome, and Dominion Energy.

This work would not have been possible without the support and expertise provided by the leadership and staff members of the ORNL's Irradiated Fuel Examination Laboratory (IFEL). Special thanks go to Jerid Metcalf, Scott Thurman, John Hinds, and Brian Woody for their assistance with in-cell testing activities. Rick Henry has the unenviable task of tracking the bits and pieces of sister rods, their moves around the hot cell, and to other facilities, and we very much appreciate his patience and continued support. Mark Delph, Russ Smith, and Ryan Schultz have been vital in supporting the deployment of new equipment to the cell, and we appreciate their continued support.

We are grateful to Chuck Baldwin of the IFEL for his support on the sister rod project and for his dedicated efforts in training the next generation of IFEL staff members. Special thanks go to Tyler Smith for his work developing a dissolution column for the sister rod fuel material. We appreciate his continuing support, and the ongoing efforts from Lindsey Aloisi to defuel the many small specimens required for total cladding hydrogen and metallographic studies. We also appreciate Tracy Binger's efforts measuring and tracking the defueled cladding radiation levels in support of releasing the specimens to ORNL Low Activation Materials Development and Analysis (LAMDA) lab. Our appreciation and thanks are extended to Josh Schmidlin and the staff of LAMDA lab for their continuing support on the sister rod metallography and total hydrogen measurements.

Ricardo Muse and Jason Braden have supported the fabrication and rapid prototyping jobs associated with the sister rod project and we appreciate their continued patience.

We also very much appreciate Darren Skitt and would like to thank him for the long hours spent photographing fractured sister rod fatigue test specimens.

Ben Garrison has been indispensable to the team in augmenting and testing the load frame for use in mechanical testing the sister rod specimens. Drew Walker and Don Erdman were also essential in the development of radiation tolerant instrumentation for the load frame and we appreciate their continuing support. Danny Parrott, Tony McBee, and the staff members of the ORNL Instrumentation and Controls team provided custom radiation tolerant cables for the much of the hot cell equipment being used by the sister rod project.

We would also like to thank the staff of the Nuclear Analytical Chemistry and Isotopics Laboratory for their work analyzing the sister rod fission gas samples and defueling the sister rod specimens. Particular thanks go to Jeff Delashmitt, Doug Canaan, and Joe Giaquinto for their efforts. Thanks also to Ben Rothrock and his efforts on behalf of the sister rod project.

We are grateful for the advice and continuing support provided by M. D. Cheng of the ORNL Environmental Sciences Division in the area of aerosol collection.

The ORNL Used Fuel Systems team is indebted to Kory Linton and the ORNL Nuclear Fuel Materials team for providing their team's support and expertise on a variety of topics.

Thanks go to Tracy Binger and Mark Walls for their quick support when radiation protection coverage is required.

The expertise and fabrication capabilities provided by Charles Blue and Randall Blue of Infrared Heating Technology (Oak Ridge, TN) were vital to the development and deployment of the full-length rod heat treatment oven.

Much appreciation is extended to our technical, editorial, and administrative reviewers, Jianwei Hu, Jason Harp, Rose Raney, and Andrea Beatty. Without their keen reviews, this document would have been much less precise.

Finally, we would like to express our gratitude to Ken Geelhood of PNNL for his detailed review of the rod internal pressure, void volume, and fission gas release data and the additional verification calculations he performed using FAST.

CONTENTS

LIST OF FIGURES

This page is intentionally left blank.

LIST OF TABLES

This page is intentionally left blank.

REVISION HISTORY

Date	Changes
3/29/2019	Initial release
9/27/2019	Revised to include additional data and incorporate comments from the previously released report.

This page is intentionally left blank.

ACRONYMS

BOL	beginning of life
CIRFT	cyclic integrated reversible-bending fatigue tester
DE	destructive examination
DOE	US Department of Energy
EPRI	Electric Power Research Institute
FHT	full-length fuel rod heat treatment
FY	fiscal year
GTRF	grid-to-rod fretting
HBU	high burnup
HDCI	high duty core index
ID	inner diameter
IFBA	Integral Fuel Burnable Absorber
IFEL	Irradiated Fuels Examination Laboratory
LT	low tin
LVDT	linear variable differential transformer
MET	metallography
NE	Office of Nuclear Energy
NDE	nondestructive examination
OD	outer diameter
ORNL	Oak Ridge National Laboratory
PCI	pellet-cladding interaction
PVC	polyvinyl chloride
PWR	pressurized water reactor
REDC	Radiochemical Engineering Development Center
RPC	Research Project Cask
RS	rough segmentation
SEM	scanning electron microscope
SFRHTO	spent fuel rod heat treatment oven
SFWD	Spent Fuel and Waste Disposition
SFWST	Spent Fuel and Waste Science and Technology
SNF	spent nuclear fuel
SRSS	square-root-sum-square
TEM	transmission electron microscope
UE	uniform elongation
VVER	water-water energetic reactor

This page is intentionally left blank.

SPENT FUEL AND WASTE SCIENCE AND TECHNOLOGY SISTER ROD DESTRUCTIVE EXAMINATIONS

1. INTRODUCTION

As a part of the US Department of Energy (DOE) Office of Nuclear Energy (NE) High Burnup Spent Fuel Data Project, Oak Ridge National Laboratory (ORNL) is performing destructive examinations (DEs) of high burnup (HBU) (>45 gigawatt days per metric ton uranium) spent nuclear fuel (SNF) rods from the North Anna Nuclear Power Station operated by Dominion Energy. The goals of the High Burnup Spent Fuel Data Project are to "provide confirmatory data for model validation and potential improvement, provide input to future spent nuclear fuel dry storage cask design, support license renewals and new licenses for Independent Spent Fuel Storage Installations, and support transportation licensing for high burnup SNF" [1]. The SNF rods, called the "sister rods," are all HBU and include four different kinds of fuel rod cladding: standard Zircaloy-4 (Zirc-4), low-tin Zircaloy-4 (LT Zirc-4), ZIRLO®, and M5® [2,3]. The sister rods have similar characteristics to SNF that will be placed in dry storage in a modified TN-32B cask because they have been extracted from assemblies with the same design and similar operating histories (symmetric partners) or from the actual fuel assemblies that will be included in the TN-32B cask[1]. Details about the sister rods, their operation in the North Anna Nuclear Power Station, and the high burnup spent fuel data project are provided in References 1 through 4.

The 25 sister rods were subjected to nondestructive examinations (NDEs) at ORNL's Irradiated Fuels Examination Laboratory (IFEL) as described in Montgomery et al. (2018) [4]. The NDEs included detailed visual and dimensional inspections, gamma scanning, eddy current, and rod surface temperature measurements. Following the NDEs, 10 of the 25 sister rods were shipped from ORNL to Pacific Northwest National Laboratory for defueled cladding mechanical tests. Several cladding segments from ORNL's sister rods were defueled for shipment to Argonne National Laboratory (ANL).

The DEs are being conducted to obtain a baseline of the HBU rod's condition prior to dry storage and to investigate specific conditions of dry storage through small scale and separate effects tests. The testing performed is focused on understanding overall SNF rod strength and durability. Both composite fuel and empty cladding will be tested to derive material properties. While the data generated can be used for multiple purposes, a primary goal for obtaining the post-irradiation examination data and the associated measured mechanical properties is to support SNF dry storage licensing and relicensing activities by (1) addressing identified knowledge gaps and (2) enhancing the technical basis for post-storage transportation, handling, and consolidation activities.

The 15 rods available at ORNL for DE are described in Table 1. The planned DEs include full-length rod heat treatments simulating the peak dry storage cladding temperature, rod internal pressure and void volume measurements, fission gas analysis and release ratios, fuel burnup, gas transmission testing, metallography, cladding total hydrogen measurements, four-point bend and axial tension tests, microhardness tests, ring compression tests, and burst tests. The mechanical testing will be performed using fueled segments and is expected to complement previous and current mechanical test results using defueled cladding segments.

[1] With the exception of the Zirc-4 rods taken from assembly F35 and the LT Zirc-4 rods taken from assembly 3A1; these rods are not exact sister rods to any rods in the dry storage cask but were the closest available. Further it should be noted that assembly F35 was operated as a test assembly and was irradiated for 4 cycles of operation to high burnup.

The DE scope necessarily includes preparatory tasks such as rod segmenting, defueling, and heat treatments, and those activities are discussed within this report.

Throughout this document the following terms are used:

- Rod: the full-length sister rod, unpunctured or punctured, but not segmented, with the exception that a rod used for gas transmission testing (lower end cap removed only) can continue to be called a rod
- Segment: a length of cladding with pellets that has been cut from the parent rod to be further modified for use in examinations
- Specimen: a segment that has been modified for use in a DE
- Sample: a small portion of material taken from a segment or specimen for local property testing

The DEs are performed using a phased approach, as described by Saltzstein [2]. This report documents the status of the ORNL Phase I DEs and outlines the DE tasks performed and the data collected to date, as guided by the sister rod test plans [2,3]. Testing is performed and documented per the requirements of the ORNL sister rod test plan [3], which includes applicable consensus standards (e.g., American Society for Testing and Materials), regulatory requirements (e.g., Department of Energy orders), and adherence to the laboratory and Fuel Cycle Technologies quality assurance plans. In compliance with the ORNL sister rod test plan, Measuring and test equipment necessary to conduct the examinations is controlled and calibrated at the facilities performing the work in accordance with approved laboratory procedures.

Unless otherwise specified, examinations were completed at ambient temperature at standard pressure in air, including those using heat-treated specimens. Throughout the remainder of this document the sister rods will be described using the format XXXYYY, where XXX represents the fuel assembly ID and YYY represents the rod lattice position within the assembly. Individual sister rod segments are described using the format XXXYYY-RRRR-TTTT where XXXYYY is the sister rod ID as previously described, RRRR is the lowest original rod elevation of specimen, and TTTT is the upper original rod elevation of the segment. If segments longer than 50 mm are subdivided to provide additional test specimens, the ID is further adjusted to reflect the rod elevations originally occupied by the specimen. This nomenclature is intended to provide traceability to the elevation on the sister rod where each specimen originated.

Table 1. Sister rods selected for destructive examination at ORNL [3]

Clad material	Sister rod	Rod average burnup (GWd/MTU)	Assembly average burnup (GWd/MTU)	Assembly operation	Key characteristics	Cask-stored sister(s)	
						Assembly identifier	*Cask rod lattice location*
M5	30AG09	53	52.0	30A was operated hot-hot-cold. Its last cycle was uprated in the last quarter, making it the cycle with the highest power density of those represented. This assembly had the highest pellet enrichment. The assembly design included mid-span mixing grids which should have lowered the rod operating temperature in the hot spans somewhat. All of the M5 rods are expected to have relatively low rod internal pressure and cladding hydrogen content.	Sister rod to assembly rod in assembly 57A lance position with close proximity to the peak (hottest) cask rod position (I-7). The rod was operated in a guide tube adjacent location. Of the sister rods, predicted to have the highest decay heat.	57A	I07
M5	30AK09[a]	54			The corresponding cask rod is next to a lance position with close proximity to the peak (hottest) rod position (I-7) in the cask	57A	I07
M5	30AD05[a]	54			D-5 & E-14 were operated in a guide tube adjacent location with (E-14) and without (D-5) burnable poisons. Because the poisons influence power output during irradiation, the rods are expected to have different characteristics, even though they have burnups that are similar	57A	E14
M5	30AE14[b]	54				57A	D05
M5	5K7O14	53	53.3	5K7 was operated hot-hot-cold and had the highest pellet enrichment of the assembly batches represented. The assembly design included mid-span mixing grids, which should have lowered the rod operating temperature in the hot spans somewhat.	Approximately average assembly burnup; the rod was operated in a GUIDE TUBE diagonal location. All of the M5 rods are expected to have relatively low rod internal pressure and cladding hydrogen content.	5K6 3K7 5K1	C04
ZIRLO	6U3I07	54	52.7	6U3 was operated hot-cold-cold. The 6U3 sister rods are expected to have relatively high rod internal pressure and cladding hydrogen contents.	This rod is a sister to three different fuel assemblies in the central, middle, and outer regions of the RPC basket. The rod was operated in a guide tube adjacent location.	3U4 3U9 3U6	I07 I11 I11
ZIRLO	6U3M09	55			This rod's cask sister is next to a lance position	3U4 3U9 3U6	E09
ZIRLO	6U3K09[a]	55			This rod's cask sister is next to a lance position	3U4 3U9 3U6	K09

Table 1. Sister rods selected for destructive examination at ORNL (continued)

Clad material	Sister rod	Rod average burnup (GWd/MTU)	Assembly average burnup (GWd/MTU)	Assembly operation	Key characteristics	Cask-stored sister(s)	
ZIRLO	3F9N05[b]	54	52.3	3F9 was operated hot-hot-cold. Both sister rods appear to have experienced grid-to-rod fretting in reactor; marks were observed at grid locations along the entire axial length. The 3F9 rods are expected to have moderately high rod internal pressure and cladding hydrogen content.	Rod is a good match for several cask rods with a relatively high burnup.	4F1 3F6 6F2	N05 N05 N05
ZIRLO	3F9D07	52			Rod having approximate average assembly burnup	4F1 3F6 6F2	D07
ZIRLO	3D8E14[a]	59	55.0	3D8 was operated hot-cold-cold. The 3D8 rods are expected to have moderate rod internal pressure and high cladding hydrogen content.	Rod having approximate highest burnup in assembly and the highest sister rod burnup.	5D9 5D5	N13 M04
ZIRLO	3D8B02	50			Rod having close to lowest burnup in assembly (selected based on pulling restriction).	5D9 5D5	B16 P16
LT Zirc-4	3A1B16	48	50.0	3A1 was burned hot and in only two cycles reached high burnups comparable to the other sister rods.	Rod having lowest burnup in assembly; close to assembly periphery	OA4[c]	B16
LT Zirc-4	3A1F05[a]	51			Rod having highest burnup in assembly; reasonably close to center of assembly. Areas of CRUD observed.	OA4[c]	F05
Zirc-4	F35P17[b]	60	57.9	Four cycles of operation. F35 operated its fourth cycle in D-bank with control rods partially inserted. Operated prior to North Anna's power uprates so lower power density. Lowest enrichment. At time of exams, predicted to have the lowest decay heat.	Rod located on the assembly periphery. Spalling oxide was observed. This rod is expected to have a high rod internal pressure combined with a relatively large cladding hydrogen content.	None (F40)[d]	N/A

[a] Phase 1 baseline rod.

[b] Phase 1 full length heat-treated rod.

[c] The LT Zirc-4 rods taken from assembly 3A1 are not exact sister rods to 0A4 but were the closest available.

[d] The Zirc-4 rods are not exact sister rods to F40 but were the closest available. Additionally, assembly F35 was operated as a test assembly and was irradiated for 4 cycles of operation to high burnup.

2. DESTRUCTIVE EXAMINATION SCOPE

The DE tasks in Phase 1 include the following [2,3]:

FHT:	Full-length fuel rod heat treatments of three sister rods (one ZIRLO, one M5, and one LT Zirc-4).
RS:	Rough segmenting of the rods for allocation of segments to DE. Segments are stored in aluminum capsules, in air, until the time of the test.
DEF:	Defueling of selected segments. Some segments are defueled as preparation for cladding-only DE; other segments are defueled to gather samples for fuel isotopic and burnup measurements.
AERO	Capture of aerosolized particles released from the segments where fracture occurs during testing (e.g., four-point bend); fixtures and sampling methods are developed to support this effort.
DE.01	Rod internal pressure measurement, rod void volume measurement, collection of fission gas specimens, gas transmission testing, fuel isotopics and burnup measurements.
DE.02	Metallography.
DE.03	Cladding total hydrogen measurements.
DE.05	Cyclic integrated reversible-bending fatigue tests (CIRFT) in static, dynamic, and cumulative test modes.
DE.07	Four-point bend tests.
DE.08	Axial tension testing.
DE.09	Microhardness tests.
DE.10	Ring compression tests (RCTs).
DE.14	Burst tests.

Each of the following sections provides details on the status and results of the DEs currently under way. DE.04, DE.06, DE.11, DE.12, and DE.13 have been deferred to later phases of the test program [2].

This page is intentionally left blank.

3. FULL-LENGTH FUEL ROD HEAT TREATMENTS (FHT)

In preparation for dry storage, the fuel assemblies and canister cavity must be drained and dried. Typically, the most challenging thermal condition experienced by the fuel during dry storage occurs either during the drying sequence or just after drying during transfer of the canister to the storage pad. To gain a better understanding of the effects of the drying and transfer sequence, three full-length sister rods were subjected to a simulated dry storage vacuum drying temperature distribution to examine the rod condition induced by the increased fuel rod temperature compared with the rod condition prior to dry storage [1,2,3].

The spent fuel rod heat treatment oven (SFRHTO), shown in Figure 1 was developed for FHT. The SFRHTO is capable of imposing a variety of expected axial temperature profiles and peak cladding temperatures up to 530°C on a full-length fuel rod. In contrast with heat treatment of rod segments where the full-length rod is depressurized and segments are cut, heat treating full-length fuel rods before depressurization preserves the as-received, as-irradiated internal pressure and induces the representative hoop stresses associated with bounding drying temperature conditions.

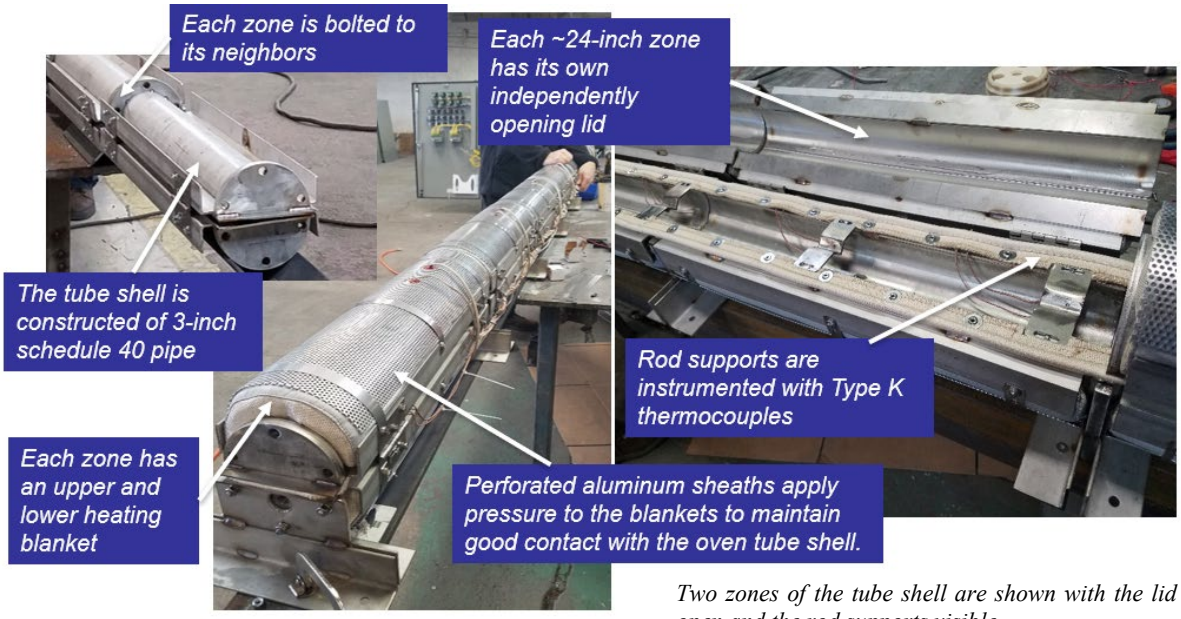

The SFRHTO tube shell with its seven modular zones. The power and thermocouple cables for the heating blankets are visible at the top center of each zone.

Two zones of the tube shell are shown with the lid open and the rod supports visible.

Figure 1. SFRHTO Configuration.

As discussed in the ORNL sister rod test plan [3], the sister rods selected for FHT were chosen based on two main criteria: (1) the likelihood of a relatively high amount of hydrogen in the cladding for that cladding type and (2) the predicted rod internal pressure. Past RCT testing at ANL [35] has identified these two parameters as important to hydride reorientation, which can degrade the load-bearing capability of the cladding under some conditions. The NDEs completed [4], particularly the eddy current examinations, confirmed that the selected FHT rods are expected to have among the highest oxidation and hydrogen pickup for rods of the same cladding type. Since rod internal pressure is not directly correlated to cladding oxidation and hydrogen pickup, the rod having the highest pressure is not necessarily the rod whose cladding has the highest hydrogen content. Therefore, specimen selections considered available analytical predictions of rod internal pressure.

The peak temperature to be applied to the full-length rods was selected as 400°C based on regulatory guidance regarding calculated peak fuel cladding temperatures for normal conditions of dry storage and short-term loading operations [5]. The full-length rods were heated slowly and held at temperature for several days, and then they were slowly cooled to ambient temperature.

As illustrated in Figure 2, the local temperature of the fuel rod cladding varies with axial elevation and based on the dry storage system; however, a flat 400°C was imposed at all axial locations for the FHT. The expected axial temperature distribution in the Research Project Cask (RPC) is also provided in Figure 2 for information [6]. The hydrogen content in the fuel rod cladding is expected to vary axially as well, with the highest cladding hydrogen concentrations located in the upper elevations where the cladding and coolant were hottest during reactor operation. Axial rod elevations where high hydrogen cladding concentration coincides with higher temperatures during storage are expected to be the most vulnerable to cladding degradation mechanisms such as hydride reorientation embrittlement, and those elevations of the sister rods are expected to provide representative performance data for HBU fuel storage conditions.

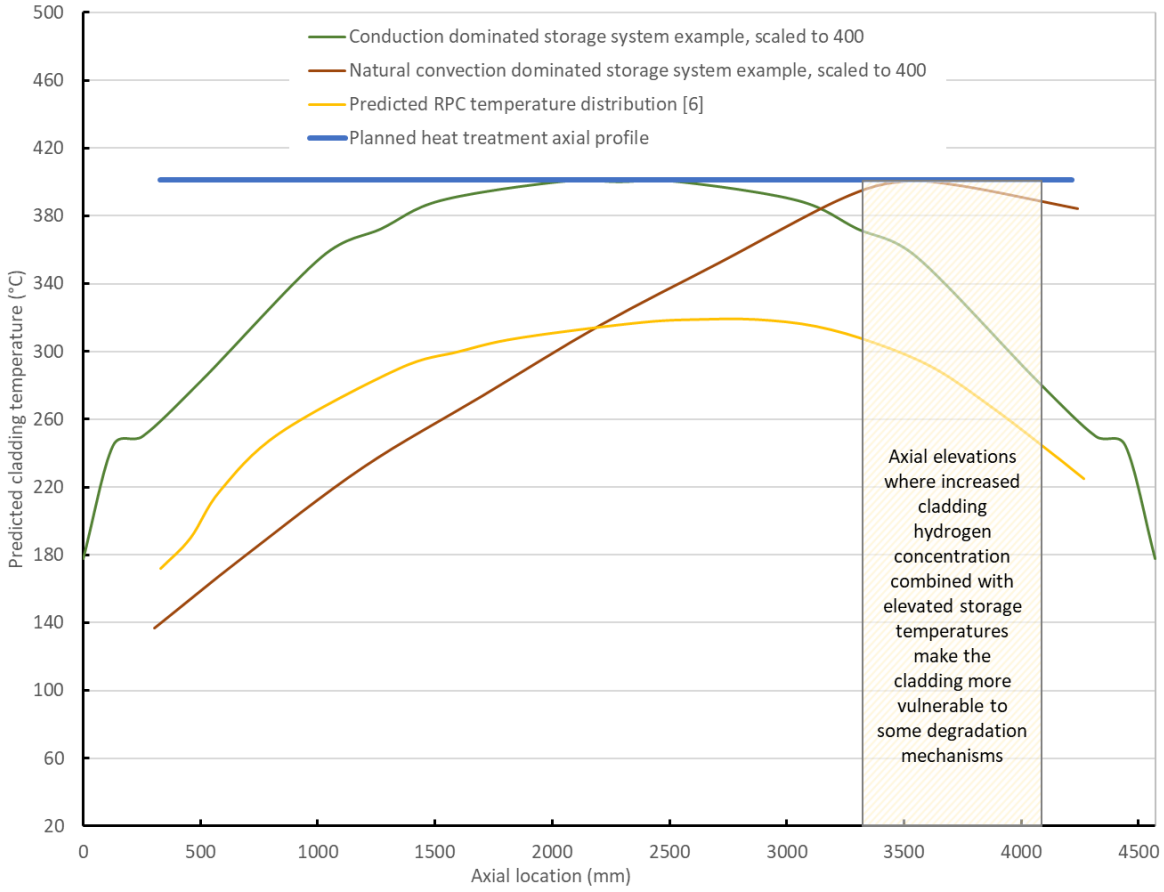

Figure 2. Illustration of Various Axial Profiles Associated with Dry Storage Systems and the Fuel Rod Expected Axial Hydride Density Trend.

While several different types of SNF dry storage systems are available, there are two basic designs with respect to heat transfer modes: a convection-based design and a conduction-based design. As illustrated in

Figure 2, the axial temperature profiles of the fuel in the storage systems differ in the location of the peak temperature and the quantity of fuel in the storage system at or near the peak temperature. As described by Salzstein [2], in an effort to reduce the number of variables that could cause variations in the behavior of the hydrides along the axis of the rod, the Spent Fuel and Waste Science and Technology (SFWST) program elected to implement a flat temperature profile for FHTs, with all rod elevations subjected to the peak temperature. The peak temperature for the heat treatment was selected based on the regulatory limit for the fuel rod cladding, 400°C.

The target heat-up and cool-down rates selected for the heat treatments are based on the rates measured for the RPC during the cask loading and vacuum drying sequence and are 10°C /h and 3.7°C/h, respectively. The SFWST program specified an 8 h hold time or *soak* at peak temperature to ensure that cladding hydrogen dissolution was complete, while minimizing the potential for annealing of irradiation defects that would tend to offset any effects of hydride reorientation-induced embrittlement. Figure 3 provides a graphical representation of the ideal timeline for the selected FHT.

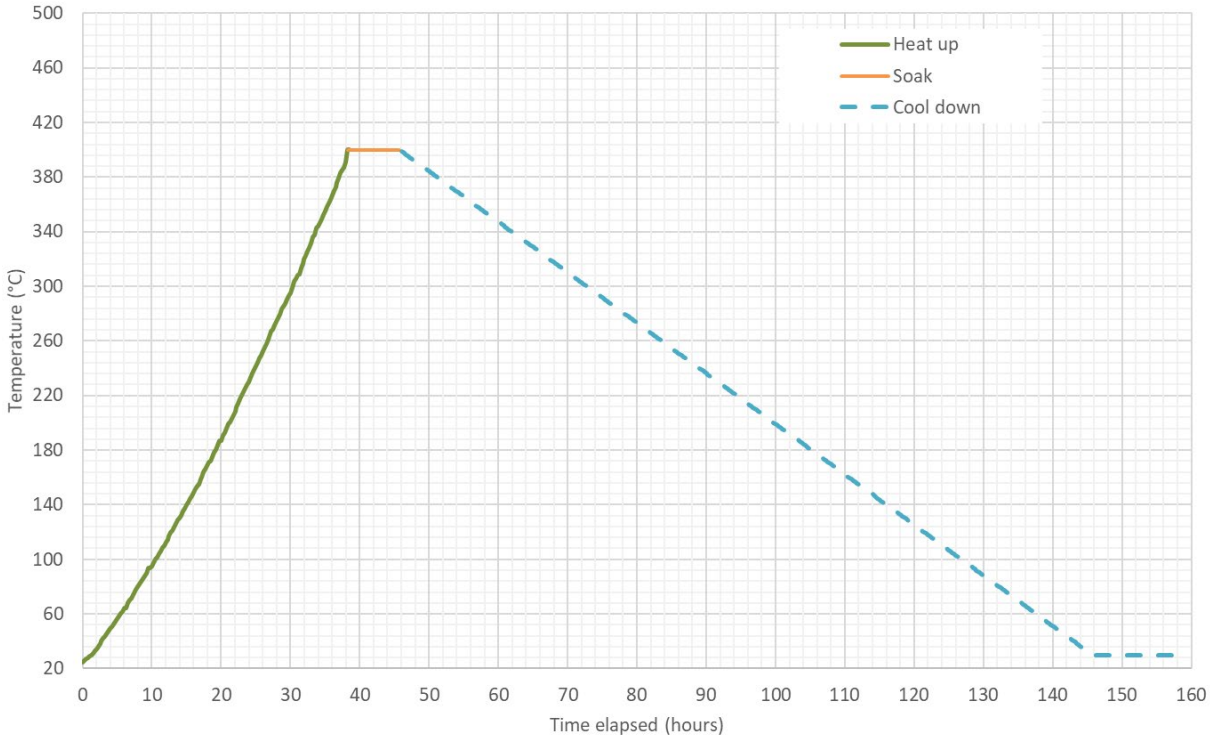

Figure 3. The Selected Heat Up and Cool Down Cycle for the Three Initial FHT Sister Rods.

3.1 Heat Treatments Applied

Three fuel rods have been heat-treated in the SFRHTO to date: one Zirc-4-clad (F35P17), one ZIRLO-clad (3F9N05), and one M5-clad (30AE14) unpunctured fuel rod. Figure 4, Figure 5, and Figure 6 provide the heat treatment history for each of the selected rods. Table 2 provides a summary of the heat treatment parameters.

As evidenced by the data, the target heat-up rates, soak temperatures and times, and cool-down rates were successfully achieved, with the exception of SFRHTO Zone 1 for rod 30AE14. During the heat treatment of 30AE14 (M5 cladding), the Zone 1 heating blanket controller malfunctioned, and that part of the fuel rod (the upper end cap, the plenum region, and ~200 mm of fuel stack at the top of the rod) reached temperatures as high as 485°C for approximately 1.75 h during the thermal soak. The average Zone 1 temperature during the 8 h soak period was 452°C (see Figure 6). The Zone 1 heating blanket controller was corrected before the end of the 8 h soak, and the average temperature was 401°C when cool-down began.

Table 2. Measured rod temperatures and heat-up/cool-down rates during the heat treatments.

Rod	SFRHTO Zone	Approximate Rod Elevations (mm)	Heat up rate (°C /h)	Cooldown rate (°C /h)	Average soak temperature (°C)
F35P17 (Zirc-4)	1	Bottom of rod – 420 mm	10.3	3.9	414.8
	2	420 mm – 1,030 mm	10.1	3.8	405.6
	3	1,030 mm – 1,640 mm	9.9	3.7	396.0
	4	1,640 mm – 2,250 mm	10.2	3.8	406.2
	5	2,250 mm – 2,860 mm	10.1	3.8	405.1
	6	2,860 mm – 3,470 mm	10.0	3.8	403.7
	7	3,470 mm – Top of rod	10.0	3.8	402.7
3F9N05 (ZIRLO)	1	3,470 mm – Top of rod	10.2	3.8	408.2
	2	2,860 mm – 3,470 mm	10.1	3.8	404.8
	3	2,250 mm – 2,860 mm	9.9	3.7	396.2
	4	1,640 mm – 2,250 mm	10.1	3.8	406.0
	5	1,030 mm – 1,640 mm	10.0	3.8	404.0
	6	420 mm – 1,030 mm	10.0	3.8	402.5
	7	Bottom of rod – 420 mm	10.0	3.8	401.0
30AE14 (M5)	1	3,470 mm – Top of rod	11.2	3.6	451.6
	2	2,860 mm – 3,470 mm	10.1	3.6	409.4
	3	2,250 mm – 2,860 mm	9.8	3.6	397.8
	4	1,640 mm – 2,250 mm	10.1	3.6	407.4
	5	1,030 mm – 1,640 mm	10.0	3.6	405.5
	6	420 mm – 1,030 mm	9.9	3.6	402.6
	7	Bottom of rod – 420 mm	9.9	3.6	402.3
Average, all rods in all zones			10.1	3.7	406.4
Standard deviation, all rods in all zones			0.3	0.1	11.2

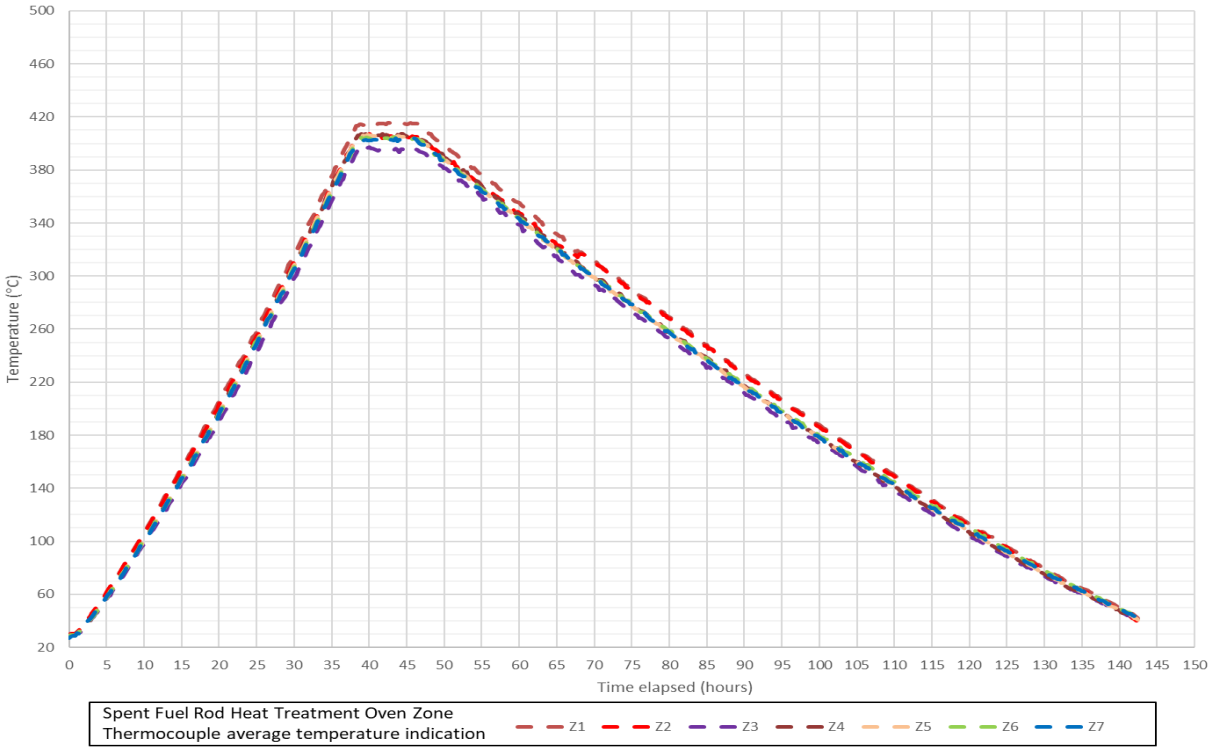

Figure 4. Heat Treatment Zone Average Rod Temperatures for F35P17.

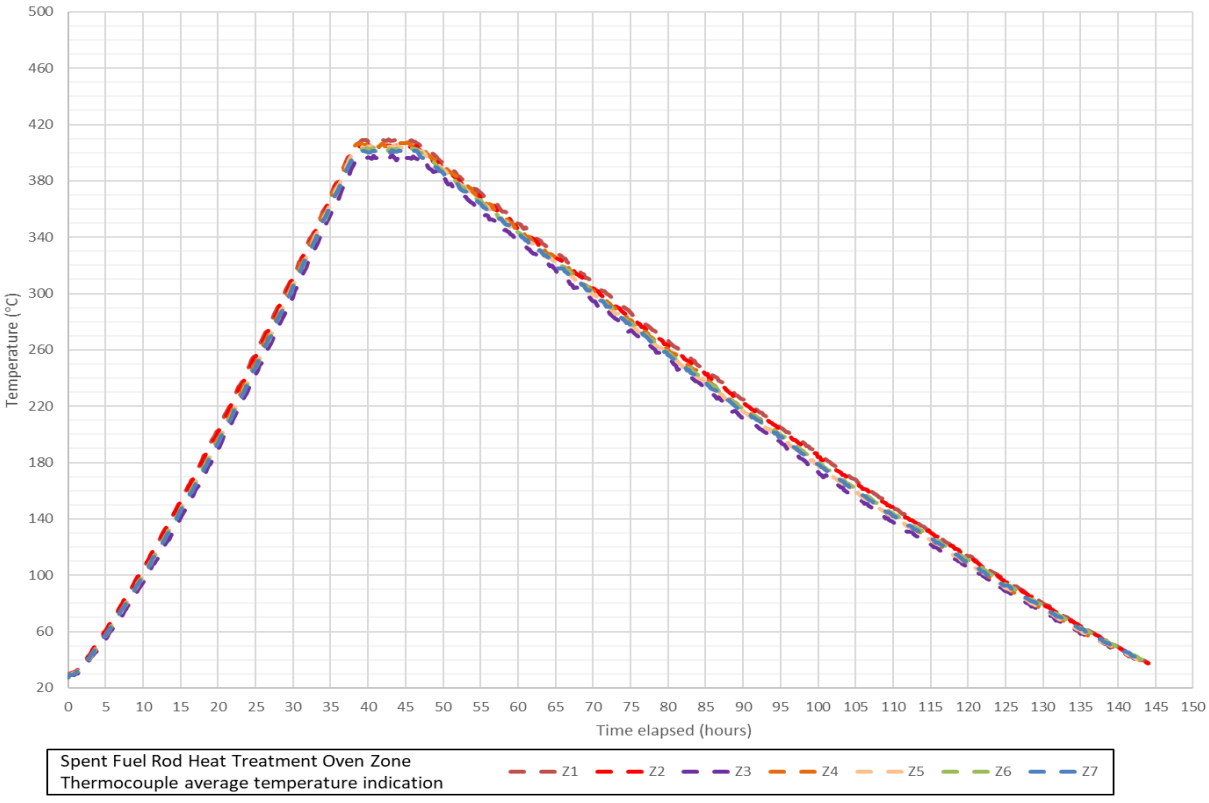

Figure 5. Heat Treatment Zone Average Rod Temperatures for 3F9N05.

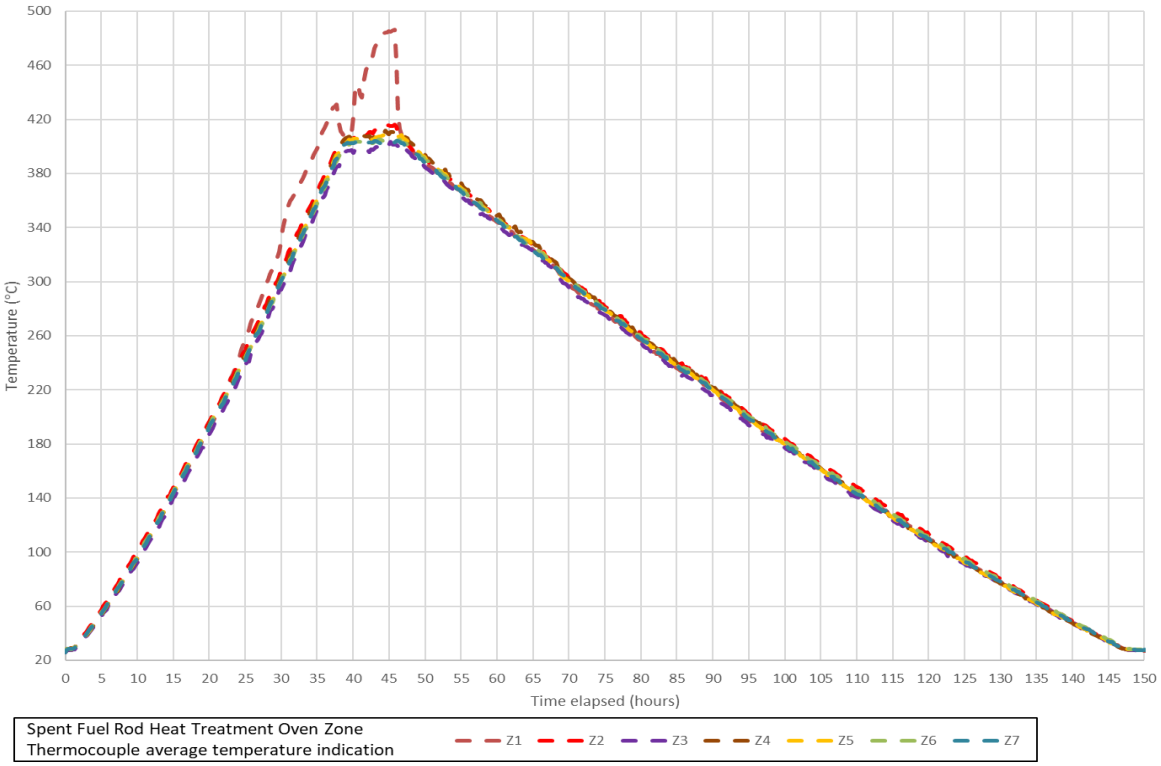

Figure 6. Heat Treatment Zone Average Rod Temperatures for 30AE14.

3.2 Evaluating the Higher Than Planned Soak Temperature of 30AE14

Although the soak temperature of Zone 1 on rod 30AE14 was corrected prior to initiating rod cooldown, it is important to assess the potential impacts on the follow-on experiments to be completed on that rod. In particular, the impacts on hydrogen and hydride reorientation, pellet-clad bonding, and annealing of irradiation defects can strongly influence the mechanical strength of the rod.

At room temperature, the measured pressure of 30AE14 was 3.2 MPa (see Section 3.2). At the targeted 400°C, the rod pressure would have been ~7.1 MPa. At the higher average temperature of 452°C that was imposed during the heat treatment, the pressure was ~7.6 MPa, about 8% higher than planned. The maximum pressure during the soak was estimated as 8.0 MPa at the 485°C peak temperature for ~1.75 h. The impacts of the higher temperature and pressure on pellet clad bonding will be investigated as more testing is completed.

It is unlikely that the higher temperature affected the behavior of the cladding hydrides for the following reasons:

- Based on the eddy current data [4], the M5-clad rod has a very thin oxide layer (31 μm peak measured lift-off) and is expected to have very low hydrogen content.
- At a low hydrogen concentration, all precipitated hydrides are expected to be dissolved in the cladding at 400°C, and no additional dissolution would have occurred as the result of the higher temperature.

- Given the low hydrogen content in the plenum region of the M5-clad rod, any migration of hydrogen from the hotter SFRHTO Zone 1 to the adjacent SFTHTO Zone 2 (<85°C cooler) is expected to be minimal.
- Because the controller was corrected and the temperature was restored to the target range (400°C) before the end of the soak, the cool-down phase proceeded as expected and precipitation of the hydrides should not have been affected.

To evaluate the potential effects on irradiation annealing, available data on irradiation defect annealing were collected. Bourdiliau [7] provides uniform elongation (UE) data on irradiation defect annealing in the 400–420°C range for Zr-1% Nb specimens (Figure 7). Cockeram [8] provides data on Zirc-2 and Zirc-4 materials annealed over much shorter time scales (1 to 500 h) and over a range of temperatures. Based on Bourdiliau's data, the increase in UE associated with 1,000 h at approximately 400°C is 4.5%. Given the 8 h soak time for the sister rods, the increase in ductility related to the heat treatment is expected to be <0.1%. Based on Cockeram's results, it appears that there is little change in the irradiation defect annealing rate as the temperature is increased from 400°C to ~500°C. Given these data, it is highly unlikely that there was additional annealing of irradiation defects as a result of the higher temperatures imposed on rod 30AE14.

Based on these discussions, it seems unlikely that the short increase in soak temperature will affect the results of the DE; however, the difference in the heat treatment conditions will be considered with the results of the DE when it becomes available.

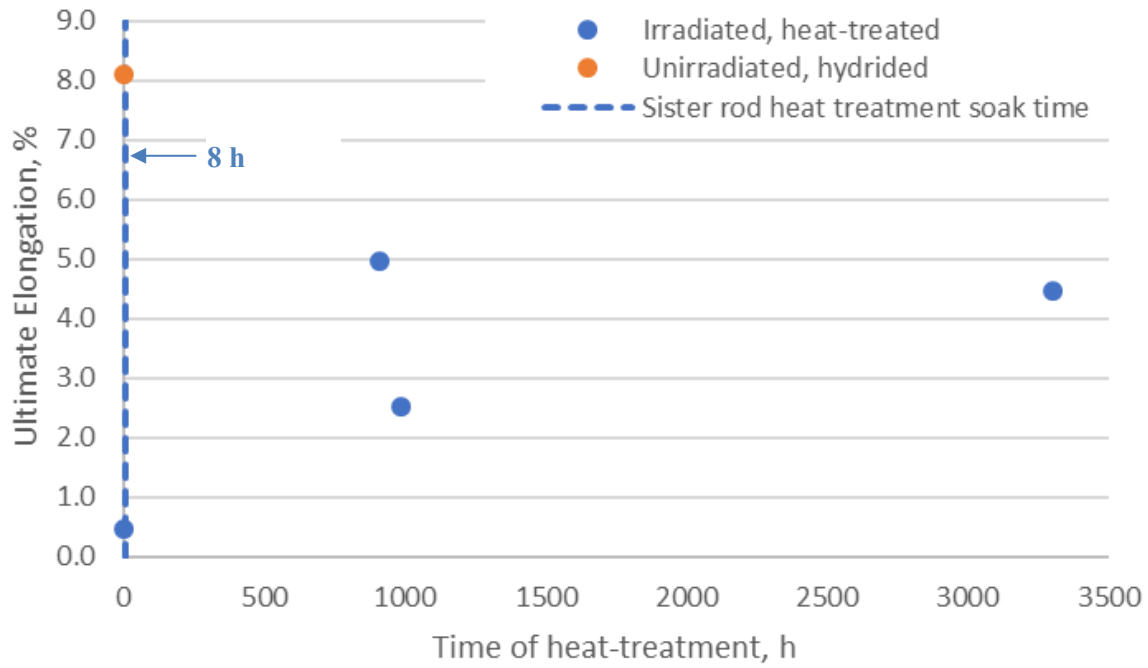

Figure 7. Data Available on Ductility for Irradiated Zr-1%Nb After Heat Treatments in the 400 to 420°C Range [7] as Compared with the 8 h Sister Rod Heat-Treatment Soak Time.

This page is intentionally left blank.

4. ROUGH SEGMENTATION (RS)

Seven Phase 1 rods have been segmented: 30AD05 (M5 clad), 30AE14 (M5 clad, heat-treated), 3D8E14 (ZIRLO clad), 3F9N05 (ZIRLO clad, heat-treated), F35P17 (Zirc-4 clad, heat-treated), 3A1F05 (LT Zirc-4 clad), and 6U3K09 (ZIRLO clad). A detailed cutting plan was developed [3], with test specimens allocated for the DE as guided by the test plans [2,3] and the results of the NDE [4]. Each segment was marked to indicate the upper elevation and placed into a labeled storage capsule as it was cut. The capsules are not backfilled with inert gas, as these Phase 1 rod segments are expected to be used in testing within a few years' time.

This page is intentionally left blank.

5. DEFUELING (DEF)

Many segments will be defueled in the process of specimen preparation for DE. For example, all DE.03 specimens must be defueled prior to testing. DE.10 includes both fueled and defueled specimens. In some cases, the removed fuel is the target of the test (e.g., DE.01 includes burnup measurements). The defueling processes vary depending upon the follow-on tests to be performed. This section provides a brief description of defueling activities.

5.1 Defueling Cladding Segments for Shipment

Twelve rod cladding segments were selected from the Phase 1 sister rods for ring compression testing as listed in in Table 3. The segments have been defueled by boiling them individually in an acid bath, and each piece of defueled cladding has been weighed, packaged individually in aluminum containers, and the dose rate was measured at contact and at one foot. The dose rates represent the hottest spots on the container. The exterior surfaces of the aluminum containers were decontaminated before they were loaded into the shipping container. The dose rate of a decontaminated empty aluminum container is expected to be <20mR/hr. Figure 8 shows the cladding segments in their aluminum containers awaiting shipment to ANL and a dose rate measurement being taken on one sample in its aluminum container using a Ludlum 9-4 ion chamber.

To determine the isotopic inventory of any pellet materials that may still be adhered to the interior wall of the cladding following this defueling process, one 18 mm rod segment was defueled using the same process, and then the resulting defueled cladding segment was dissolved and analyzed. The results of the analysis, tabulated in Table 4, were used to determine the residual pellet material isotopic content of each cladding segment based on the segment's weight.

Shipment of the segments was completed in April 2019.

Table 3. Defueled cladding specimens for shipment to ANL

Sister rod and elevation of segment	Al canister weight (g)	Canister + clad weight (g)	Clad weight (g)	Gamma dose on contact (mR/hr)	Gamma dose @ 30cm (mR/hr)
30AD05-2429-2519-DE.10	10.18	19.2	9.02	1,800	70
30AD05-3259-3349-DE.10	9.97	19.04	9.07	1,800	70
30AE14-2694-2784-DE.10	10.19	19.55	9.36	2,300	100
30AE14-3309-3399-DE.10	10.39	19.76	9.37	1,800	70
3A1F05-2555-2645-DE.10	10.22	19.74	9.52	1,200	50
3A1F05-3015-3105-DE.10	10.41	19.79	9.38	1,000	40
3D8E14-2213-2303-DE.10	10.17	19.68	9.51	1,400	60
3D8E14-2565-2655-DE.10	10.16	19.74	9.58	1,400	60
3F9N05-2572-2662-DE.10	10.22	19.78	9.56	1,400	70
3F9N05-3241-3331-DE.10	10.02	19.6	9.58	1,200	50
F35P17-2555-2645-DE.10	10.16	19.42	9.26	1,200	40
F35P17-3069-3159-DE.10	10.14	19.91	9.77	1,000	40

Table 4. Residual pellet materials after defueling on a per gram of cladding basis

Isotope	Ci/g	Isotope	Ci/g	Isotope	Ci/g
Co-60	7.20E-06	Np-237	2.14E-10	Pu-242	4.81E-09
Zr-95	4.15E-06	U-234	3.70E-10	Am-241	2.85E-06
Ru-106	2.08E-05	U-235	3.87E-12	Am-242m	2.44E-08
Sb-125	1.27E-05	U-236	1.07E-10	Am-243	6.47E-08
Cs-134	1.58E-04	U-238	7.19E-11	Cm-244	1.04E-05
Cs-137	1.27E-03	Pu-238	3.53E-06	Cm-245	2.41E-09
Ce-144	4.15E-06	Pu-239	3.75E-07	Cm-246	9.61E-10
Eu-154	5.53E-05	Pu-240	5.33E-07	Beta *	3.708E-03
Eu-155	1.94E-05	Pu-241	0.000147		

* "Beta" is remaining Beta activity after subtracting known beta emitters and G-Alpha result from liquid scintillation result. Assumption could be it represents Sr-90/Y-90.

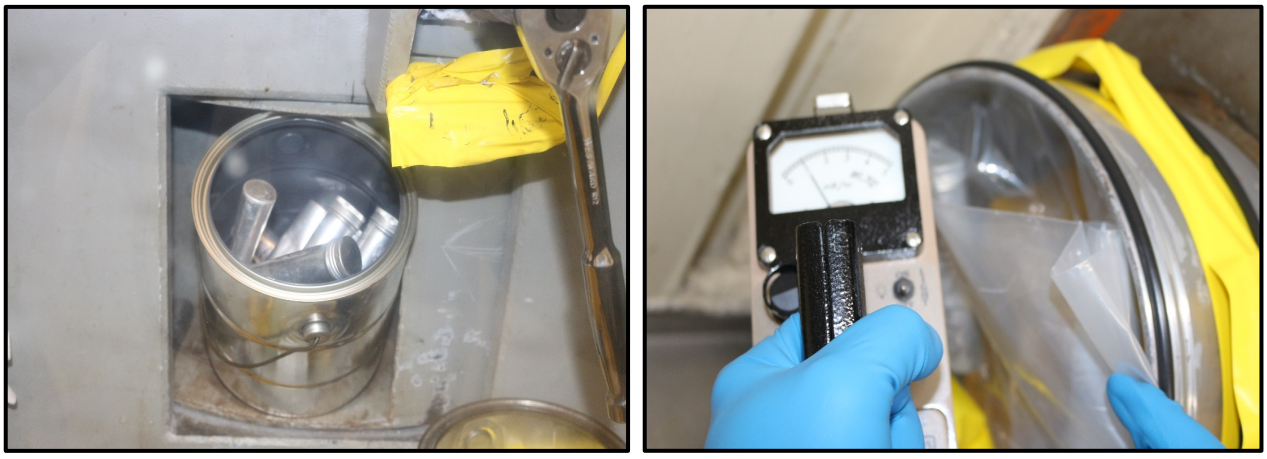

Figure 8. Defueled Cladding Segments in Aluminum Containers Awaiting Shipment to ANL (left) and Contact Dose Rate Measurement on a Single Container (right).

5.2 Defueling Cladding Segments to Prepare Total Cladding Hydrogen Specimens and Cladding Metallographic Specimens

To prepare specimens for total cladding hydrogen measurements (DE.03), the fuel is removed from the cladding. Also, it is desired to produce some cladding-only metallographic (DE.02) specimens. To remove the fuel from the cladding for these examinations, a dissolution column was constructed and installed in the IFEL hot cell in March of 2019. The column design incorporates a recirculating acid loop to reduce the volume of waste generated and to reduce acid vapor release to the hot cell atmosphere. The design also includes a Soxhlet extractor which periodically flushes the dissolution acid bath from the chamber where the cladding is held. This provides a supply of clean acid to remove as much fuel as possible. Figure 9a shows a defueled specimen planned for metallographic imaging, and Figure 9b shows the dissolution column in the ORNL hot cell. To date, 13 specimens have been defueled using the dissolution column.

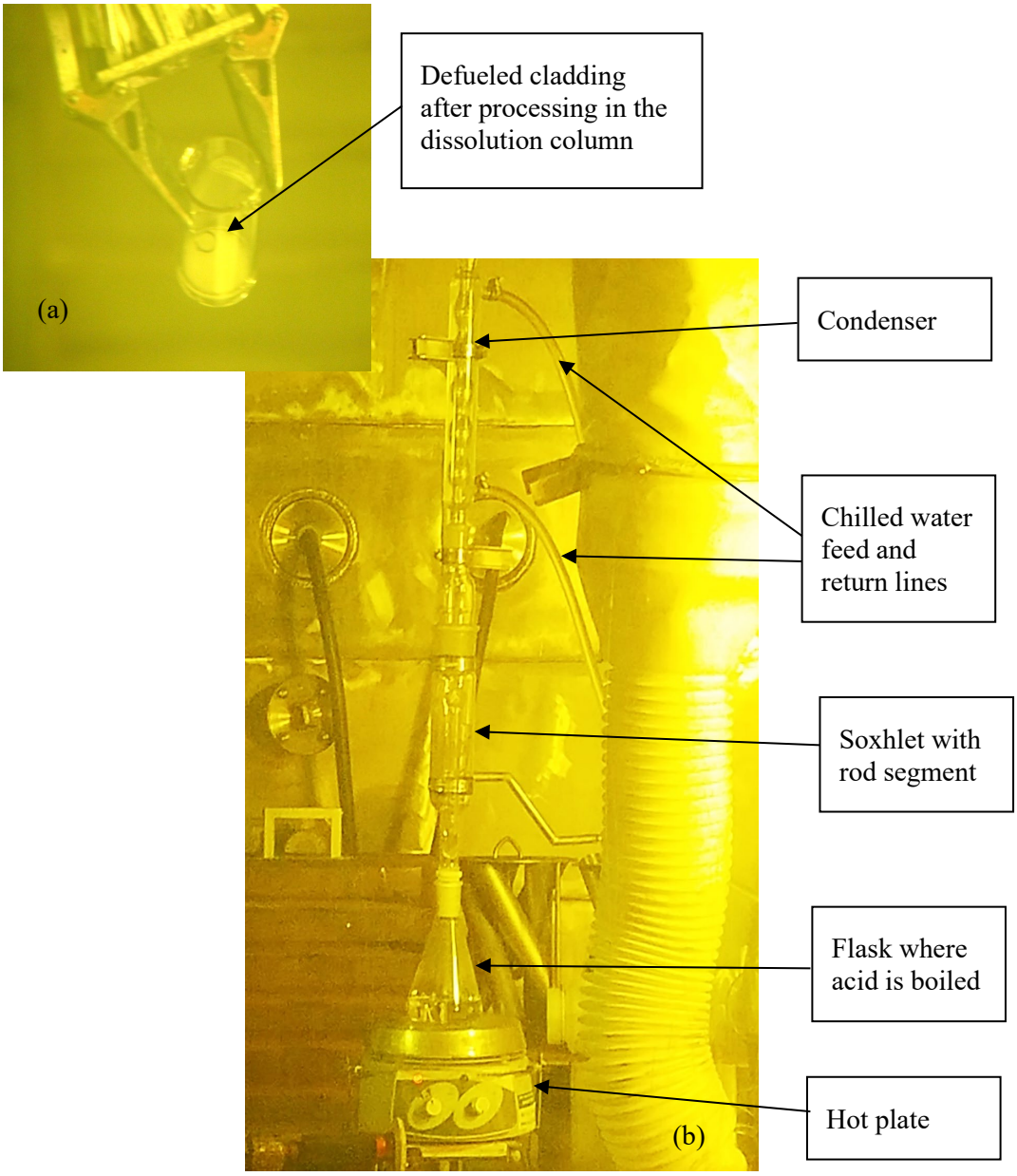

Figure 9. (a) A Defueled Specimen Ready for DE.02 or DE.03 after Several Passes in (b) the Dissolution Column Installed in the ORNL IFEL Hot Cell.

This page is intentionally left blank.

6. AEROSOL COLLECTION APPARATUS AND APPROACH (AERO)

To investigate the release of aerosolized radioactive material from a HBU fuel rod during fracture (10 microns or less is generally considered to be the upper limit of human respirability [9]), an aerosol collection capability is being developed for deployment on the CIRFT equipment (DE.05) and Instron load frame (used for DE.07, DE.08, and DE.10). Two different collection configurations (one for CIRFT and one for the load frame) will be developed, but the aerosol collection media and approach are expected to be the same.

The initial AERO design has been configured for the Instron load frame. An illustration of the collection enclosure is shown in Figure 10. The enclosure is an aluminum box with a replaceable plastic window in the front to allow viewing of the test in progress. The collection enclosure is expected to be used for multiple tests. The back half of the enclosure is fixed onto the load frame's lower load arm, and the front half is removable to allow access to insert load test specimens. The rear half of the enclosure includes buttons where as many as three aerosol collection cards can be hung; these cards are replaced for each test. Two versions of the aerosol collection cards will be used. The first includes a 4-filter cascade impactor with particle collection cut-points of 2.5 μm, 1.0 μm, 0.50 μm, and 0.25 μm. Silver filters are used in the cascade impactor. The second version of the collection card includes a single filter cassette with a cyclone having a 4 μm cut-point. Silver filters or polyvinyl chloride (PVC) filters are used in the single filter cassette. Each impactor/cyclone has its own dedicated vacuum pump to maintain the appropriate sampling flow rate. A wash system is provided to rinse the enclosure walls after each the test. The rinse fluid may also be collected and sampled for particulates.

Inertial impaction is the method used to collect particulates released from the sister rod specimen as it is fractured during testing. Impactors and cyclones are devices that separate the particulates based on size. In the 4-stage impactor, air containing the particulates to be sampled is accelerated through an orifice toward a collection filter placed at a fixed distance below an orifice. The collection filter forces the air stream to change direction abruptly, and particles that are large enough have enough inertia to escape the air stream and are collected on the filter. Particles that are smaller follow the air stream and remain suspended, moving on to the next stage of the impactor. In the single filter cassette, a cyclone is used at the bottom of the sampler, creating a flow vortex that allows only particles of a certain size to pass to the filter media. Larger particles that get into the sampler are collected in a grit pot at the base of the cyclone.

The *cut-point* is the size of particles collected by the sampler with 50% efficiency. Ideally, all particles greater than a certain size are collected on the filter and all particles that are smaller pass through. However, because impactors and cyclones are acting on aerodynamic variables and do not perform like a mechanical barrier such as a sieve, the collection efficiency is not 100%. Based on the orifice diameter and flow rate used, collection efficiency increases for particles larger than the cut-point, and it decreases for smaller particles. For a 4 μm cut point, 100% of 10 μm particles and 50% of 4 μm particles are removed from the air stream and deposited on the filter.

6.1 Collection System Prototyping

A prototype of the collection enclosure used with the Instron load frame was 3D printed and the fit up of the enclosure was evaluated. Specification of the equipment to be used for particle collection has been completed, and initial verification testing of the system's basic functionality was completed using the plastic prototype collection enclosure.

6.2 Collection System Validation Activities

After the system's basic functionality was confirmed using the 3D printed prototype, 2 aluminum enclosures for the load frame were fabricated. These were delivered in June 2019, and validation testing is in progress.

The goal of the validation testing is to ensure that the enclosure and collection card designs produce a representative sample of the aerosols in environment. This will be accomplished using ISO test dust with known particle size and material distributions. Surrogate rod cladding was 3D printed and filled with the ISO test mixtures, and the surrogate rods are fractured on the load frame using the same fixturing planned for the sister rod tests. The aerosols released from the surrogate rods during fracture are collected using the collection card systems. Filters from the surrogate tests will be analyzed and imaged to determine if the collection system is sufficiently capable of defining the characteristics of the ISO dust. The rinse liquid collected during the verification tests will be analyzed to determine if large amounts of dust were deposited on the enclosure walls. If that is the case, a rinse will be incorporated at the end of each sister rod test, and the rinse liquid (isopropyl alcohol proposed) will be analyzed with the filters for each test.

It is anticipated that the out-of-cell testing will be completed by the end of FY2019, and that the collection enclosure can be used with the four-point bend testing beginning in FY2020.

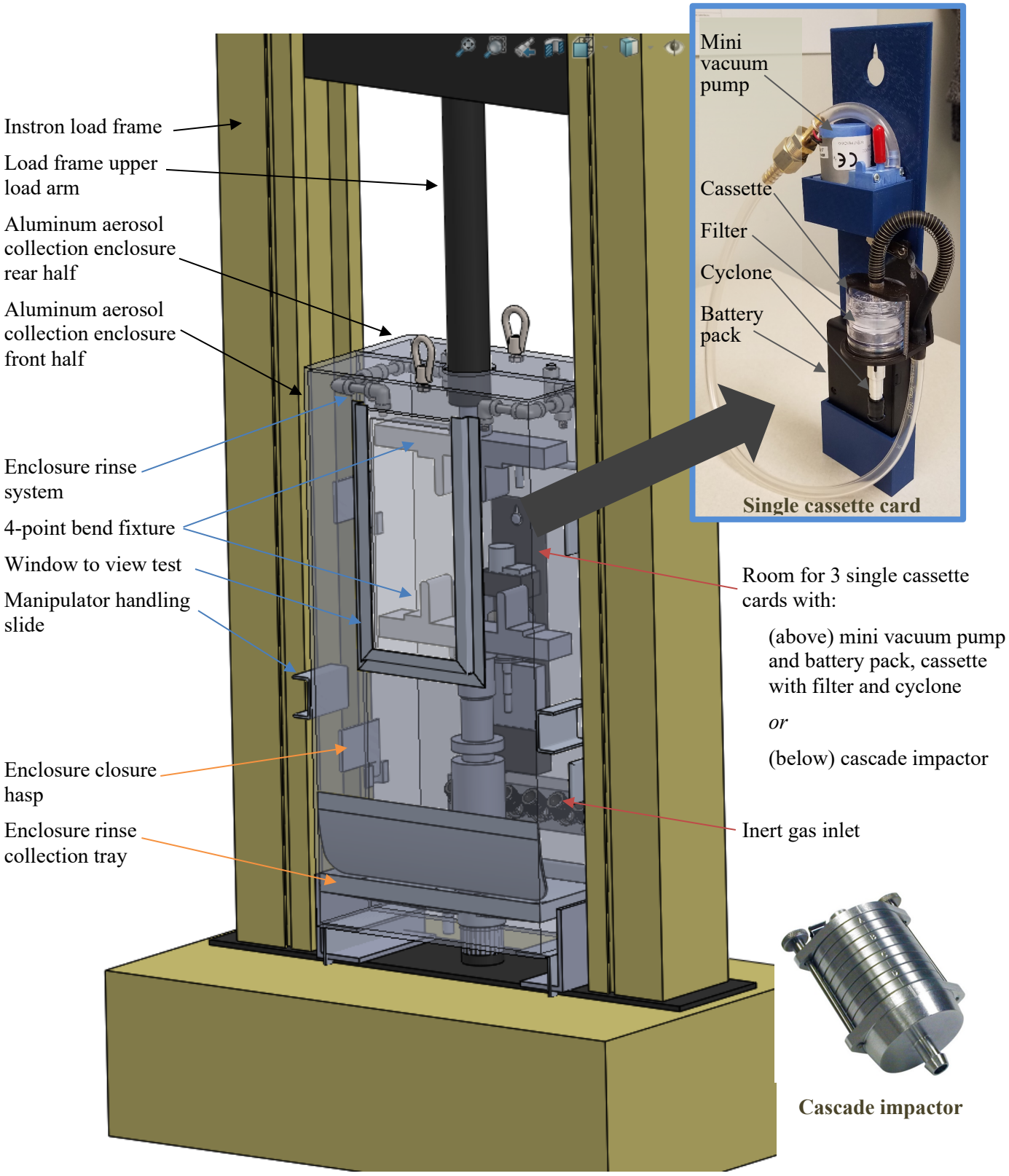

Figure 10. Illustration of the Load Frame Aerosol Collection Enclosure with One Cassette Sampling Card Shown.

This page is intentionally left blank.

7. ROD INTERNAL PRESSURE MEASUREMENT, ROD VOID VOLUME MEASUREMENT, AND COLLECTION OF FISSION GAS SPECIMENS, GAS TRANSMISSION TESTING (DE.01)

Commercial nuclear fuel rods are pre-pressurized with helium before irradiation. The magnitude of pre-pressurization varies with fuel design; at manufacture the sister rods were pre-pressurized between 1.7 and 2.5 MPa, depending upon their design. Each fuel rod includes a spring in a plenum at the top of the rod to provide a small compression load on the fuel pellet stack inside the rod, mainly to ensure that gaps between pellets do not occur. During irradiation and subsequent storage, the rod internal pressure increases due to production of fission gases (e.g., xenon, krypton) and volumetric changes due to swelling and irradiation growth. At manufacture, the rod includes spaces that are unoccupied by the fuel stack and spring termed the *void volume*. The void volume changes during operation as the cladding creeps and grows due to irradiation, and as cracks and porosity are formed within the pellets. For purposes of this discussion, the void volume is defined as including the volume in the plenum of the rod that is not occupied by the spring, the gap between the pellet outer diameter and the cladding inner diameter, the volume of any pellet chamfers and dishes, and the volume of pellet cracks and open porosity at the specified temperature. Because rod internal pressure and void volume are important parameters in determining rod performance throughout its lifetime, both were measured for each of the sister rods.

7.1 Rod Internal Pressure and Void Volume Measurements

The gas pressure and void volume of a fuel rod was measured by puncturing the plenum region of the rod and using the ideal gas law in conjunction with known pressures and volumes. The plenum end of the fuel rod is sealed into an evacuated housing of known volume (the “tare” volume). After puncture, the pressure in the housing was measured, and then the gas was expanded into another chamber of known volume, and the new pressure was measured. This double expansion method allowed the rod’s internal pressure and free internal volume to be determined. Once measurements were completed, the housing and the now-accessible free rod volume were evacuated and backfilled with a known volume and pressure of gas, and the final gas pressure was measured. This process allowed a second two-step measurement of the rod’s void volume and a second calculation for the rod’s internal pressure.

Section 7.1.1 discusses ORNL’s approach in designing the rod’s internal pressure and void volume measurement system and the general operation of the developed system. Section 7.1.2 summarizes the results for the sister rods tested in Phase 1. Appendix A provides a detailed description of the puncture system and its operation, as well as derivation of the 2σ measurement uncertainties, a description of the out-of-cell testing performed, discussions on the time required to pump down a fuel rod to vacuum, estimated retained fission gas volumes after rod pump down, and calculated impacts of retained fission gas and temperature differentials on the final pressure and volume measurements for the ORNL system.

7.1.1 Puncture system operation and design considerations

The measurement system’s design is extremely important in achieving accurate internal rod pressure and void volume measurements. The basic layout of the puncture apparatus is shown in Figure 11, and the puncture housing is shown in Figure 12. Only part of the apparatus is in the hot cell; the radiation-sensitive gauge, fission gas sample bottle, inert gas supply, and vacuum pump are all outside the hot cell. Like many of the components, the line connecting the pressure gauge to the puncture housing is of small diameter to minimize volume, as minimization of the tare volume is an important system consideration. Component sizes were optimized based on the uncertainties in the system reference volumes and pressure indicator. This was accomplished using the experimental uncertainty quantification expressions derived in Appendix

A.4. Furthermore, the pellet stack introduces a flow impedance into the system which must be considered to estimate the pressure stabilization time, which is a function of pressure, as discussed in Appendix A.

To operate the puncture system, the plenum end of the fuel rod is inserted into the puncture unit and is sealed within the puncture housing, as shown in Figure 11. The small clearance between the outer diameter (OD) of the rod and the inner diameter (ID) of the puncture housing becomes a part of the system's tare volume. Before measurements are made, system seals are checked by holding pressure and then by holding vacuum. Once a leak-free system has been demonstrated, the tare volume is measured. Because the accuracy of the rod internal pressure and void volume measurements are very sensitive to the total system volume, the tare volume must be measured individually and accurately for each fuel rod. This is done by evacuating the tare volume and then expanding a known pressure and volume of inert gas (argon) into the tare volume. The fission gas sample bottle is used as a reference standard, providing a known pressure and volume of inert gas for the measurement. The volume of each fission gas sample bottle is individually measured prior to use (nominally 26 cc) and is known within ±0.2 cc. After expanding the inert gas from the fission gas sample bottle to the evacuated system tare volume, the ideal gas law can be used to calculate the system's tare volume (nominally 25 cc). Temperature is monitored during the measurements, and the calculations include temperature adjustments, as required.

Once the system tare volume is known, the rod is punctured within the housing in the following sequence: (1) the tare volume and a second calibrated volume bottle, the *expansion volume* (29.3cc) are evacuated, (2) the expansion volume is valved off, and (3) the sharpened point of the puncture pin is advanced until a pressure increase is detected by the pressure gauge. After puncture, the rod's free fission gas expands from the rod's void volume to fill the system's tare volume, and the pressure is recorded. The valve to the expansion volume is then opened, and the fission gas sample is expanded a second time into the known expansion volume. The final pressure is then recorded, and the ideal gas law is used to calculate the rod's internal pressure and void volume using the two measured pressure values and the known expansion and tare volumes. This is known as the *double expansion method*. The double expansion method generally has a slightly higher measurement uncertainty than the *two-step method* (see the description below) that is related to the inclusion of one additional uncertainty associated with the second expansion operation (see Appendix A). In practice the double expansion and two-step methods are complimentary as they provide independent corroborating data as well as an independent check on the operation of the apparatus.

Next, to capture a fission gas sample, the system pressure is reduced to ensure that the fission gas sample dose is low enough for transfer outside of the hot cell. To achieve this, the puncture pin is backed out of the housing enough to vent some of the fission gas to the hot cell's atmosphere. At a pressure reading of ~16 psia (0.11 MPa) which is slightly above local atmospheric pressure, the pin is again advanced into the housing to seal it, and the valve to the fission gas sample volume is opened. This low-pressure fission gas sample is expected to have the same mole ratio of gases as the original mixture contained within the fuel rod plenum, and the total number of gas moles can be calculated based on the measured total system volume and pressure.

Finally, to keep the rod's void volume measurement uncertainty as low as possible (as it is further propagated into the rod internal pressure measurement), a two-step method leveraging the smaller fission gas sample bottle volume is used. After obtaining the fission gas sample, the rod and the puncture system are evacuated. A second (replacement) fission gas sample bottle is pressurized using an inert gas at a known pressure and a known volume. This gas is then expanded into the evacuated tare and fuel rod void volume. This provides a second method of determining the rod void volume and pressure which can be compared to the double expansion method. Temperature is monitored during the measurements, and the volume and pressure measurements are standardized to 25 °C.

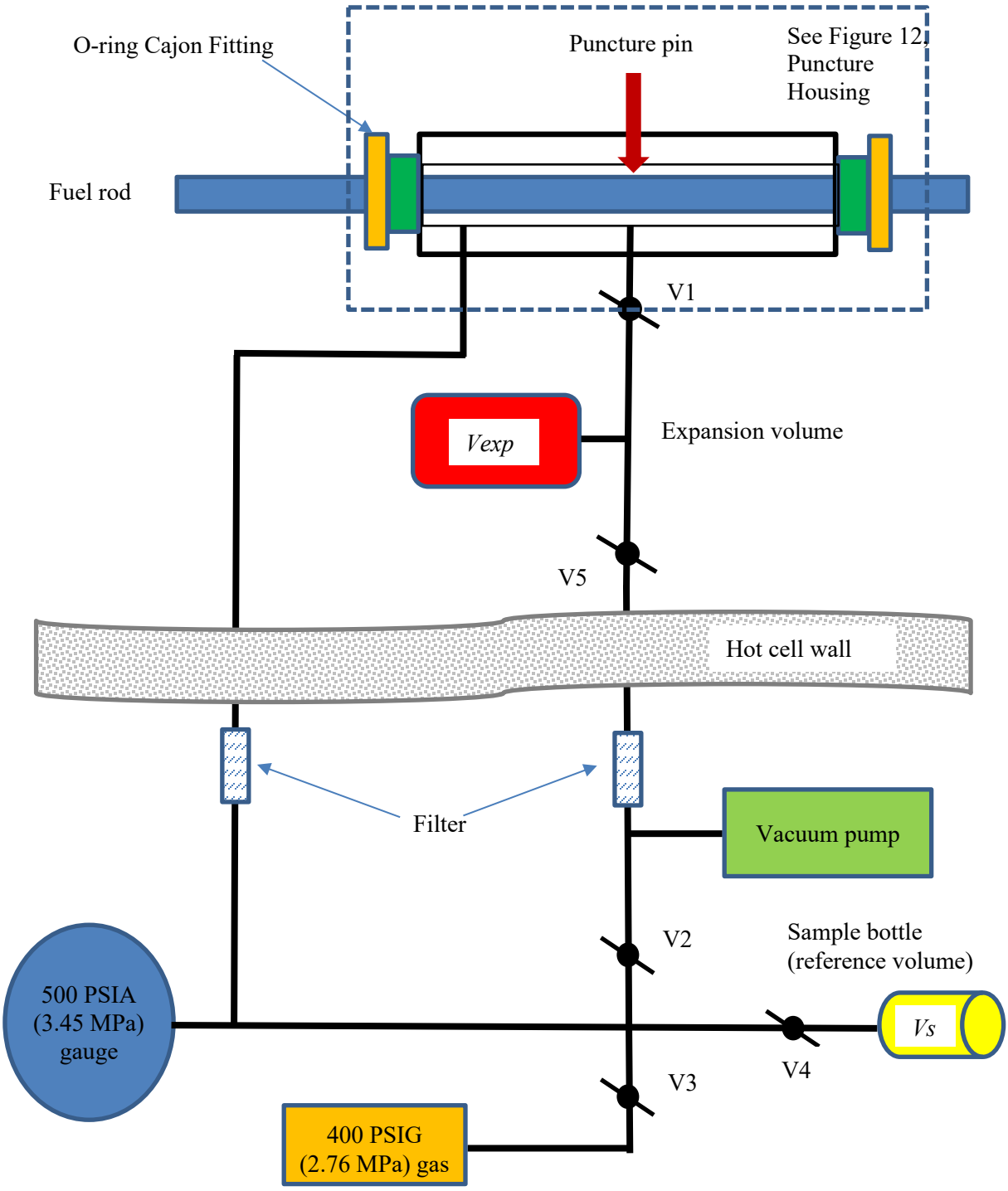

Note that only part of the apparatus is in the hot cell. The sample bottle provides a reference volume, and it also serves as a removable gas sample to be sent to the radiochemical laboratory.

Figure 11. Basic Layout of the Rod Puncture Apparatus Used to Measure Rod Internal Pressure and Void Volume, and to Collect a Sample of Fission Gas for Analysis.

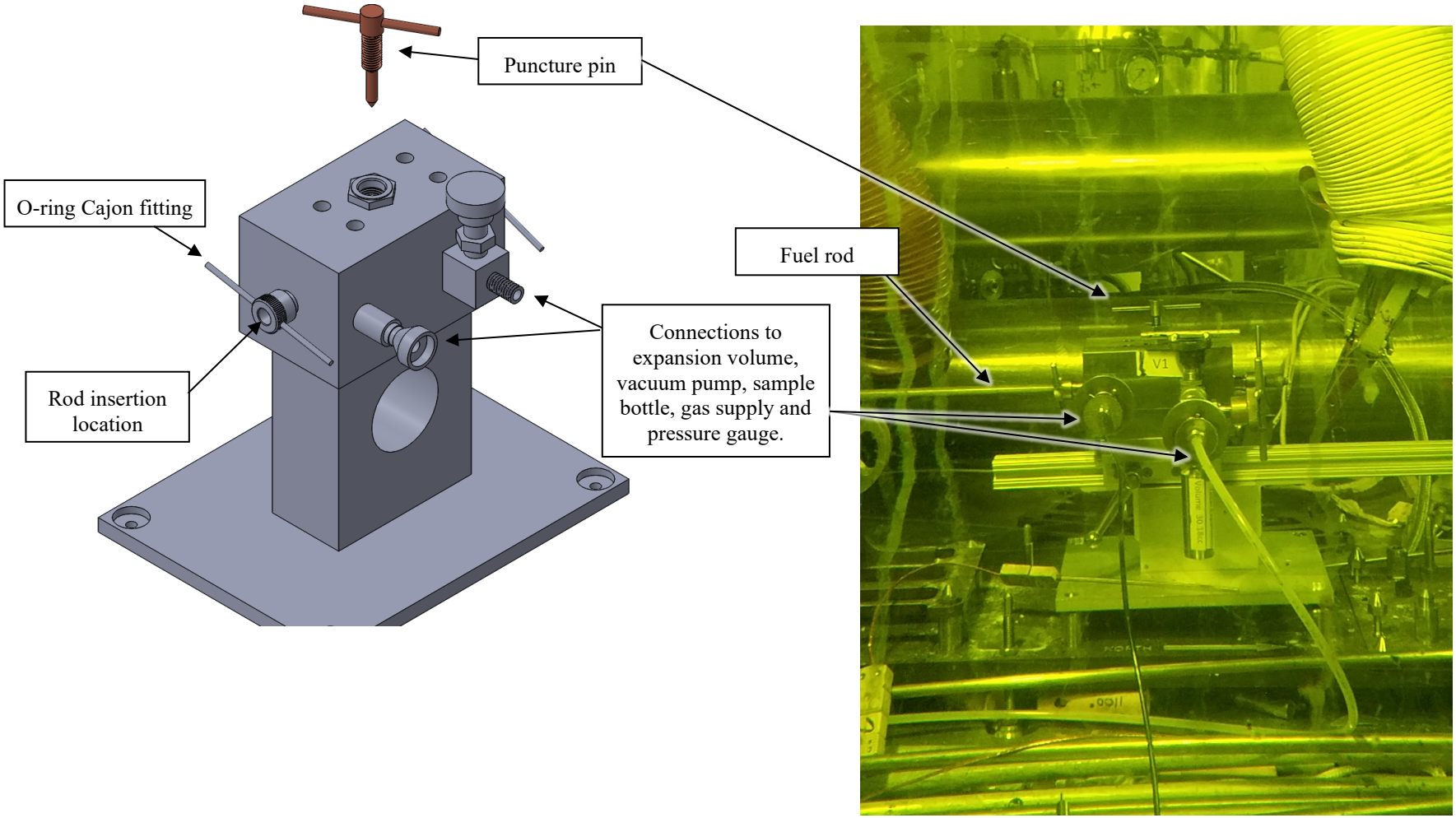

Figure 12. Illustration of the Puncture Housing (left) and a Photo of a Rod Inserted into the Housing for a Rod Internal Pressure Measurement (right).

7.1.2 Rod Internal Pressure and Void Volume Measurement Results

The results of the rod internal pressure and void volume measurements for the 8 sister rods punctured to date are shown in Table 5 along with the 2σ uncertainty. The double expansion method measured both volume and rod pressure in a single action and had a somewhat higher uncertainty than the two-step method, which measured the volume separately from the pressure measurement and thus offered a small improvement in uncertainty. Rod 30AK09 had a faulty measurement in the second expansion operation, so the double expansion results were invalid; however, the two-step method provided usable results. The rod puncture left a very small hole in the plenum region of the rod, estimated to be less than ½-mm in diameter.

7.1.2.1 Comparisons of the Sister Rod Measured Internal Pressure and Void Volume with Available Data from Other Fuel Rods

Figure 13 plots the sister rod measured internal pressures with other pressurized water reactor (PWR) fuel rod data from the Electric Power Research Institute (EPRI) [10] and the sister rod internal pressure is within the envelope of the available information. Likewise, Figure 14 plots the sister rod measured void volume with available EPRI data [10], demonstrating that the sister rod measured void volumes are within the extents of past measurements. However, while these general comparisons provide information about the sister rods relative to other commercial power PWR rods, direct comparisons cannot be made with the majority of the EPRI data because the mechanical design of the fuel rods are too diverse. Only four of the EPRI datapoints are from other 17×17 rods having a similar rod pre-pressurization of ~1.7–2.5 MPa and are more directly comparable, although they were not operated in domestic reactors under the same conditions as the sister rods. Other array types within the EPRI data cited are not directly comparable, as design parameters such as initial design void volume, pellet density and grain size, initial fill pressure, and cladding alloy (in addition to the fuel operating temperature in reactor) can strongly influence the end-of-life internal pressure and void volume. Figure 13 also includes four datapoints for Westinghouse 17×17 rods that were fabricated with an Integral Fuel Burnable Absorber (IFBA) coating on the fuel pellets [29]. The coating is typically a thin layer of zirconium diboride on the outer diameter of the pellets that is used for reactor reactivity control during reactor operation. None of the sister rods had IFBA coatings, but otherwise the rods are very similar to the sister rods. It should be mentioned that the heat-treated Zirc-4-clad sister rod, F35P17, is expected to be atypical because it was operated to HBU for four cycles as a lead test rod and is at a higher burnup than other sister rods and the four comparable EPRI rods that were measured.

Plotting the partial pressure of the fission gas (the measured rod internal pressure minus the rod design pre-pressurization [as adjusted for the change in void volume]) with rod average burnup yields similar information, as shown in Figure 15. Note that the initial void volume is not available for the EPRI data and the fission gas partial pressures for those reference datapoints were calculated assuming a volume adjustment of 1.2.

Table 5. Results of rod internal pressure and void volume measurements at 25 °C.

	cladding	Pre-pressurization (MPa)	Measured Pressure, Double expansion (MPa) [a]	2σ (95% confidence interval) Uncertainty [a]	Measured pressure, Two-Step (MPa)	2σ (95% confidence interval) Uncertainty	Volume (cc)	2σ (95% confidence interval) Uncertainty
30AK09	M5	1.7	N/A[b]	N/A[b]	3.46	2.5%	9.89	4.0%
30AD05	M5	1.7	3.50	4.1%	3.46	2.7%	10.63	3.7%
30AE14[c]	M5	1.7	3.25	4.0%	3.22	2.6%	10.99	3.6%
3D8E14	ZIRLO	2.0	4.14	3.0%	4.18	2.4%	11.73	3.4%
3F9N05[c]	ZIRLO	2.0	4.02	2.9%	3.98	2.2%	12.74	3.2%
6U3K09	ZIRLO	2.0	3.74	3.5%	3.64	2.5%	11.78	3.5%
3A1F05	LT Zirc-4	2.0	3.73	2.9%	3.73	2.2%	12.94	3.2%
F35P17[c]	Zirc-4	2.5	4.83	5.7%	4.68	3.8%	13.32	4.8%

[a] The double expansion method has a slightly higher uncertainty. The results are provided here as an independent measurement for information; however, the two-step method is the cited result for the rod internal pressure and void volume measurements.

[b] A problem with the second expansion operation introduced an irrecoverable error to the double expansion measurement for this rod.

[c] The rod was heat-treated as described in Section 3.1.1.

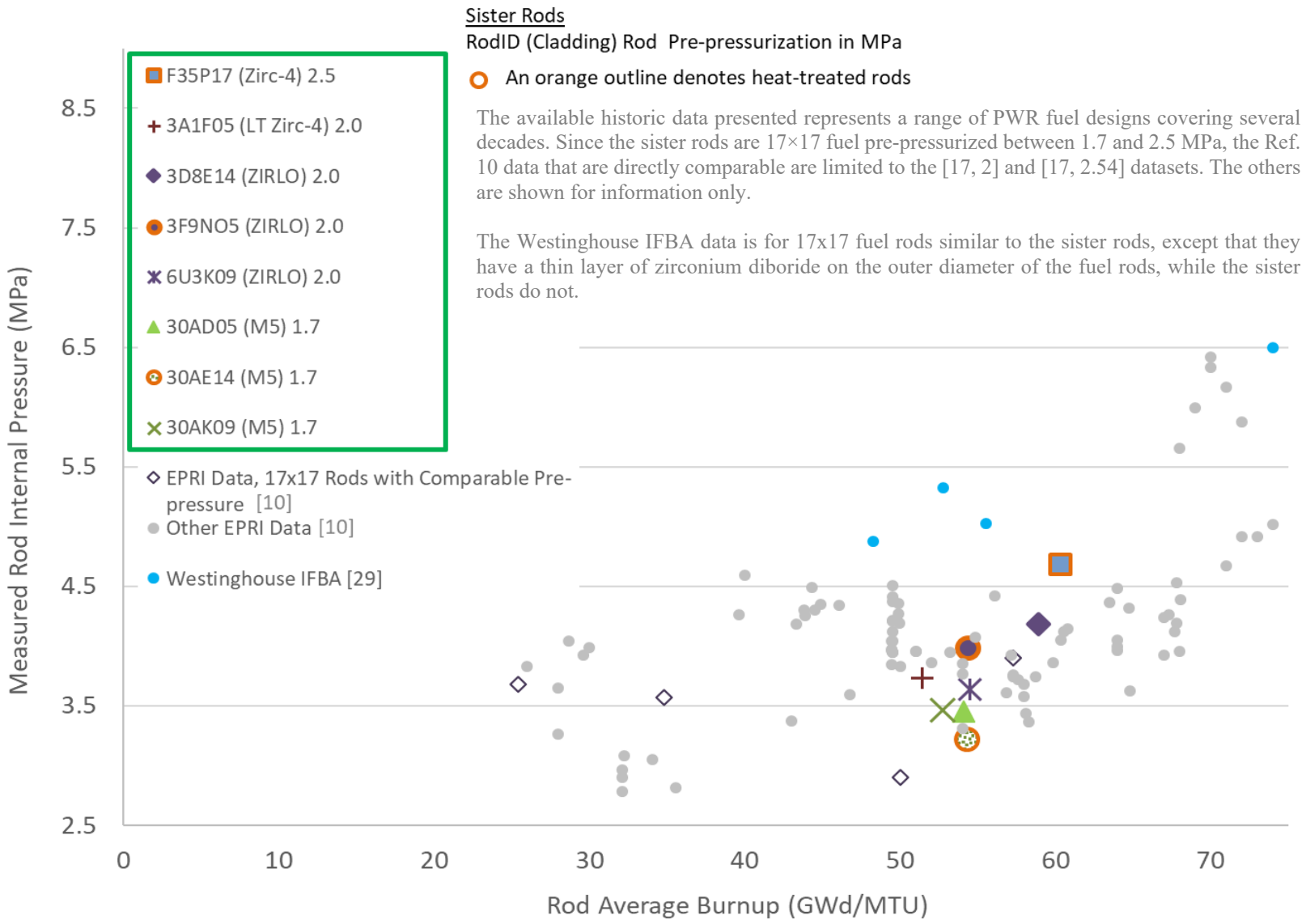

Figure 13. Sister Rod Measured Rod Internal Pressure at 25 °C.

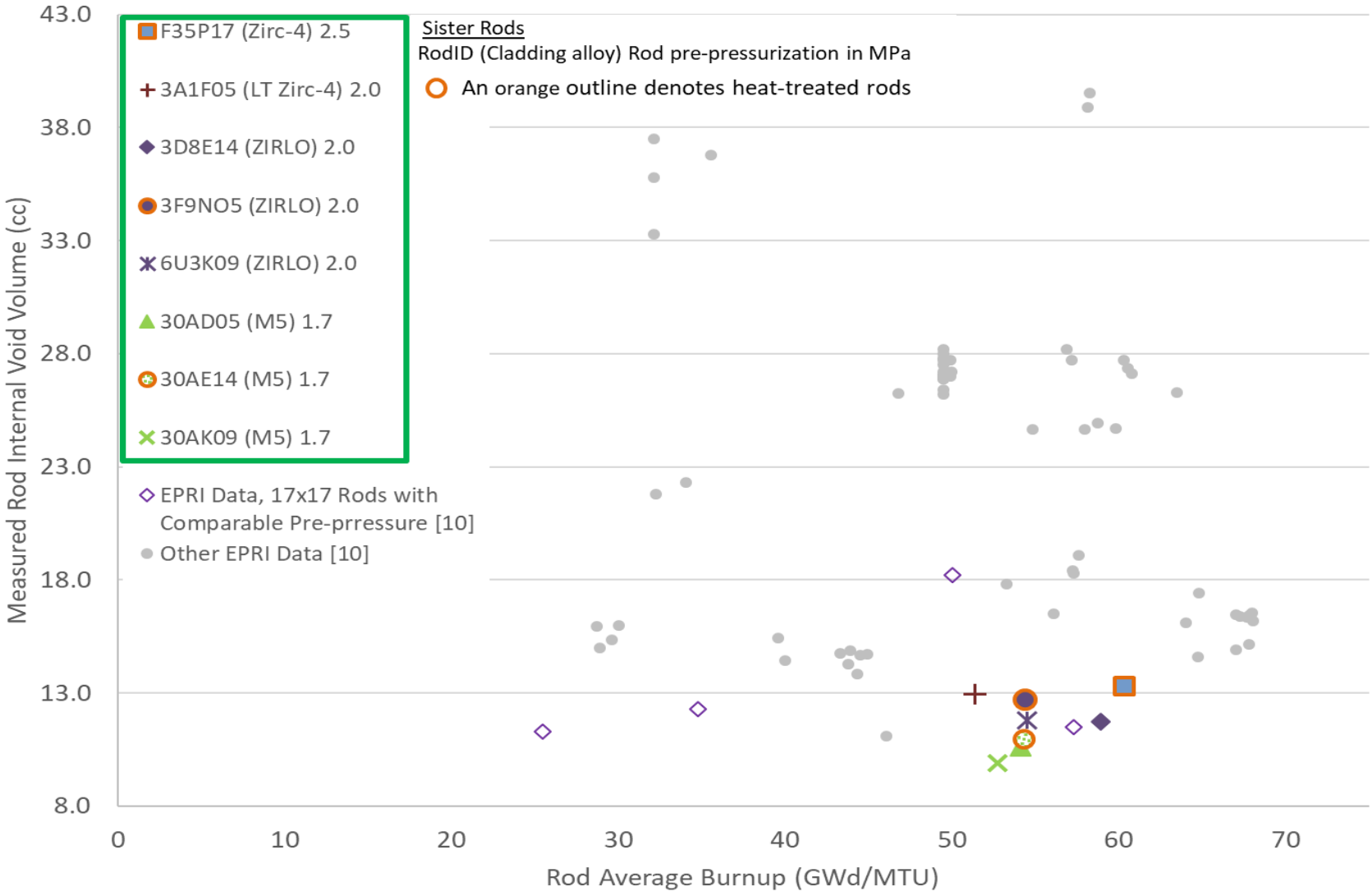

Figure 14. Sister Rod Measured Void Volume 25 °C with Comparable Historical Data.

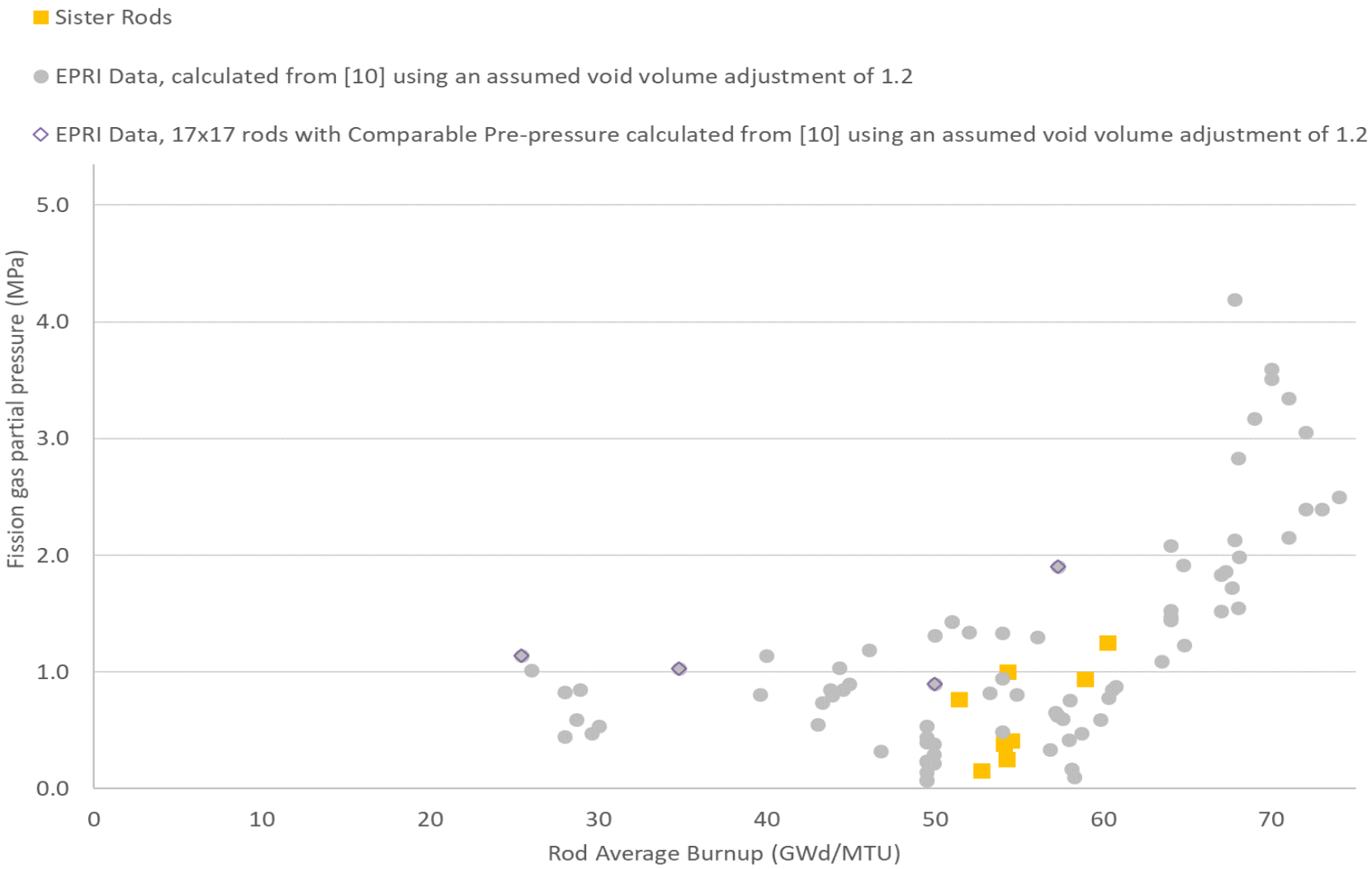

Figure 15. Sister Rod Measured Fission Gas Partial Pressure at 25 °C.

7.1.2.2 Comparisons of the Measured Internal Pressure and Void Volume with Available Data from Other Sister Rods

Figure 16a plots the measured rod internal pressure against the measured rod void volume and illustrates the expected grouping by vendor design/cladding type. For example, the Framatome designed rods are consistent with each other and the Westinghouse ZIRLO rods are consistent with each other. Figure 16b plots the measured rod internal pressure as a function of the rod nominal design pre-pressure. There appears to be a strong correlation between the end-of-life and beginning-of-life pressures ($R^2 > 0.6$).

Plots of the rod internal pressure with other parameters of interest such as the rod average burnup, assembly duty, average fuel temperature, and maximum fuel temperature (Figure 17) indicate that these parameters are not as strongly correlated ($0.4 < R^2 < 0.6$). This is likely due to the lack of a variety of data points within those parameters—as the range of burnup is small—combined with measurement uncertainties and inaccuracies in the rod's design and operational data (e.g., the maximum assembly middle-of-cycle temperature reported may not correspond to the sister rod's operating location). When considering only the fission gas partial pressure, the design and operational data are correlated at about the same quality ($R^2 \approx 0.4$), as shown in Figure 18. More operating data for rods at other are required to further evaluate the measured pressure and volume data within the context of power operation.

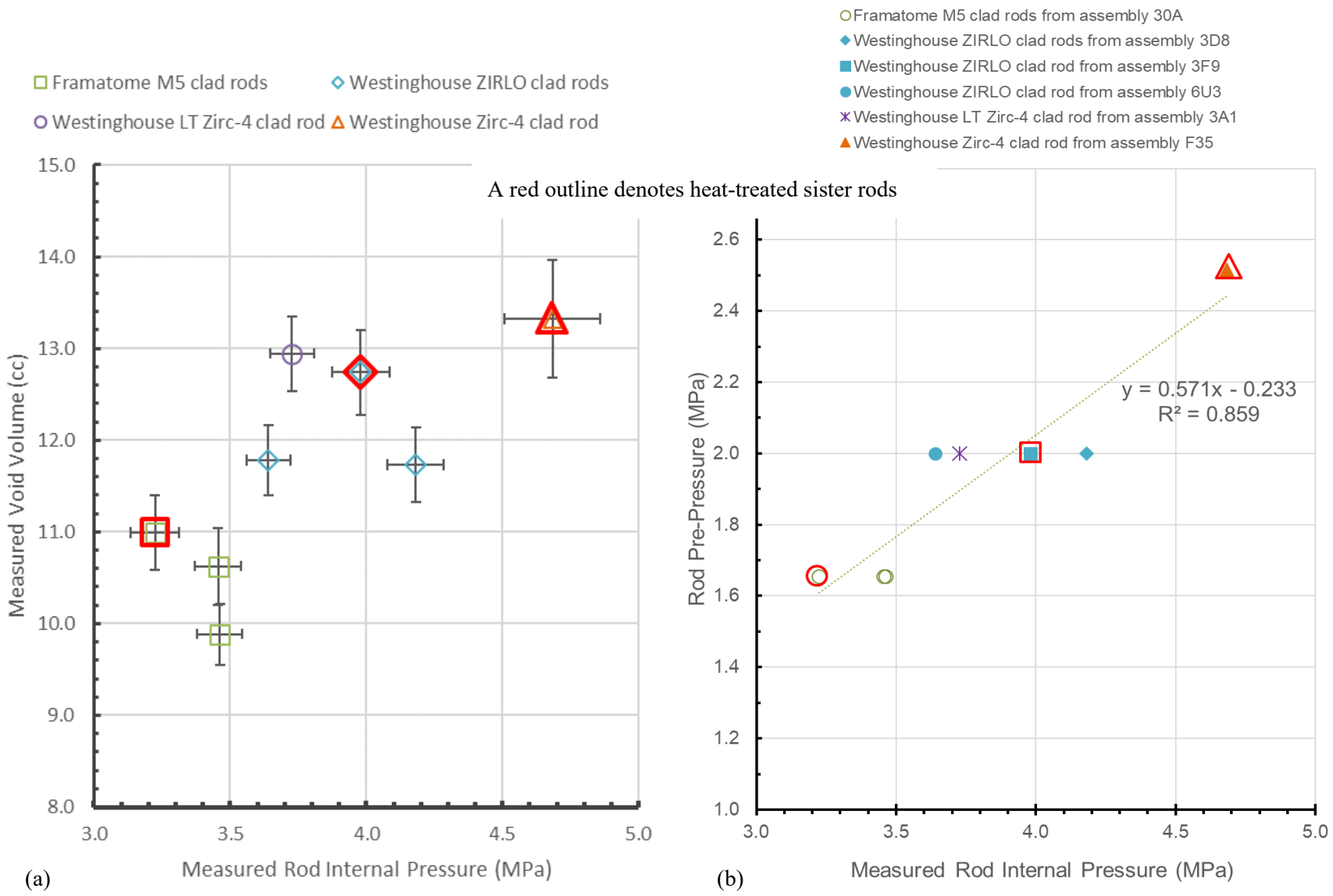

Figure 16. Sister Rod Measured Rod Internal Pressure vs. (a) Measured Rod Void Volume by Manufacturer/Cladding Alloy, and (b) Nominal Beginning-of-life Fill Pressure of the Rod by Manufacturer/Cladding Alloy/Parent Assembly.

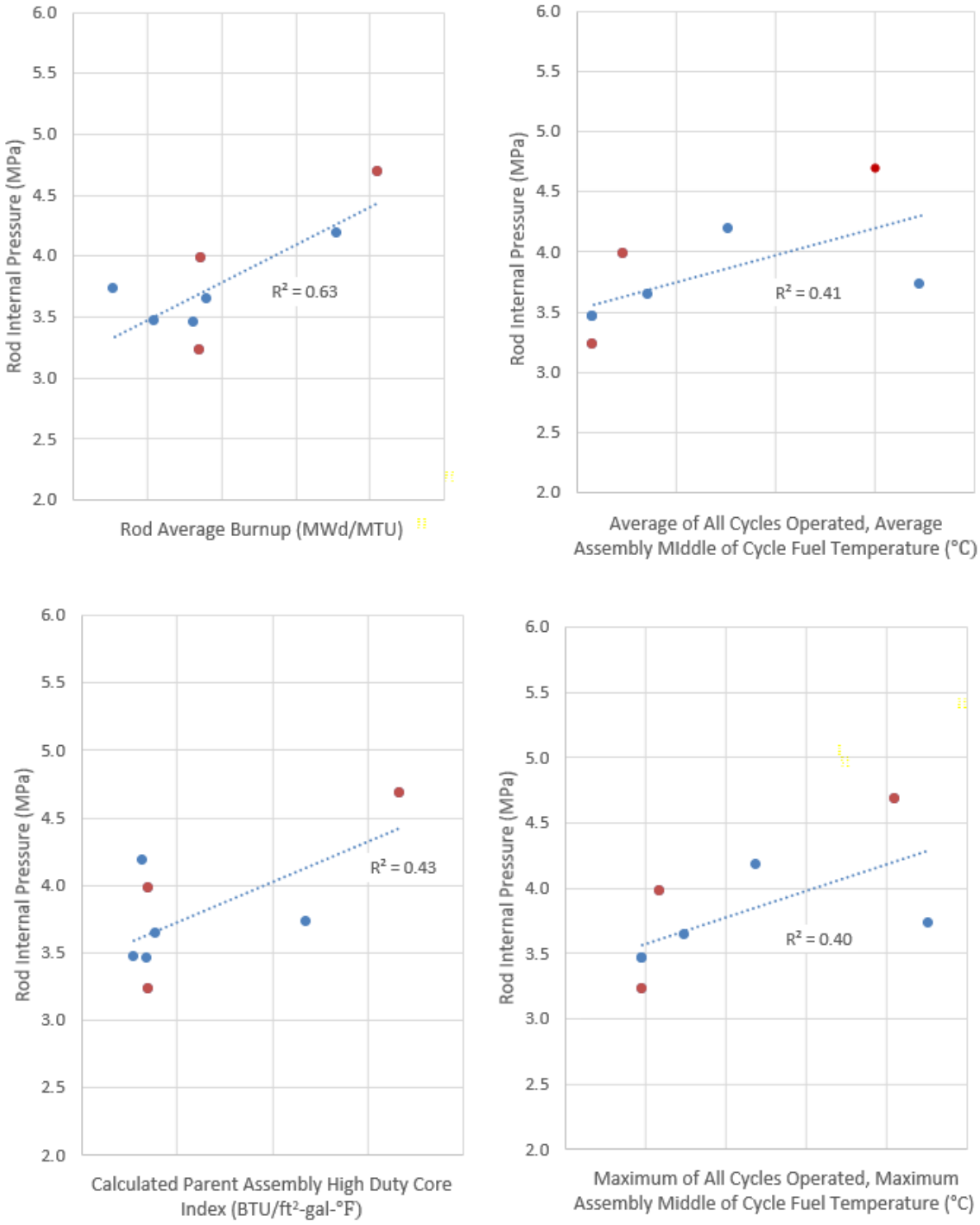

Note data for rod F35P17 are estimated.
The abscissas values are not provided.

Figure 17. Measured Rod Internal Pressure as a Function of Various Parameters of Interest (Red Symbols Denote Heat-Treated Sister Rods).

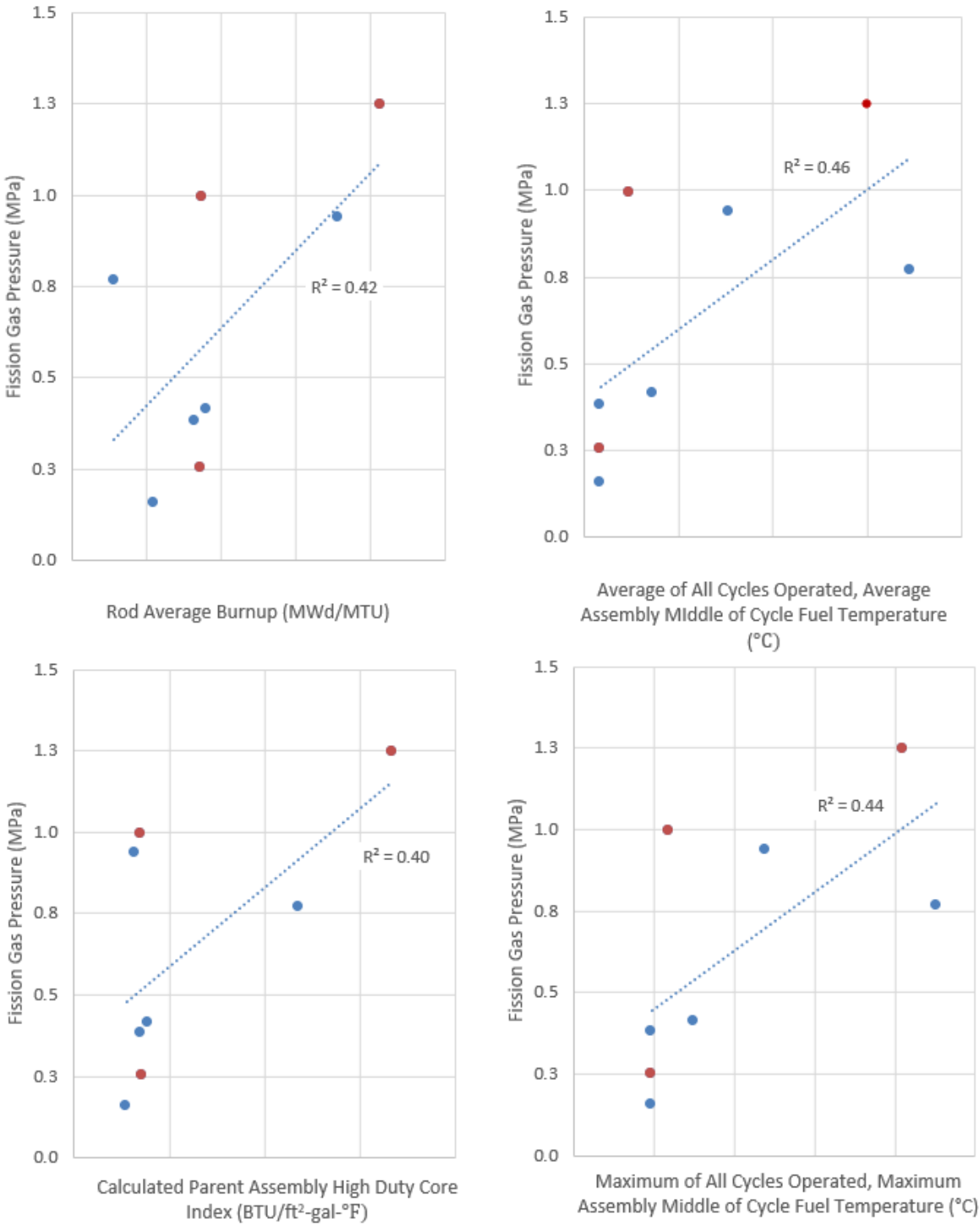

Note data for rod F35P17 are estimated.
The abscissas values are not provided.

Figure 18. Calculated Fission Gas Pressure as a Function of Various Parameters of Interest (Red Symbols Denote Heat-Treated Sister Rods).

7.1.2.3 Comparisons of the Heat-Treated Sister Rod Measured Internal Pressure and Void Volume with Baseline Sister Rods

Comparisons of the measured rod internal pressure and void volume can provide some information about the effects, if any, of the heat-treatments performed on three of the sister rods. For the ZIRLO-clad rods, the heat-treated rod has a higher void volume and a higher internal pressure than the corresponding baseline rods as shown in Figure 16(a). However, when evaluating the measured pressure and void volume data independently of other data reported herein (e.g., transmissibility reported in Section 7.2) and considering both the measurement uncertainty and the expected variation in rod internal pressure and void volume related to operational differences, it seems unlikely that the difference between the baseline and heat-treated rod measurement results are statistically different. The M5 heat-treated rod had a higher void volume and a lower pressure than the M5 baseline rods but are nearly within measurement uncertainty of each other. Thus, based only on the void volume and rod internal pressure measurements, there does not appear to be a difference between the ZIRLO- and M5-clad heat-treated and the baseline rods.

To determine if the heat treatment of the Zirc-4-clad rod made a difference in the rod internal pressure and void volume, it would be preferable to compare the results with the baseline Zirc-4 rod measured by PNNL. The void volume measured by PNNL on the baseline Zirc-4 rod is ~0.7 cc lower than that measured by ORNL on the heat-treated rod, which is almost within the ORNL 2σ volume measurement uncertainty of 0.5 cc. The rod internal pressure measured by PNNL for the baseline Zirc-4 rod is ~12% higher than that measured by ORNL for the heat-treated rod. PNNL's measurements of that rod were obtained from the bottom of the fuel rod in the pellet stack. Other than the PNNL Zirc-4-clad rod, the closest comparable baseline sister rod is a LT Zirc-4-clad rod. The void volumes of the heat-treated Zirc-4 rod and the baseline LT Zirc-4 rod are within measurement uncertainty of each other, as shown in Figure 16(a), but the heat-treated Zirc-4 rod pressure is significantly higher than the baseline LT Zirc-4 rod. The pre-pressure of the Zirc-4 rod was 0.5 MPa higher than the LT Zirc-4, but this does not account for the almost 1 MPa difference observed in the rods' end-of-life rod internal pressures. Although the Zirc-4 and LT Zirc-4 rods are very similar, differences in the rods' mechanical design could result in different end-of-life pressures and void volumes. Also, as mentioned previously, the Zirc-4 rod was a lead test rod that was operated to HBU over four cycles, while the LT Zirc-4 rod was a part of a typical batch fuel assembly operated over two cycles. Given these differences and based only on a comparison of the rod internal pressure and void volume data, it is not clear whether there was an effect related to the heat treatments on the Zirc-4-clad rod.

As a further comparison point, the product of the fission gas partial pressure and volume (P_fV) was examined, as it tends to neutralize any lab-specific biases in the available data. The P_fV was graphed with rod average burnups, including both ORNL and PNNL [11] data with available EPRI data [10] in Figure 19(a). It can be seen that the P_fV is relatively consistent for all of the sister rods, with the exception of a single datapoint, the Zirc-4-clad rod that was punctured in the pellet stack, F35K13 [11]. The sister rod data are consistent with the historical database, including a change in slope occurring at ~60 GWd/MTU. To determine if there is a difference related to the heat treatments applied, Figure 19(b) plots the available sister rod ZIRLO data, and Figure 19(c) plots the available sister rod M5 data. It can be seen that the data for ZIRLO rods from assembly 6U3 trend very well with burnup, even given the measurements from separate labs. Data from rods from assemblies 3F9 and 3D8 are also shown, with one of the 3F9 rods being the ORNL FHT rod, 3F9N05. The baseline ZIRLO rod from 3D8 appears to fit with the generally observed uptick in fission gas release shown in Figure 19(b). It is expected that the P_fV of rods from ZIRLO assembly 3F9 would follow a trend very similar to trends for ZIRLO rods from other fuel assemblies since they are of very similar manufacture and operation. The baseline 3F9 rod P_fV is not too far from that measured for a rod having a comparable burnup. However, the FHT rod does not appear to follow the trend established by the baseline ZIRLO rods from assembly 6U3, and based on Figure 19(b), it appears that there could have been an effect on either void volume or fission gas partial pressure related to the FHT. When the same

information is plotted for M5-clad rods, however, there does not appear to be an effect related to FHT, as shown in Figure 19(c).

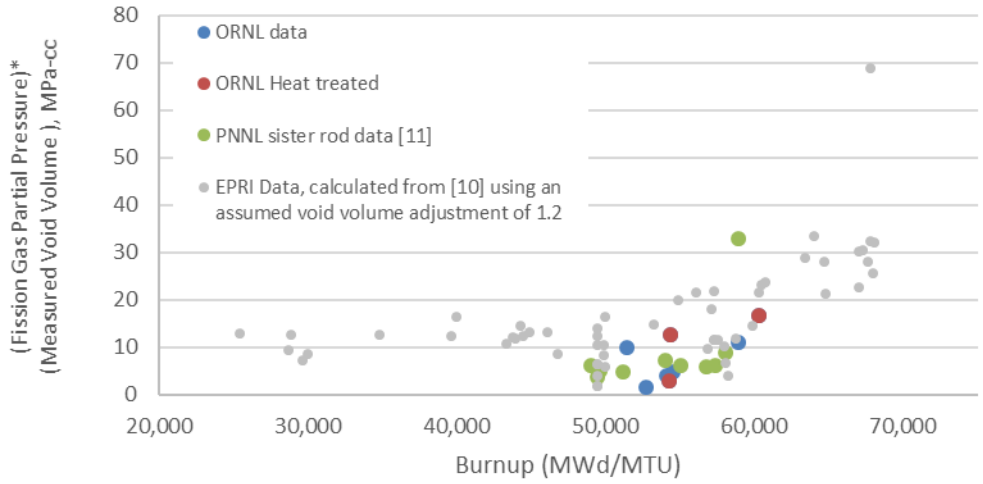

(a)

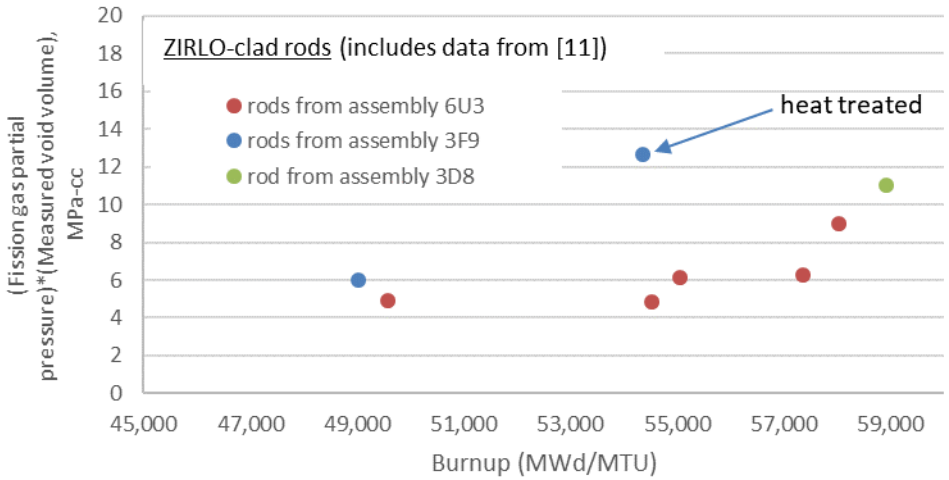

(b)

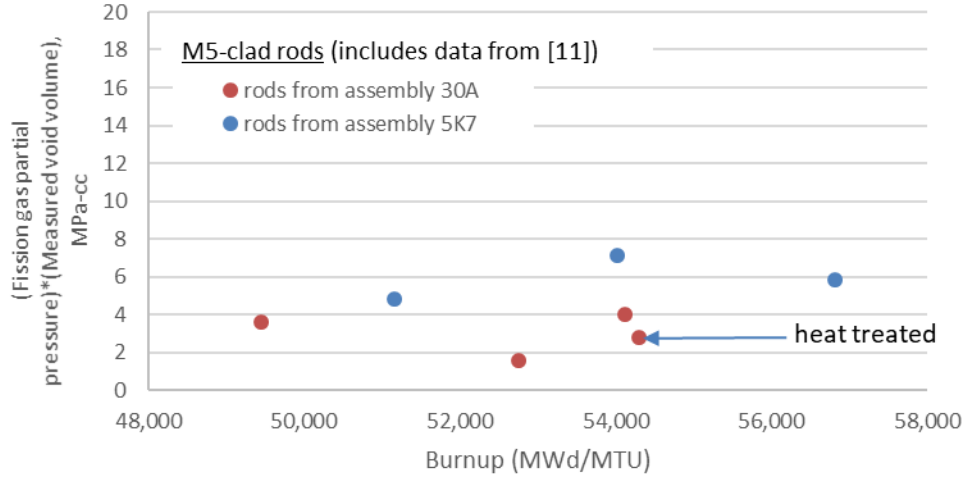

(c)

Figure 19. P_fV as a Function of Burnup for (a) All Data to Date, (b) ZIRLO-Clad Sister Rods, (c) M5-Clad Sister Rods.

7.1.2.4 Comparisons of the Measured Rod Internal Pressure and Void Volume with Code Predictions

As listed in Table 6, blind predictions of the sister rod internal pressure and void volume were made by Geelhood [12] using the FAST code and by Stimpson [13] using BISON. The two codes represent two different approaches in fuel rod modeling, with FAST providing models that are highly calibrated to a large body of empirical data and BISON operating through a more general first principles approach. This section provides a comparison of the two predictions with the measured data.

Figure 20(a) provides a comparison of the code-predicted rod internal pressure with the measured pressure. In general, BISON tended to over-predict pressure, while FAST underpredicted it. FAST pressure predictions for the ZIRLO-clad 6U3 rods were within ±5% of measured pressure, but other ZIRLO-clad rods from assembly 3F9 and 3D8 were within -25% of measured pressure. All of the M5-clad rods were underpredicted by FAST, with differences between -13 and -28%. The LT Zirc-4 rod pressure was also under-predicted (-18%) and the Zirc-4 rods were under-predicted (-15 and -25%) by FAST. It should be noted, however, that the Zirc-4-clad sister rod F35K13 was punctured from a location in the pellet stack. The average difference between the FAST pressure prediction and the measured value is -14%. While the FAST code appeared to produce more accurate pressure predictions for ZIRLO-clad sister rods, the BISON predictions didn't appear to have a trend related to the cladding alloy. The BISON pressure prediction difference from measured ranged from +10 to +81%, with an average difference of +40%. Five of the BISON rod simulations did not converge [13].

Figure 20(b) compares the measured void volume with the code-predicted void volume. BISON under-predicted void volume while FAST over-predicted it most of the time. As with pressure, the FAST void volume predictions for ZIRLO-clad rods from assembly 6U3 were more accurate than predictions for other sister rods, with the average difference ranging from 0 to +14%. Other than the trend noted for the 6U3 rods, there didn't appear to be a cladding alloy-related trend within the FAST void volume predictions. The average difference from measured void volume for the FAST predictions was +20%. The BISON void volume prediction average difference from measured was -37%. The BISON void volume trends appeared relatively insensitive, producing nearly the same void volume for all rods.

The product of the rod internal pressure and void volume (PV) provides an additional metric to compare the measured rod data with the code predictions. The predicted rod internal pressure and void volume (P_pV_p) are graphed with the product of the measured rod internal pressure and void volume (P_mV_m) in Figure 20(c). When considering PV, the FAST prediction difference from measured ranged from -14 to +18%, with an average difference of 2%. For the BISON predictions, the difference from P_mV_m ranged from +16% to -26%, with an average difference of -11%.

Figure 20(d) plots the differences of predicted from measured by rod average burnup, and this plot can be used to determine if there were any trends in the differences from measured values related to rod burnup. Because the 6U3 rods were more accurately predicted by FAST, those rods are indicated on Figure 20(d); they have a variety of rod burnups consistent with the range of burnups of the sister rods. Thus, the increased accuracy doesn't appear to be related to a particular range of burnup. No other obvious trends with rod burnup are visible and therefore it is concluded that the differences in the prediction accuracy are not related to rod burnup. When fission gas release is available for the sister rod measurements, it would be useful to make a comparison with the predicted fission gas release. Other operating data could be reviewed in a similar fashion to determine if improved modeling of a single parameter or a group of parameters can increase the accuracy of the internal pressure and void volume predictions.

Finally, in order to provide an additional viewpoint on whether the heat-treatments applied to three of the sister rods resulted in a change of the rod internal pressure or void volume, the predictions were compared graphically with ORNL's measurements (Figure 21). It can be seen in Figure 21 that the variations from rod to rod that were measured are consistent with variations predicted by FAST. An additional FAST

calculation was completed to simulate the applied sister rod heat treatments, and there was no change to the predicted fission gas release as a result of the short time at 400 °C. There does not appear to be a consistent pattern when comparing the BISON results with the measured results, and two of the BISON simulations for the rods graphed did not converge.

Table 6. Summary of Measured and Predicted Rod Internal Pressure and Void Volume

Rod ID	Cladding Type	Average Rod Burnup	Measured rod internal pressure (MPa)	Measured void volume (cc)	FAST predicted [12] rod internal pressure (MPa)	Fast predicted [12] void volume (cc)	BISON predicted [13] rod internal pressure (MPa)	BISON predicted [13] void volume (cc)
30AD05	M5	54	3.46	10.63	2.82	13.48	4.96	7.42
30AE14	M5	54	3.22	10.99	2.82	13.50	5.06	7.44
30AK09	M5	53	3.46	9.89	2.82	13.26	4.50	7.34
30AP02 [11]	M5	49	3.36	10.8	2.80	12.85	3.69	7.40
5K7C05 [11]	M5	57	3.97	9.7	3.11	14.61	No result reported	No result reported
5K7K09 [11]	M5	54	3.79	10.5	2.72	13.96	5.82	7.55
5K7P02 [11]	M5	51	3.35	11.2	2.73	13.43	4.53	7.39
3D8E14	ZIRLO	59	4.18	11.73	3.19	15.28	7.56	7.51
3F9N05	ZIRLO	54	3.98	12.74	3.46	14.76	No result reported	No result reported
3F9P02 [11]	ZIRLO	49	3.44	12.8	3.28	13.45	5.36	7.15
6U3K09	ZIRLO	55	3.64	11.78	3.47	13.41	4.56	7.10
6U3L08 [11]	ZIRLO	55	3.56	12.4	3.48	13.44	4.62	7.02
6U3M03 [11]	ZIRLO	57	3.72	11.9	3.53	13.57	4.95	6.97
6U3O05 [11]	ZIRLO	58	3.70	12.7	3.55	13.61	5.07	6.96
6U3P16 [11]	ZIRLO	50	3.28	13.1	3.37	13.16	4.29	7.40
3A1F05	LT Zirc-4	51	3.73	12.94	3.04	16.77	No result reported	No result reported
F35K13 [11]	Zirc-4	59	5.26	12.6	3.97	14.42	No result reported	No result reported
F35P17	Zirc-4	60	4.68	13.32	3.99	14.55	No result reported	No result reported

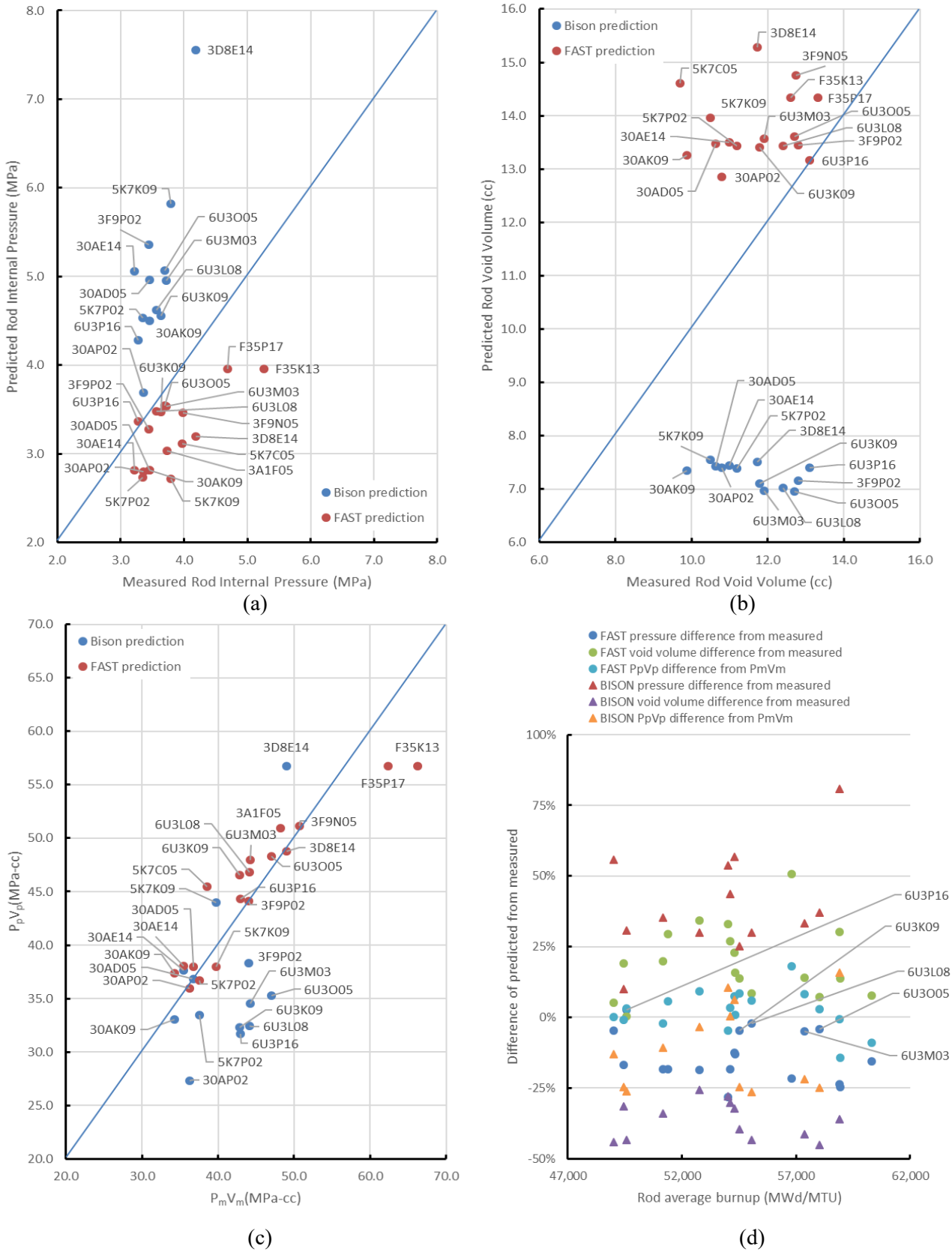

Figure 20. BISON- and FAST-Predictions versus Measured: (a) Rod Internal Pressure, (b) Void Volume, (c) Product of Rod Internal Pressure and Void Volume (d) difference of predicted from measured by rod average burnup

Figure 21. Predicted Rod Internal Pressure and Void Volume as Compared with ORNL Measurement Data.

7.2 Pellet Stack Gas Depressurization and Transmission Testing

The typical design of PWR fuel rods includes a small gap between the pellet OD and the cladding ID and a plenum volume at the top of the fuel rod that provides void volume for the helium gas used to pre-pressurize the rods. In addition to the gap and plenum void volumes, the sister rods' pellets include chamfers and dishes, and those void volumes provide a relatively large reservoir throughout the pellet stack for pre-pressurization gas. At beginning of life (BOL), these relatively large void volumes provide an open pathway for gas transmission up to the onset of pellet-cladding interaction (PCI). By the end of the first cycle, cladding creep down and pellet swelling tend to close the gap between the pellet OD and the cladding ID, and after PCI, gas transmission is restricted because the gap is no longer open. The amount of PCI varies axially. Local fission gas production and its release to the rod void volume are variable along the axial length of the rod because power, fluence, and fuel temperature vary radially and axially within the fuel rod [14].

However, as the rod is operated in the reactor, additional circulation paths through the pellet stack are developed, depending on local operating conditions. The process is somewhat stochastic and is related to thermal cycling of the fuel, crack development in the pellet due to thermal stresses, and crack self-healing. Once the fuel is discharged, the flow path becomes essentially fixed [15,16].

In order to characterize the ability for helium and fission gases to move through the pellet stack, gas transmission tests were performed. All punctured sister rods were subjected to a "depressurization" test, and three sister rods were also subjected to a "gas transmission" test. For the depressurization test, after the rod internal pressure and void volume measurements were complete, the rod's bottom end cap was cut off. Pressurized argon (~175 psia [1.21 Mpa] remained in the rod following the final two-step volume measurement) flowed from the plenum through the pellet stack and out of the bottom of the rod to atmospheric pressure and the pressure drop with time at the plenum was recorded. This depressurization measurement provided an initial indication of the resistance to fission gas transmissibility within the pellet stack and demonstrated gas communication from one side of the stack to the other at room temperature. For the gas transmission test, the free rod volume was evacuated, and a constant pressure source was connected at the open bottom of the rod. The gas flowed from the lower end of the rod upward along the pellet stack to the plenum and the pressure rise with time was recorded. Two or three different tests were completed for 3 rods at different pressures.

Section 7.2.1 discusses the general set-up of ORNL's gas transmission and depressurization tests. Section 7.2.2 summarizes the results for the sister rods tested in Phase 1. Appendix B provides a more detailed discussion of the measurement procedures and the methods used to correlate the data.

7.2.1 Depressurization and Gas Transmission Test Operation and Design Considerations

Schematics of the model control volumes, and depressurization and gas transmission configurations are shown in Figure 22(a), (b), and (c). Both the depressurization test and the gas transmission test are constructed with a constant pressure source connected to one end of the fuel rod and a pressure-monitored fixed volume reservoir connected at the other end and both ends are open to the pellet stack, as shown in Figure 22(b) or Figure 22(c), with the flow in opposite directions for the two configurations. The fuel rod system is divided into two control volumes connected by a flow path composed of the rod pellet stack with the control volumes and pressures as illustrated in Figure 22(a).

To describe the average gas transmissibility through the complete pellet stack and quantifying a permeability coefficient, the pellet stack is modeled as a single unit. The stack is considered a one-dimensional flow path having closely packed coarse irregular media (cracked UO_2 pellets) with a pressure differential across the media. The flow conditions are assumed to be isothermal.

To describe the movement of fission gas through the pellet stack, Muskat's porous media flow application [17] of Poiseuille's equation (compressible flow through a long cylindrical pipe) is used to approximate the flow to allow for comparison with previous work on this topic [18–21]. Appendix B.2 provides details of the application of the permeability correlations presented in this section and the following section.

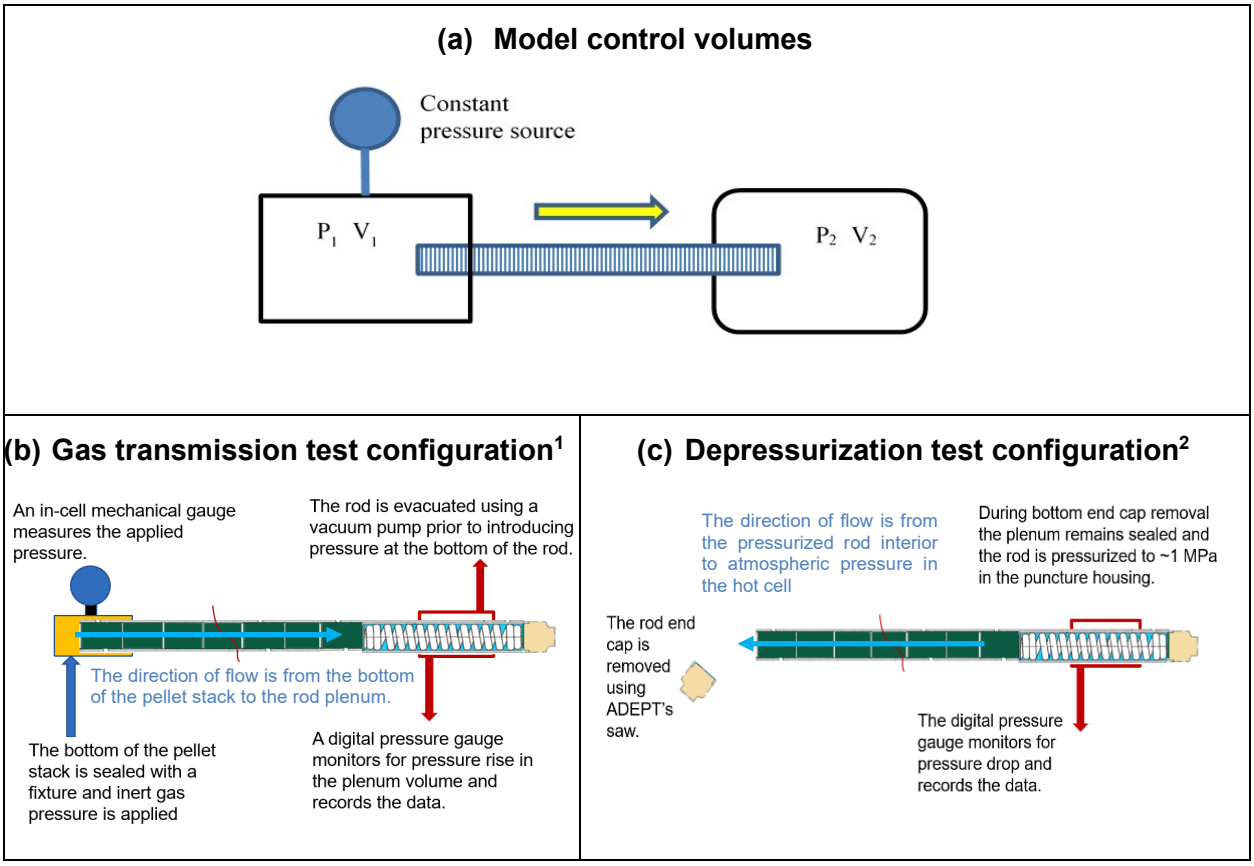

Figure 22. Schematics of the Depressurization and Gas Transmission Test Configurations.

[1] After the end of the rod is cut off and depressurization of the rod is complete, a compression fitting is sealed over the cut end, and pressurized gas is introduced.

[2] The plenum end of the fuel rod is pressurized with an inert gas. The end of the rod is removed, providing an outlet at atmospheric pressure.

As described previously, two versions of the gas transmission test are performed, a depressurization test and a gas transmission test. For the depressurization test, the plenum region pressure (P_2) starts at a high pressure and decays through the pellet stack, and the rod bottom end pressure (P_1) is held constant at atmospheric pressure. This is conducted by cutting off the bottom of the rod just after the rod plenum volume measurement, as illustrated in Figure 22(c). Note that prior to the depressurization test, the rod was evacuated and backfilled with the test gas. For the gas transmission test, a constant test gas pressure (P_1) is applied to the cut off rod end while the pressure (P_2) in the plenum volume (V_2) is measured, after first being evacuated, as shown in Figure 22(b).

The expected compressibility of the gases during flow through the pellet stack can be addressed by applying an adaptation for porous media flow to Poiseuilles' Law presented by Muskat [17]:

$$\frac{dm_2}{dt} = \left(\frac{KA}{2\mu L}\right)\left(\frac{M}{RT}\right)(P_1^2 - P_2^2) \quad (1)$$

where:

dm_2/dt is the mass flow rate into V_2
K is permeability (m^2) of a homogenous porous medium,
A is the cross-sectional flow area of the flow (m^2), in this application, the cross-sectional area of the space inside the fuel rod where the bulk flow is along the longitudinal axis of the rod,
L is the length over which the pressure drop occurs (m), in this application, the pellet stack length,
μ is dynamic viscosity (Pa·s),
M is the molecular mass of the gas,
R is the gas constant, and
T is temperature
P_1 is pressure (Pa) in volume V_1 (see Figure 22), and
P_2 is pressure (Pa) in volume V_2 (see Figure 22).

The volumetric flow rate is not constant along L, and the density of the flowing gas is allowed to change along the pellet stack. Through mathematical manipulations, a direct solution for the plenum pressure as a function of the permeability can be obtained for the Muskat-Poiseuille method (see Appendix B):

$$P_2 = \frac{P_1\left(1 - P_{op}\, e^{-K\eta t}\right)}{\left(1 + P_{op}\, e^{-K\eta t}\right)} \quad (2)$$

where P_0p is a constant of integration.

All tests were performed in the hot cell at room temperature, using argon as the test gas. Argon was used since it is closer in molecular weight to the fission gases. The heavier weight gases are more likely to be trapped or impeded by tortuosity within the pellet stack flow paths, unlike helium, which moves through most materials very quickly. Although xenon would have been the best gas to use, it is very expensive and difficult to obtain in large quantities. Table 7 specifies the material properties and the rods' physical dimensions used in the calculations.

Table 7. Argon material properties used in calculations

Parameter	Value
Dynamic gas viscosity of argon	2.42E-05 Pa-s
Stack length (typical)	3.65 m
Area cross section	5.15E-05 m^2
Measuring volume (rod plenum plus tare, typical)	3.77E-05 m^3

7.2.2 Depressurization and Transmission Test Results

The results of the testing are detailed in Table 8. The time versus pressure recorded for the depressurization tests is shown in Figure 23. Although some rods took longer than others to depressurize, none took longer than ~24 h to reach atmospheric pressure, demonstrating good communication along the pellet stack at room temperature. For the gas transmission tests, two sister rods were tested at three different pressures, and the time versus pressure recorded is shown in Figure 24. At the pressures used in the transmission tests, the time response of the system was ~30 min for one rod and ~3 h for the other. Both rods demonstrated a clear correlation of gas transmission time with the applied pressure. All tests verified the ability of the argon gas to move through the pellet stack at room temperature.

Table 8. Results of Depressurization and Transmission Tests

Rod	Applied Pressure differential (MPa)	Muskat-Poiseuille Permeability and regression model coefficient of determination	
		K (m^2)	R^2
3A1F05	0.10	8.40E-14	0.999
	1.41	8.32E-14	0.999
	2.17	8.32E-14	1.000
	2.89	8.23E-14	1.000
	Average	*8.32E-14*	
F35P17	0.10	9.96E-14	0.999
3F9N05	0.10	7.30E-14	0.999
3D8E14	0.10	4.08E-14	0.998
6U3K09	0.10	1.99E-14	1.000
	1.55	1.62E-14	0.994
	2.82	2.05E-14	1.000
	Average	*1.89E-14*	
30AK09	0.10	1.04E-14	0.999
	1.41	1.02E-14	0.999
	2.17	1.05E-14	1.000
	2.89	1.11E-14	1.000
	Average	*1.06E-14*	
30AD05	0.10	1.15E-14	1.000
30AE14	0.10	2.40E-14	1.000
	Average of all	***4.25E-14***	

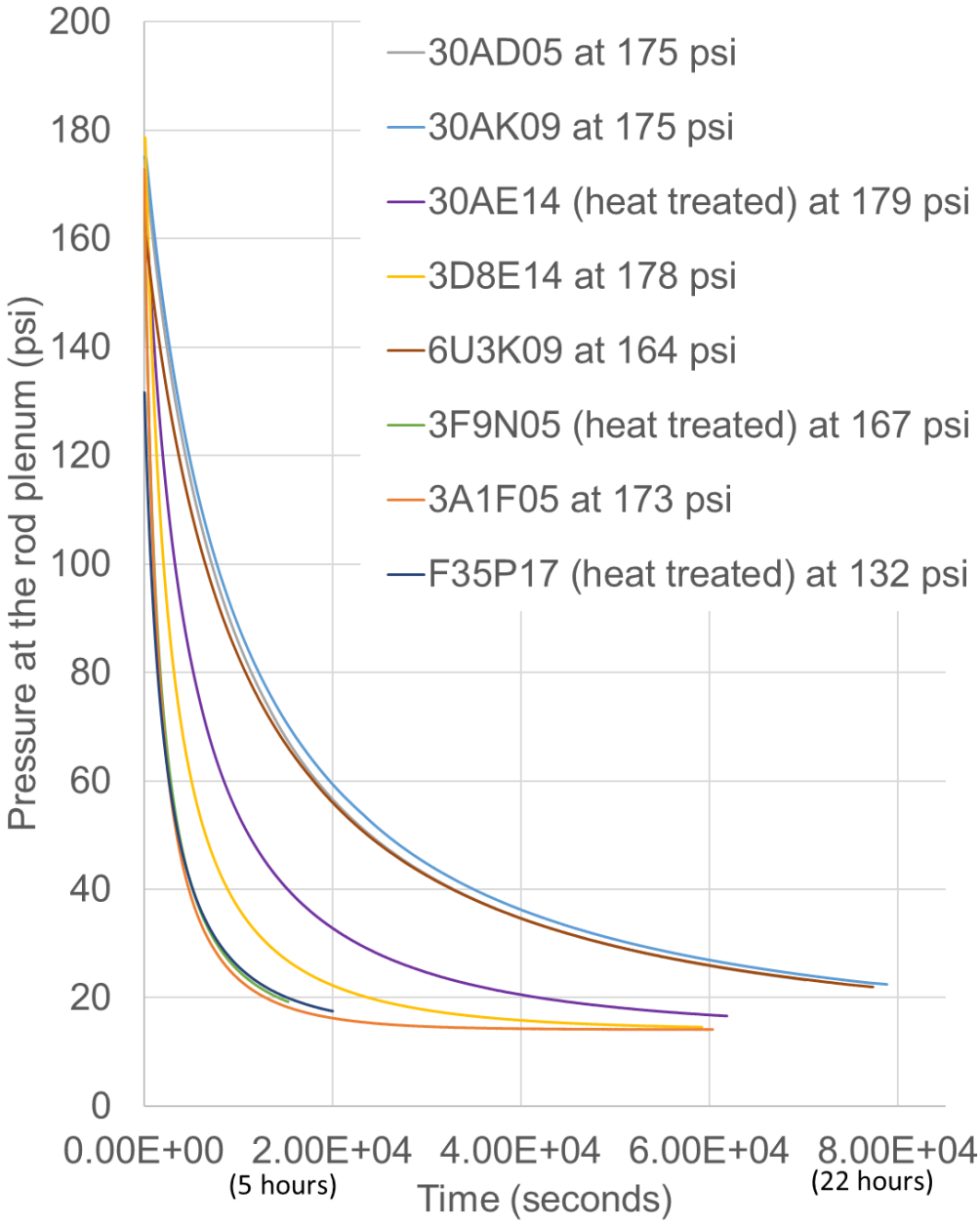

Figure 23. Results of the Depressurization Tests on 8 Sister Rods (3 rods were heat-treated).

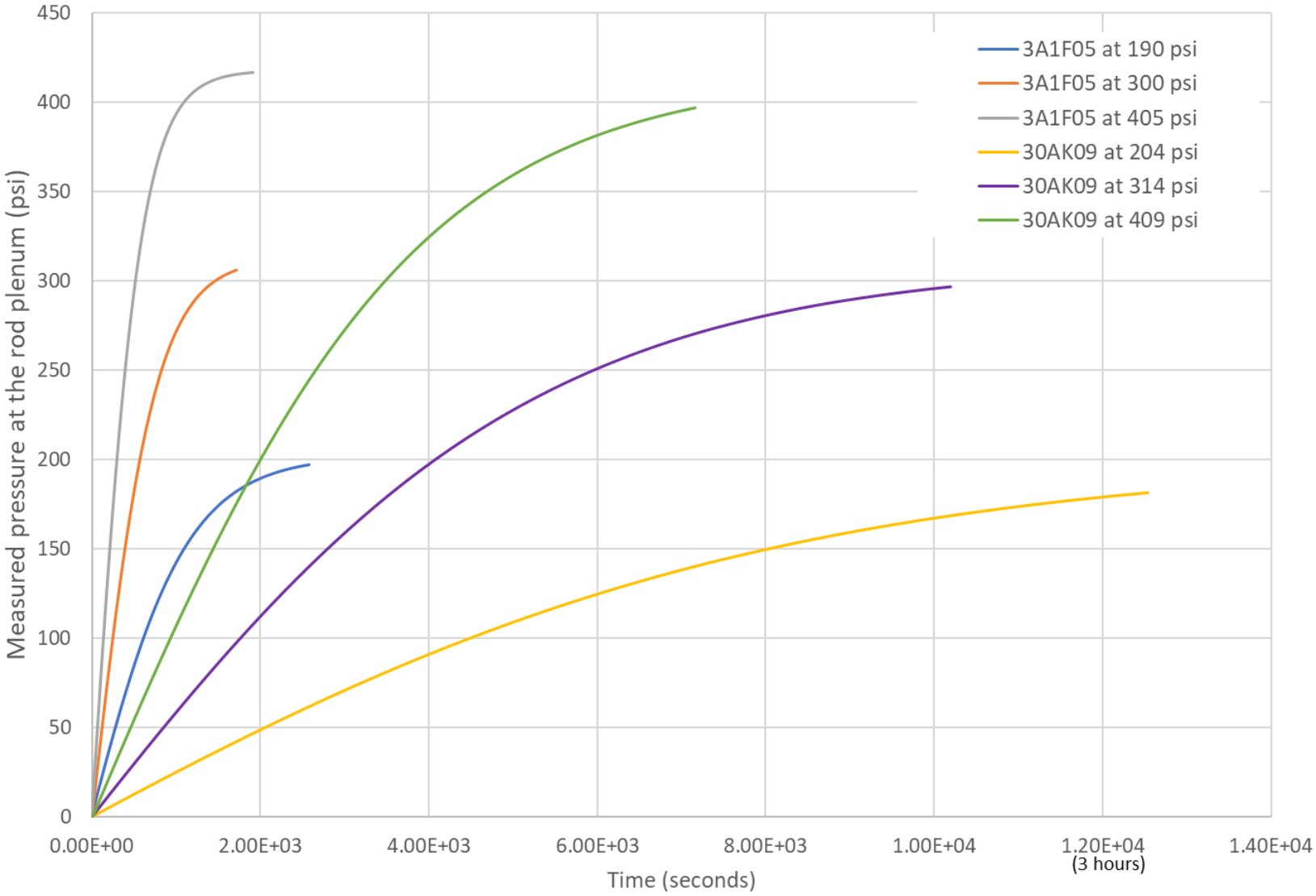

Figure 24. Results of Gas Transmission Tests on 2 Sister Rods (3 Different Pressures on Each Rod).

Figure 25 illustrates the predicted time versus pressure using the Muskat-Poiseuille correlation. The Muskat-Poiseuille prediction fits well, indicating the assumption of compressible gas flow is necessary and appropriate. For comparison purposes, the data was also fit using Darcy's Law (see Eq. B-8 in Appendix B), which assumes incompressible flow, and is plotted in Figure 25. As expected, the incompressible flow model predictions do not fit the data well. The average permeability for the HBU 17 × 17 PWR fuel rods is 4.25e-14 m^2 using the Muskat-Poiseuille model. These are about 20% of that measured by Rondinella [21] and correlated using Darcy's Law at 2e-13 m^2. If the average low-pressure Darcy porosity measured for the sister rods, 1.6e-13 m^2, is compared with Rondinella's results, the data are comparable if the same level of precision is applied. It is not clear how to relate the values provided by Desgranges [18] to the permeability constants produced by this work.

3A1F05 (LT Zirc-4) and F35P17 (heat treated Zirc-4) have the largest permeability values, but all rods are within an order of magnitude of each other, with the variance likely due to the wide variety of clads, pellets designs, and operating histories. Note that the higher the evaluated permeability, the more easily the fission gases can move through the pellet stack.

Regarding the three rods on which the gas transmission test was repeated at varying starting pressures, it appears that the permeability maintains a relatively constant value with pressure variation, as shown in Figure 26. For the tests results reported herein, the time constants ($1/\eta K$) are exaggerated because of the rather large tare volume associated with the hardware required for hot cell testing. Without the tare volume, the time constants are expected to be approximately ⅓ of that shown in the graphs. Although argon was used instead of helium, xenon, and krypton, the general results are not expected to be significantly influenced by the gas mixture if the proper viscosity is used.

To examine whether differences in rod operation resulted in different permeability, the evaluated Muskat-Poiseuille permeability was plotted against available operational parameters, including rod average burnup, high duty core index (HDCI)[22], and predicted assembly average middle-of-cycle fuel temperature, as shown in Figure 27. Unfortunately, while the average rod burnup for rod F35P17 is known [23], the rod's operating temperatures are not available at this time, so the values for HDCI and temperature shown are estimated. It appears that there is no close correlation with the rod's average burnup. Maximum rod HDCI appears to be somewhat correlated, as does the assembly's average fuel temperature. However, it is not clear if this is a global trend or if it is only related to this particular set of HBU fuel rods. The permeability does appear to be closely related to the rod manufacturer, as illustrated when the Muskat-Poiseuille permeability is plotted by cladding type (Figure 27d). Based on the results shown in Figure 27, it seems that the pellet manufacturing process and operating temperature determines the permeability of the pellet stack. Furthermore, the three rods that were heat-treated to simulate a dry storage vacuum drying environment (to the regulatory guidance temperature limit) are indicated on Figure 27. Although Figure 27 a, b and c do not provide conclusive evidence that the heat treatment affected the permeability, Figure 27d does strongly indicate that an offset in the permeability could have resulted from the heat treatment. However, there is not enough data available to reach the conclusion that a statistical difference exists.

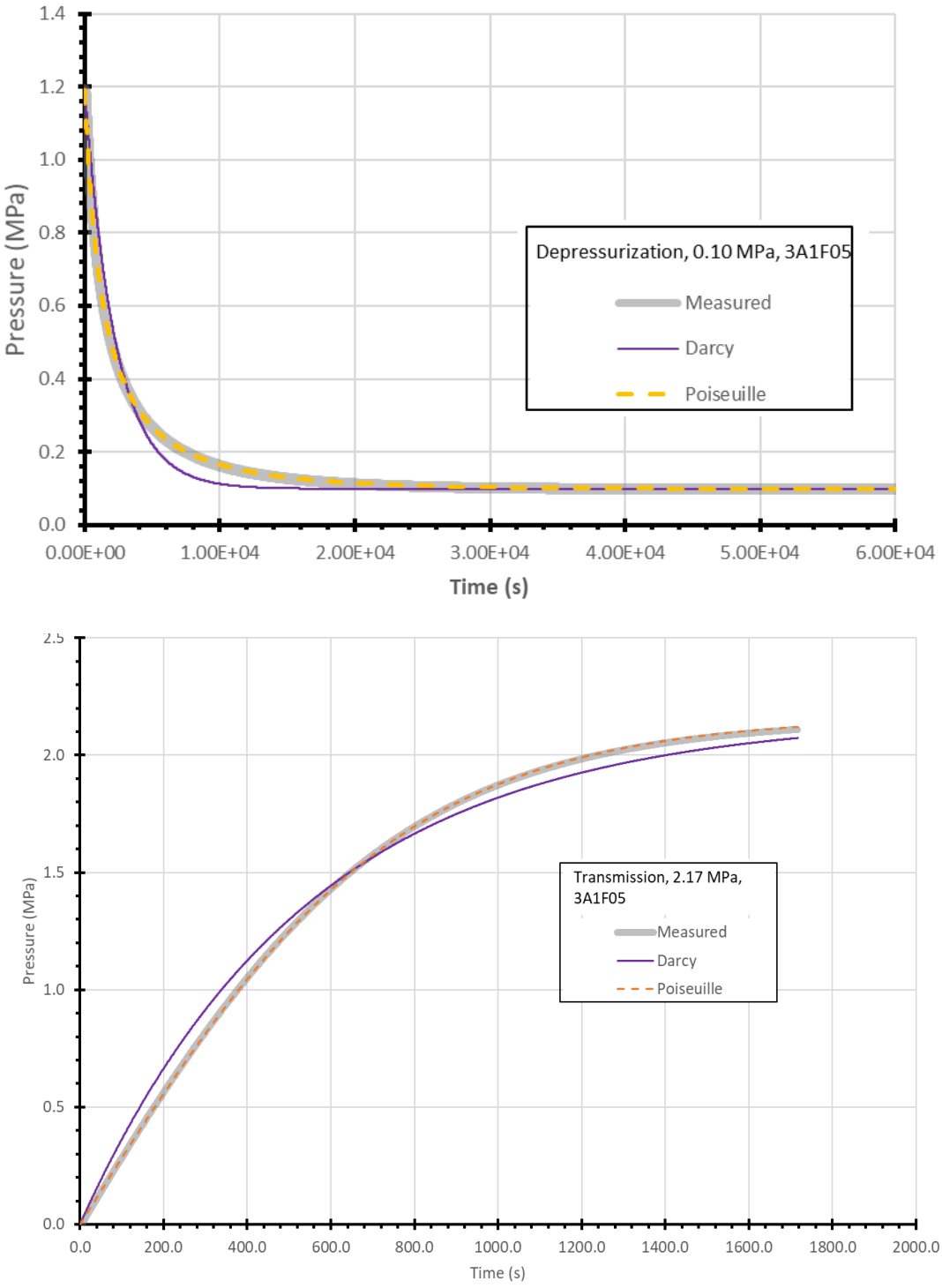

Figure 25. Pressure versus Time Predictions using the Muskat-Poiseuille Model for Compressible Gas Flow and Darcy's Law for Incompressible Flow for Sister Rod 3A1F05: Depressurization (top) and Gas Transmission (bottom) Test Results.

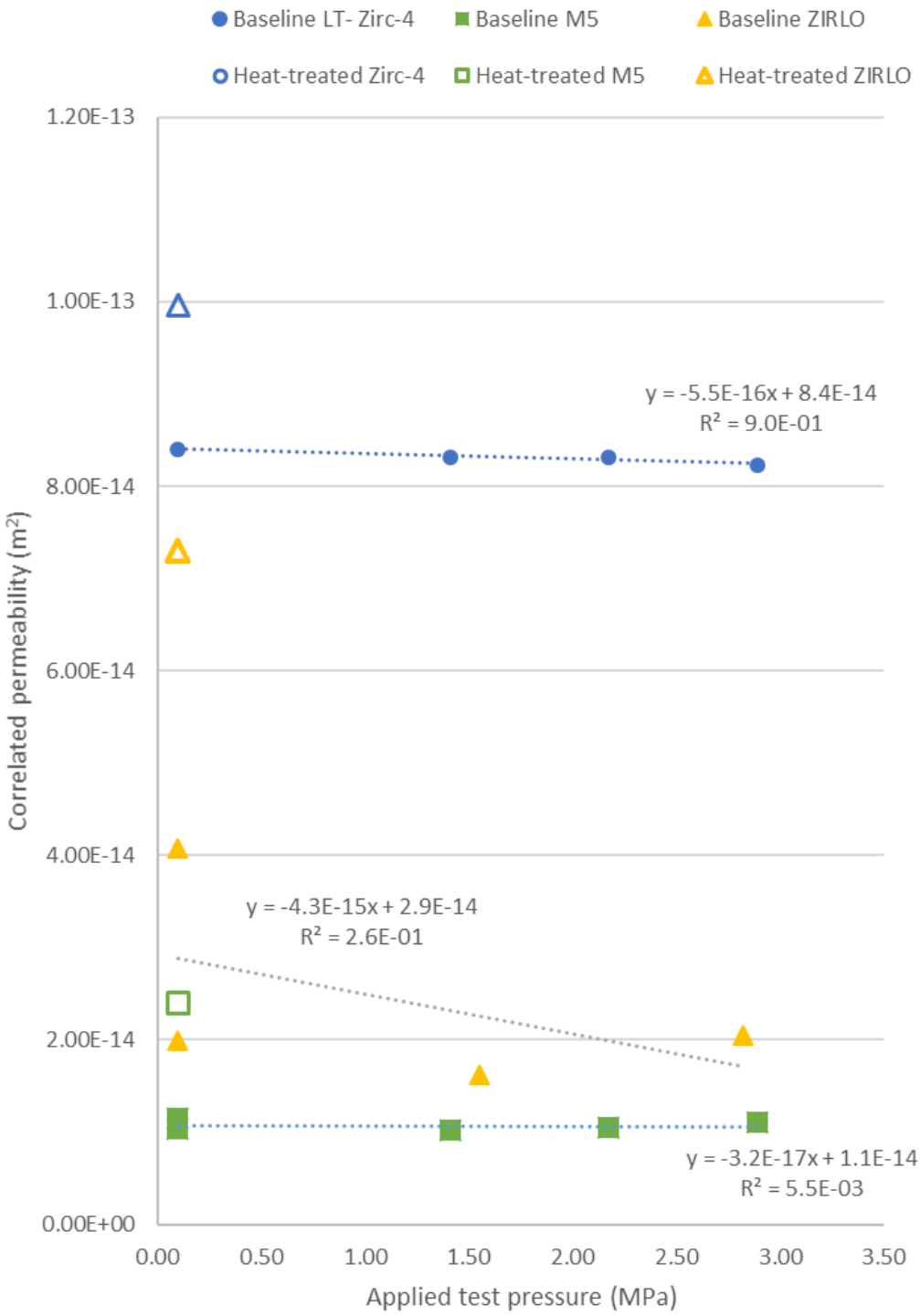

Figure 26. Evaluated Muskat-Poiseuille Permeability for Baseline Rods Subjected to Transmission Tests at Various Driving Pressures by Cladding Type and Heat-Treatment.

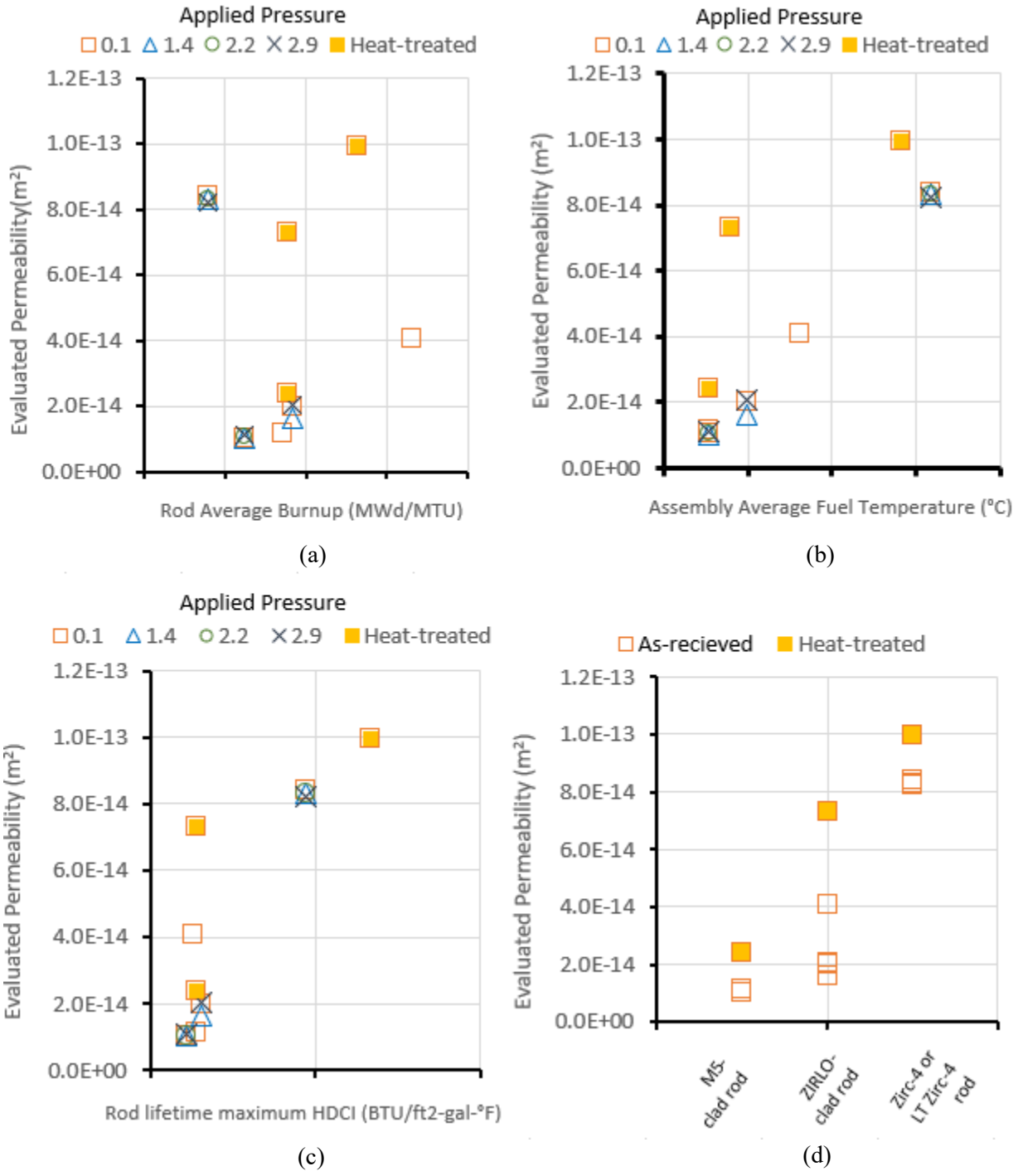

Note the abscissas values are not provided.

Figure 27. Evaluated Muskat-Poiseuille Permeability as a Function of (a) Rod Average Burnup, (b) Assembly Average Fuel Temperature during Operation, (c) Estimated Rod HDCI, and (d) Rod Cladding Type (Also Reflective of the Rod Manufacturer and Vintage).

7.2.3 Depressurization and Transmission Test Results Summary

Gas transmission and depressurization testing of eight HBU fuel rods revealed that gas communication from one end of the pellet stack to the other is unobstructed, but slow, at room temperature. The time constants derived were in the minutes to hours, depending on the starting pressure. Thus, one can expect gas equilibrium in the fuel rod over several hours, rather than in minutes or seconds. How this changes with rod temperature is not known at this time, but some change in permeability due to thermal expansion effects is expected.

The Muskat-Poiseuille model provides an acceptable model of the time-based flow of fission gases through the pellet stack with a convenient analytic expression. The permeability of the pellet stack varied over less than an order of magnitude for this set of rods which is modest and may indicate some common feature about HBU fuel. Graphs of the data with burnup, lifetime maximum HDCI, and operating lifetime average assembly middle-of-cycle predicted fuel temperature appear to indicate that the derived permeability is correlated to fuel temperature and maximum HDCI but is not correlated to the rod average burnup. The permeability does appear to be closely related to the rod's manufacturer and it seems that the pellet manufacturing process may be important in determining the permeability of the pellet stack.

While the flow regimes associated with the pellet stack flow did not change significantly for the heat-treated fuel rods, it appears that the heat treatments may have induced a shift to higher evaluated permeability, with some possible causes being a disruption of any pellet-cladding bonding, the development of additional cracks as a result of the thermal cycling, or expansion and permanent set of the cladding related to the additional pressure achieved inside the rod during the heat treatment. The role of the cladding in the resulting permeability shift is unclear.

Because the time constant of the system is strongly influenced by the applied driving pressure, measurements via puncture and evacuate/backfill type devices should be operated at pressures as high as practicable, or at least above 1.5 MPa at room temperature.

A natural extension of this work is to conduct the same tests at the fuel rod storage and transportation temperatures using a similar apparatus. Also, it would be prudent to measure gas transmissibility on rods that have been in dry storage for ~10 years to determine if the flow paths have become restricted.

7.3 Fission Gas Sample Isotopic Composition and Calculated Fission Gas Release

Before the system evacuation for the void volume measurement, a fission gas sample was taken from each punctured sister rod. Gaseous fission products evolve in all uranium dioxide nuclear fuel pellets at all axial elevations during reactor operation [24]. They are located near the site of the fission, within the fuel grains, at a grain boundary, or at free surfaces on the pellet. The gaseous fission products form small bubbles within the pellet since the xenon and krypton gases produced are virtually insoluble in UO_2. While much of the fission gas remains trapped within the fuel pellet microstructure as porosity, some fraction of the fission gas is released to the interior void volume of the fuel rod and contributes to an increase in the internal pressure of the fuel rod [25,26].

According to EPRI, less than 5% of the fission gas produced in the pellet stack during normal operation is released to the void volume of the rod [27]. The quantity of fission gas released from the pellet to the void volume of the rod during reactor operation has been the topic of much study because the gross rod pressure and localized rod pressure are important to rod performance during reactor transients such as loss-of-coolant accidents and reactivity-initiated accidents. The percentage of fission gas released is calculated as the moles of fission gas in the rod void volume divided by the total calculated fission gas produced during operation.

7.3.1 Low Pressure Fission Product Gas Analysis

The 8 sister rod samples were analyzed by the ORNL Nuclear Analytical Chemistry and Isotopic Laboratory. Fission gas isotopic (in atom %) and concentration (in mole%) determinations were made using an OmniStar GSD 320 Gas Analysis System (RGA) analyzer coupled to a sample manifold located within a radiological fume hood (Figure 28). The ion source and focus lens tune parameters are listed in Table 9.

Figure 28. The Sample Inlet Manifold (left) Coupled to an OmniStar GSD 320 Gas Analysis System (RCA) (right).

Table 9. Ion source and focus lens tune parameters for the RGA analyzer.

Parameter	Setting
Filament	No 1
Active set	Set 1
Emission current	0.50 A
Protection current	3.50 A
RF-Polarity	positive
Ion reference	150.00 V
Cathode	-50.00 V
Focus	-3.00 V
Field axis	-5.00 V
Extraction	-45.00 V

The RGA analyzer is equipped with two detectors, a Faraday that is used for all fission gas concentration measurements and a secondary electron multiplier (SEM) that can be used for low ppm gas concentration measurements. The SEM was not used for sister rod concentration measurements, but it was employed to confirm the precision of the Faraday isotopic measurements. Gas samples are scanned from 1 to 150 amu with either detector prior to starting the isotopic and mole percent determinations. These analog scans are carried out to detect potential unknown gasses present in samples, and to have a record of detected peak shape and peak resolution. The natural (using a gas standard) or fission isotopes (unknown samples) are measured using a multiple ion detection (MID) data acquisition program. Gas concentrations are then measured by quantification of Kr-84, Xe-132, and He-4 isotopes using a multiple concentration determination (MCD) program.

Quality control measures involved the analysis of two certified gas standard mixtures with different lot numbers. The primary standard is employed for calibration of the OmniStar GSD 320 Gas Analyzer and the secondary standard is analyzed for initial calibration verification and continuing instrument performance. The setup and calibration process of the OmniStar GSD 320 Gas Analysis (RGA) system involves an offset calibration with the evacuated sample manifold pressure controlled at 4 to 5 Torr. A mass scale adjustment and RGA ion source tuning are then performed with the certified mixed gas standard held at ~30 Torr in the sample manifold. Mass scale tuning, required for performance optimization, is performed when necessary. The final stage in the RGA setup is a second mass scale adjustment using a fine mass calibration setting and the same standard gas. The result of the calibration is verified with the secondary mixed gas standard held at the same pressure.

To perform measurements of the sister rod fission gas samples, the sample bottle used in the rod puncture sequence (see Section 7.1.1) is attached to the evacuated sample manifold for the measurement sequence. The known volume of the sample manifold is 18.4 mL, and the volume and pressure of each of the sister rod gas samples is known. The sample gas is allowed to expand into the manifold until gas pressure reaches equilibrium. The sample manifold pressure is recorded and then reduced to ~30 Torr prior to injection of the sample into the RGA for analysis. Argon gas (99.999% purity) is used to flush the sample manifold between gas analyses and for verification testing. NIST tracible mixed gas standards from independent lots are used for calibration and verification testing, and these contain a gas mixture that is 5.00 mol% krypton, 5.00 mol% xenon, 1.05 mol% oxygen, 3.96 mol% nitrogen, and the remaining 85.00 mol% is helium. The individual gas concentrations in the mixed gas standards are certified with a blend tolerance and certified accuracy of ±2%, and the certified test gas standards used are listed in Table 10.

Table 10. Matheson certified verification standards used for sister rod fission gas analysis.

Calibration-	Lot No:	1028601078B	Exp.	4/20/2021
Verification-	Lot No:	1027603245B	Exp.	12/8/2020

7.3.2 Sister Rod Gas Sample Measurement Results

Measured gas concentrations for the 8 sister rod gas samples collected during the rod puncture operation (see Section 7.1) are provided in Table 11. Six of the sister rod samples were measured as many as three times on non-consecutive days and the determined fission gas concentrations were averaged for those samples. The concentrations measured were determined by linear regression monitoring Kr-84 and Xe-132, which are naturally occurring isotopes present at 56.99 and 26.91 atom%, respectively. The isotopic concentration in the sister rod samples was determined by measuring the current responses corresponding to the Kr-84 and Xe-132 isotopes and comparing those to the current response of the known concentration calibration standards. The total uncertainty values reported are the combined uncertainties of the duplicate measurements at a 95% level of confidence. The number of digits in the reported mole% and their uncertainties is provided for information and is not intended to convey a significant degree of reliability.

Table 11. Sister rod gas sample measured elemental composition, mole%*

	Sample ID			
Detected gas**	30AK09 (M5) SR-Gr-02	30AD05 (M5) SR-Gr-05	30AE14 (M5, heat treated) SR-Gr-06	3A1F05 (LT Zirc-4) SR-Gr-04
Krypton	1.60 ± 0.15	1.41 ± 0.19	1.45 ± 0.22	1.97 ± 0.25
Xenon	15.31 ± 1.33	14.10 ± 0.70	14.11 ± 1.49	18.46 ± 1.72
Helium***	83.09 ± 1.10	84.49 ± 0.59	84.44 ± 1.62	79.57 ± 1.83

	Sample ID			
Detected gas**	6U3K09 (ZIRLO) SR-Gr-01	3D8E14 (ZIRLO) SR-Gr-03	3F9N05 (ZIRLO, heat treated) SR-Gr-07	F35P17 (Zirc-4, heat treated) SR-Gr-08
Krypton	1.11 ± 0.10	2.36 ± 0.30	2.23 ± 0.30	1.93 ± 0.25
Xenon	10.45 ± 1.47	22.44 ± 1.41	20.08 ± 2.01	19.87 ± 1.99
Helium***	88.44 ± 1.41	75.20 ± 1.41	77.69 ± 1.62	78.20 ± 1.62

* Reported uncertainties are the total combined uncertainties at the 95% level of confidence. Two decimal places are provided in the reported values for information only and is not intended to imply a significant degree of reliability. The precision contribution for samples 01-06 was the standard deviation of the values measured in August 2018 and September 2018. As only a single data set was measured for samples 07 and 08, for conservatism the precision contribution to the total uncertainty for those data was taken as the worst-case scenario observed for samples 01-06.

** Some residual air present in the sampling system was detected and the resulting oxygen and nitrogen content has been neglected when determining the fission gas component percentages and FGR in the fuel rod (see Table 14).

***The measured helium includes the pre-pressurization helium and any helium produced as fission/decay products.

In general, based on inspection of Table 11, there is good agreement between the M5 rods and the LT Zirc-4 and Zirc-4 clad rods. However, per Table 11, one ZIRLO rod (6U3K09) appears to have about half of the fission gas content (Kr and Xe) as compared with two other ZIRLO rods that have been measured at ORNL. When the PNNL sister rod data [11] are included in the dataset, as illustrated in Figure 29, it becomes clear that 6U3K09 is consistent with the remainder of the dataset, while the other two ORNL-measured ZIRLO rods instead appear to be too high with the deviation not explained by measurement uncertainty.

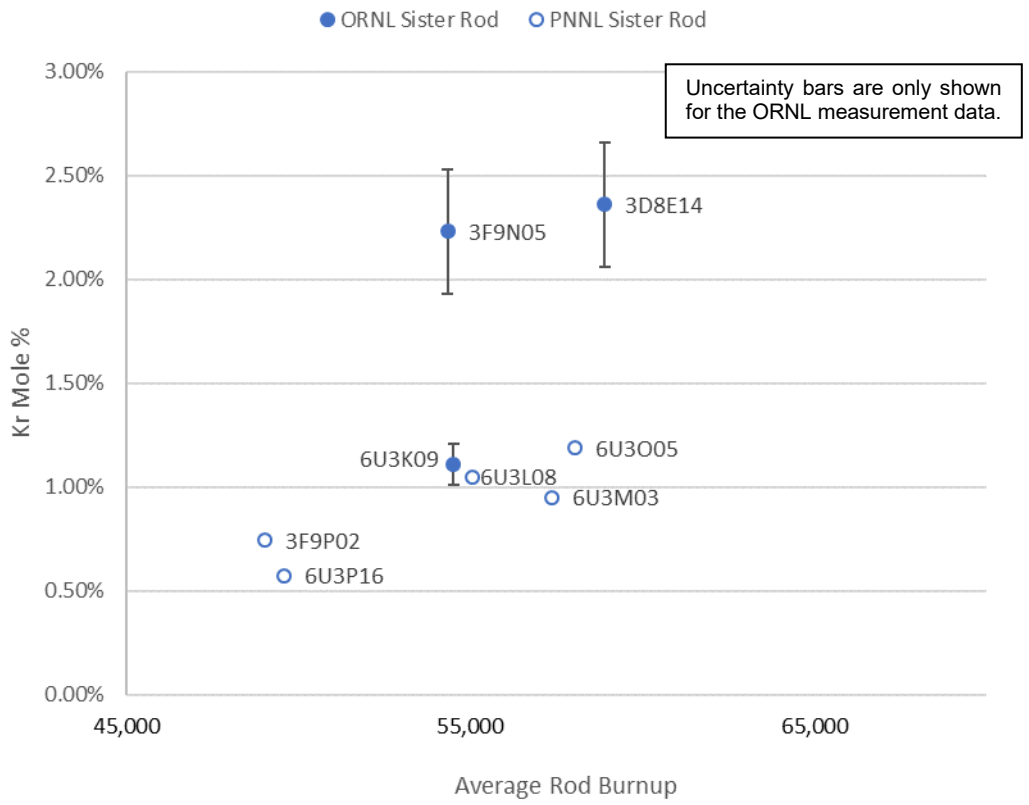

Figure 29. The Measured Kr Content of the Rod Fission Gas for ZIRLO-clad Sister Rods.

When all of the data are plotted as a function of the independently measured fission gas partial pressure, the data appears to be consistent, as shown in Figure 30, with the exception of one Zirc-4 rod (F35K13), which is ~1.4 MPa above other sister rods. Based on Figure 30, it appears that the differences in the measured rod fission gas composition of the two ZIRLO-clad rods are simply a consequence of higher fission gas release for those rods. Although not shown here, when Xe is graphed, the same trends are observed. All of the sister rods (regardless of cladding alloy) have a different operational duty. The source of higher fission gas release will be investigated once more detailed information on the measured rod burnup and predicted rod fission gas production are available.

Isotopic data, reported in Table 12 and Table 13 , were determined using the ion currents acquired from the MID run and includes both natural and fission product krypton and xenon isotopes. The isotopic composition of natural krypton and xenon in both primary and secondary standards were evaluated and compared with isotopic data sourced from the National Nuclear Data Center [28] to ensure analytical accuracy. The uncertainties reported in Table 12 are a single standard deviation from the calculated mean, where n=2-4, with the exception of SR-Gr-07 and -08, where only one measurement was completed. For those two samples, the averaged observed standard deviation for the other six samples was applied. The uncertainties reported in Table 13 are the 2σ standard deviations from the calculated mean, where n=2-4, with the exception of SR-Gr-07 and -08, where only one measurement was completed. For those two samples, the largest observed uncertainty from the other six samples was applied. The number of digits in the reported atom % and their uncertainties is provided for information and is not intended to convey a

significant degree of reliability. Some small bias in the measurement data was observed but was within the measurement uncertainty; no corrections were applied. Additionally, three independent measurements of selected sister rod samples were performed on three different dates between August 2018 and February 2019. The Faraday detector was utilized to generate most of the isotopic data; however, the SEM was also employed for three of the fission gas samples in February 2019 to verify the precision of the Faraday measurements. The results of the three SEM measurements were incorporated into the uncertainty calculations for the measured samples

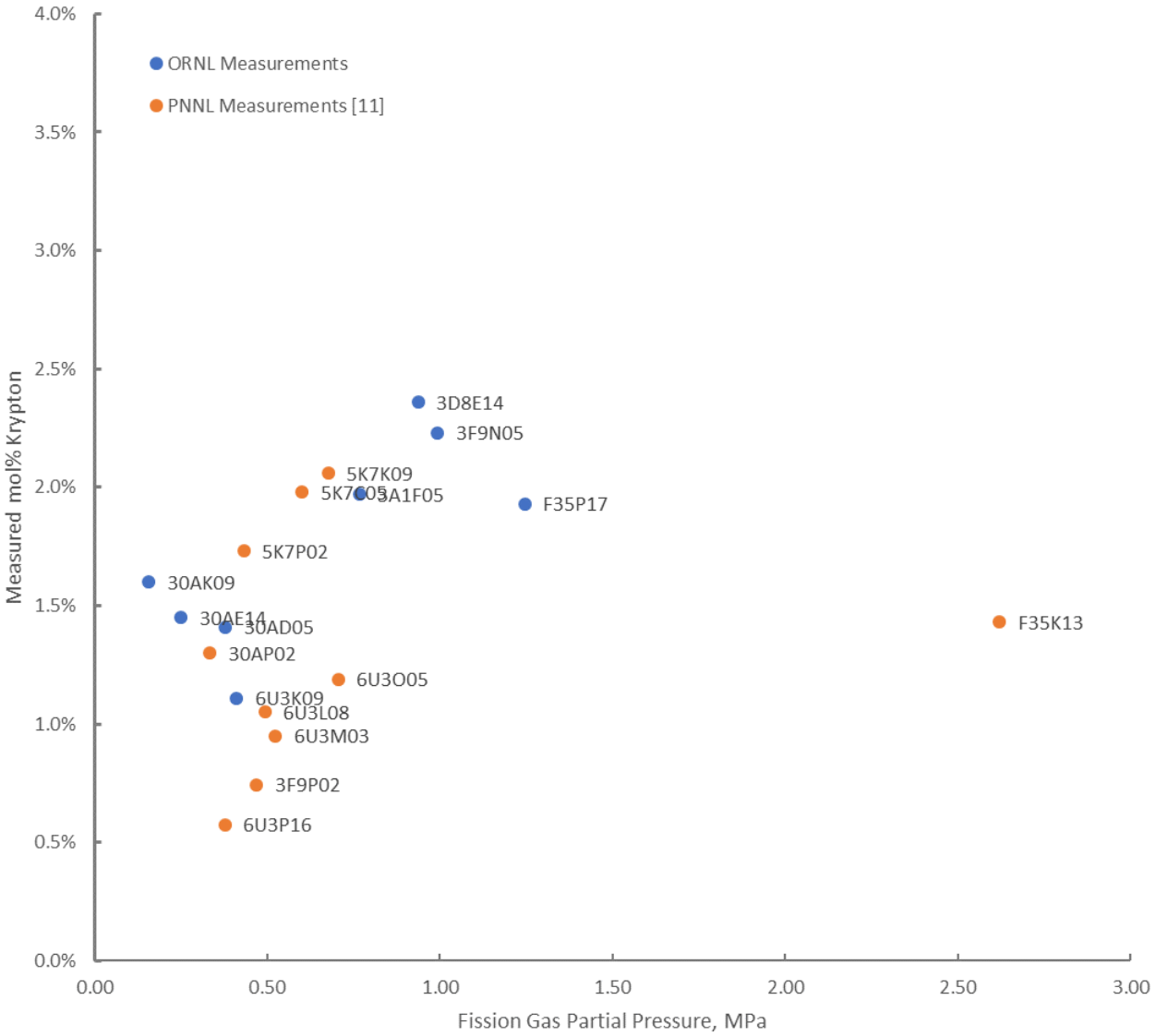

Figure 30. Measured Kr Content of the Rod Fission Gas as a function of the Independently Measured Fission Gas Partial Pressure.

Table 12. Fission gas isotope ratios, atom% ratio

Sample	30AK09 (M5)			30AD05 (M5)			30AE14 (M5, heat treated)			3A1F05 (LT Zirc-4)		
Isotope Ratio	SP-Gr-02*			SP-Gr-05*			SP-Gr-06*			SP-Gr-04*		
$^{82}Kr/^{84}Kr$	0.021	+/-	0.009	0.018	+/-	0.007	0.019	+/-	0.008	0.023	+/-	0.003
$^{83}Kr/^{84}Kr$	0.322	+/-	0.009	0.307	+/-	0.008	0.318	+/-	0.010	0.310	+/-	0.002
$^{85}Kr/^{84}Kr$***	0.121	+/-	0.007	0.121	+/-	0.008	0.123	+/-	0.009	0.059	+/-	0.003
$^{86}Kr/^{84}Kr$	1.533	+/-	0.014	1.525	+/-	0.009	1.535	+/-	0.011	1.512	+/-	0.000
$^{128}Xe/^{132}Xe$	0.005	+/-	0.003	0.005	+/-	0.003	0.006	+/-	0.003	0.007	+/-	0.004
$^{130}Xe/^{132}Xe$	0.012	+/-	0.002	0.012	+/-	0.002	0.013	+/-	0.001	0.015	+/-	0.001
$^{131}Xe/^{132}Xe$	0.278	+/-	0.004	0.289	+/-	0.003	0.296	+/-	0.002	0.293	+/-	0.004
$^{134}Xe/^{132}Xe$	1.178	+/-	0.006	1.173	+/-	0.022	1.178	+/-	0.011	1.165	+/-	0.033
$^{136}Xe/^{132}Xe$	1.689	+/-	0.029	1.661	+/-	0.055	1.654	+/-	0.029	1.647	+/-	0.080
Sample	6U3K09 (ZIRLO)			3D8E14 (ZIRLO)			3F9N05 (ZIRLO, heat treated)			F35P17 (Zirc-4, heat treated)		
Isotope Ratio	SP-Gr-01*			SP-Gr-03*			SP-Gr-07**			SP-Gr-08**		
$^{82}Kr/^{84}Kr$	0.016	+/-	0.005	0.022	+/-	0.004	0.033	+/-	0.010	0.034	+/-	0.011
$^{83}Kr/^{84}Kr$	0.311	+/-	0.005	0.277	+/-	0.001	0.310	+/-	0.006	0.278	+/-	0.005
$^{85}Kr/^{84}Kr$***	0.100	+/-	0.004	0.073	+/-	0.004	0.088	+/-	0.005	0.050	+/-	0.003
$^{86}Kr/^{84}Kr$	1.537	+/-	0.008	1.474	+/-	0.007	1.530	+/-	0.008	1.469	+/-	0.008
$^{128}Xe/^{132}Xe$	0.005	+/-	0.003	0.007	+/-	0.004	0.011	+/-	0.006	0.011	+/-	0.006
$^{130}Xe/^{132}Xe$	0.012	+/-	0.002	0.015	+/-	0.002	0.019	+/-	0.002	0.018	+/-	0.002
$^{131}Xe/^{132}Xe$	0.278	+/-	0.004	0.254	+/-	0.005	0.290	+/-	0.004	0.249	+/-	0.003
$^{134}Xe/^{132}Xe$	1.178	+/-	0.006	1.126	+/-	0.033	1.156	+/-	0.018	1.094	+/-	0.017
$^{136}Xe/^{132}Xe$	1.689	+/-	0.029	1.582	+/-	0.083	1.600	+/-	0.048	1.545	+/-	0.046

* Uncertainty for samples defined as a 1σ external standard deviation of the replicate analyses (for 01, 03, and 04 n=2, for 02, 05, and 06 n=4).

** For SP-Gr-07 and 08 only one replicate was performed the assigned uncertainties are the averages of the other six samples.

*** ^{85}Kr was decay corrected to February 2019 in each case.

Table 13. Fission gas isotopic composition, atom %*

Sample	30AK09 (M5)	30AD05 (M5)	30AE14 (M5, heat treated)	3A1F05 (LT Zirc-4)
Isotope	SP-Gr-02*	SP-Gr-05*	SP-Gr-06*	SP-Gr-04*
^{82}Kr	0.69 ± 0.34	0.59 ± 0.30	0.64 ± 0.32	0.81 ± 0.40
^{83}Kr	10.73 ± 0.32	10.34 ± 0.31	10.62 ± 0.32	10.67 ± 0.32
^{84}Kr	33.37 ± 0.67	33.65 ± 0.67	33.39 ± 0.67	34.43 ± 0.69
^{85}Kr ****	4.04 ± 0.20	4.08 ± 0.20	4.12 ± 0.21	2.03 ± 0.10
^{86}Kr	51.17 ± 0.51	51.33 ± 0.51	51.24 ± 0.51	52.06 ± 0.52
^{128}Xe	0.14 ± 0.07	0.13 ± 0.07	0.17 ± 0.09	0.16 ± 0.08
^{129}Xe	< 0.05	< 0.05	< 0.05	< 0.05
^{130}Xe	0.31 ± 0.16	0.30 ± 0.15	0.39 ± 0.19	0.36 ± 0.18
^{131}Xe	7.09 ± 0.35	6.98 ± 0.35	6.38 ± 0.32	7.11 ± 0.36
^{132}Xe	23.97 ± 0.48	24.16 ± 0.48	25.14 ± 0.50	24.24 ± 0.48
^{134}Xe	28.39 ± 0.57	28.33 ± 0.57	28.30 ± 0.57	28.23 ± 0.56
^{136}Xe	40.15 ± 0.40	40.10 ± 0.40	39.74 ± 0.40	39.90 ± 0.40
Sample	6U3K09 (ZIRLO)	3D8E14 (ZIRLO)	3F9N05 (ZIRLO, heat treated)	F35P17 (Zirc-4, heat treated)
Isotope	SP-Gr-01*	SP-Gr-03*	SP-Gr-07**	SP-Gr-08**
^{82}Kr	0.56 ± 0.28	0.77 ± 0.39	1.10 ± 0.55	1.20 ± 0.60
^{83}Kr	10.49 ± 0.31	9.75 ± 0.29	10.45 ± 0.31	9.83 ± 0.29
^{84}Kr	33.74 ± 0.67	35.14 ± 0.70	33.74 ± 0.67	35.30 ± 0.71
^{85}Kr ****	3.36 ± 0.17	2.56 ± 0.13	3.06 ± 0.15	1.81 ± 0.09
^{86}Kr	51.85 ± 0.52	51.78 ± 0.52	51.63 ± 0.52	51.86 ± 0.52
^{128}Xe	0.12 ± 0.06	0.17 ± 0.09	0.27 ± 0.20	0.28 ± 0.21
^{129}Xe	< 0.05	< 0.05	< 0.05	< 0.05
^{130}Xe	0.29 ± 0.15	0.39 ± 0.19	0.46 ± 0.23	0.45 ± 0.23
^{131}Xe	6.68 ± 0.33	6.38 ± 0.32	7.12 ± 0.36	6.36 ± 0.32
^{132}Xe	24.03 ± 0.48	25.14 ± 0.50	24.54 ± 0.49	25.54 ± 0.51
^{134}Xe	28.31 ± 0.57	28.30 ± 0.57	28.36 ± 0.57	27.92 ± 0.56
^{136}Xe	40.57 ± 0.41	39.74 ± 0.40	39.25 ± 0.39	39.44 ± 0.39

* Reported numerical uncertainties are the 2σ external standard deviation of all duplicate analyses. The last digit in the measurements and uncertainties is provided for information and is not intended to convey a significant degree of reliability. The accuracy of the analysis was confirmed using a NIST tracible standard, and a bias correction did not measurably alter the data within the uncertainty of the 2σ standard deviation.

** SR-Gr-02, 05, and 06 also incorporate the uncertainty between two different modes of mass analysis, namely SEM, and Faraday.

*** SR-Gr-07 and 08 only one replicate analyzed, for conservatism the uncertainty attributed to those data was taken as the worst-case scenario observed for samples 01-06.

**** ^{85}Kr was decay corrected to February 2019 in each case.

Table 14 provides the measured xenon-to-krypton ratio for the sister rod samples. The ratios are within the expected range, as illustrated in Figure 31, where the Xe/Kr ratio for the sister rods are graphed with other publicly available data for PWR-type fuel [36,37,38]. Serna [36] presented fission gas release and Xe/Kr ratio data for ZIRLO-clad 17×17 fuel rods enriched to 4.5wt% ^{235}U operated over 5 cycles to discharge burnups up to 75 GWd/MTU. Park [37] provided data on Zirc-4 or ZIRLO-clad 17×17 and 14×14 fuel rods enriched from 3.21 to 4.5wt% ^{235}U operated over 3 cycles. Bibilashvili [38] summarized data available for model validation of water-water energetic reactor (VVER) rods. Although the VVER rods are slightly smaller in diameter (9.1 mm VVER versus sister rods 9.5 mm nominal design outer diameter) they are similar in mechanical design and are operated in a PWR-type reactor. The reactor operating conditions and cycle lengths of the comparison rods shown in Figure 31 are somewhat different from typical US commercial power operation; however, even with the operational differences, the Xe/Kr ratios were consistent. The Xe/Kr ratio was also evaluated to determine if there was any additional Xe or Kr preferentially released as a result of the heat treatments performed on three of the sister rods; based on the data available, if additional fission gas is released as result of the heat treatment, it does not significantly affect the proportion of Xe to Kr released.

The predicted xenon-to-krypton ratio and the predicted fission gas production during operation are not yet available, so the calculated percentage of fission gas released from the pellets to the void volume of the rod (FGR) are not yet available. Once the predicted fission gas production is available, the FGR of the baseline and heat-treated rods will be compared to determine if the heat treatment resulted in additional fission gas release to the rod void volume.

Table 14. Measured xenon-to-krypton ratio for the sister rods.

Rod ID / Condition	Cladding type	Measured Xe/Kr
30AK09 / baseline	M5	9.6
30AD05 / baseline	M5	10.0
30AE14 / heat treated	M5	9.7
6U3K09 / baseline	ZIRLO	9.4
3D8E14 / baseline	ZIRLO	9.5
3F9N05 / heat treated	ZIRLO	9.0
3A1F05 / baseline	LT Zirc-4	9.4
F35P17 / heat treated	Zirc-4	10.3

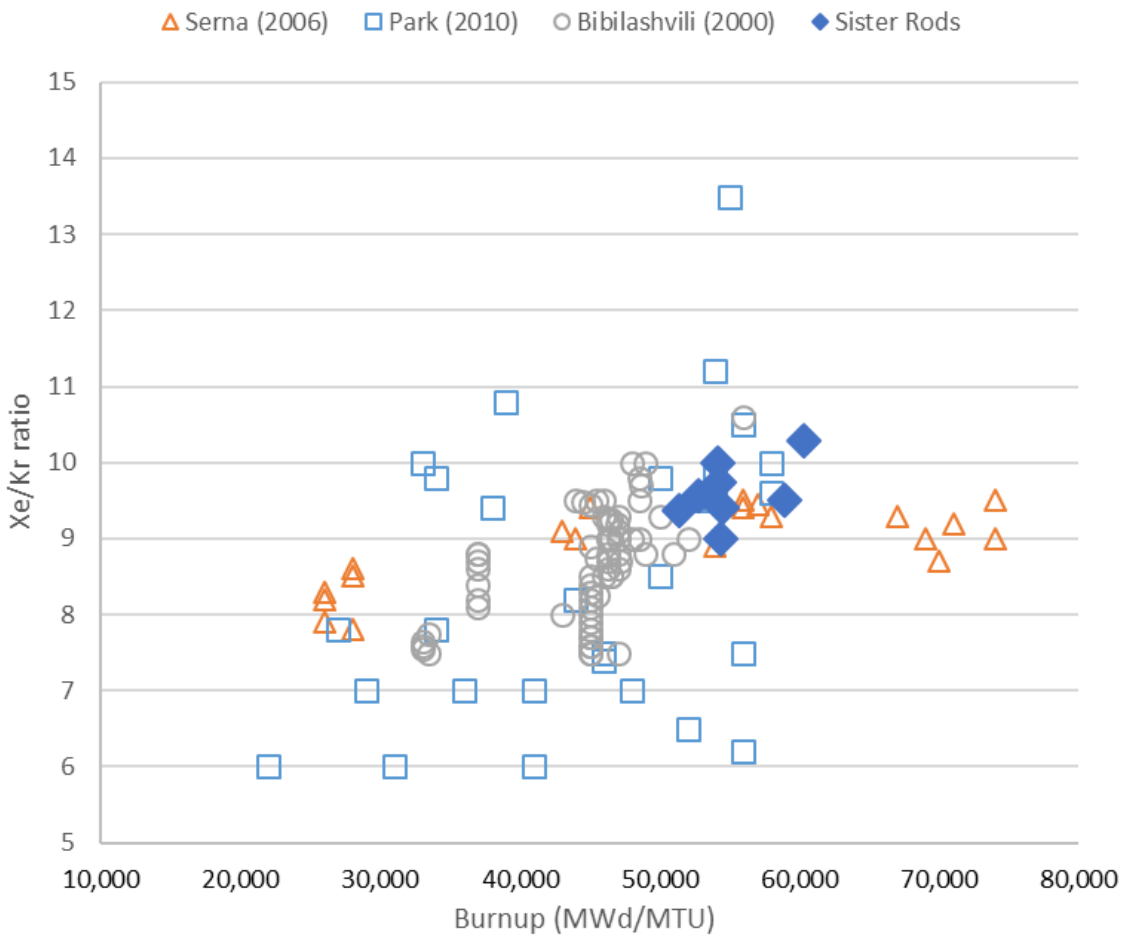

Figure 31. Xe-to-Kr Ratio for the Sister Rods Measured.

7.4 Fuel Burnup Measurements

Six specimens have been sent to the ORNL Radiochemical Engineering Development Center for burnup analysis (Nd, U, Pu only). Additionally, other sponsors are funding isotopic analysis of additional sister rod specimens (~51 isotopes measured). The specimens cover the range of the Phase 1 sister rods being mechanically tested and will verify the code-predicted rod burnups and validity of linear scaling of gamma scan profiles. Table 15 indicates the specific specimens being analyzed for fuel burnup.

8. METALLOGRAPHY (DE.02)

The rough-cut DE.02 segments provide material for several exams (Table 15), including metallographic mounts (METs), total cladding hydrogen analysis, microhardness, scanning electron microscope (SEM), and transmission electron microscope (TEM) imaging. The first step in the DE.02 process is to cut appropriate specimens from the segments for the other exams. Approximately ⅓ of the Phase 1 DE-02 segments have been sub-sectioned. Higher priority specimens (blue shading) and segments with specimens slated for burnup or isotopic measurements have been sub-sectioned.

METs are currently available for two M5-clad sister rods (Figure 32); while they contain many polishing artifacts, some indications at the ID of the heat-treated rod's cladding appear to be radially-oriented hydrides that have nucleated on a pellet crack. It is not clear, based on just these two images, whether the radial hydrides were present prior to the heat treatment or if the heat-treatment of the M5-clad sister rod induced hydride reorientation. MET mounts are also available for one ZIRLO-clad sister rod that was heat-treated (Figure 33, two rod elevations, three different sections mounted) and one Zirc-4-clad sister rod that was heat-treated (Figure 34, one rod elevation, two different sections mounted). The heat-treated ZIRLO MET at the highest burnup elevation shows some ~35 μm radial hydrides that nucleated on the rod ID, and a ~60 μm long radial hydride near the rod ID. The heat-treated Zirc-4 MET does not show any radial hydrides, but the contrast on the available images is not sufficient to fully define the hydride precipitates. Some of the sections will be etched to improve the contrast between the cladding and the hydride precipitates. Several additional metallographic mounts are in progress.

Measurements of the cladding thickness, waterside oxide thickness, pellet-side oxide thickness, and high burnup rim regions have been completed and the averages for the MET elevations are provided in Figure 32, Figure 33, and Figure 34. The NDE provided measurements of the waterside oxide thickness and minimum remaining cladding wall thickness using eddy current methods [4]. The cladding wall thickness measurements from the METs are consistent with those measured using eddy current. As discussed in the NDE report [4], the waterside oxide thickness varies around the circumference of the cladding. At this time, complete circumferential measurements are not available using the METs, but the point measurements taken are consistent with the eddy current measurements at that elevation for some azimuthal locations. For example, the eddy current measured oxide thickness (liftoff) for 30AD05 at 3,240 mm in elevation varies from 4 to 18 μm for the 0°, 90°, 180°, and 270° scans, while the Figure 32 MET average waterside oxide thickness is 11 μm. Also, the waterside oxide thickness reported using eddy current at the elevation of the for F35P17 MET shown in Figure 34 is 80 to 121 microns, while the MET measurements indicate a thickness of 73 to 86 microns.

Table 15. Selected metallographic, total cladding hydrogen, microhardness, fuel isotopic and fuel burnup specimens (in order of decreasing priority).

Rod	Originating segment elevation range (mm)		Selection criteria	MET	Total cladding H_2	Micro-hardness specimen	Fuel burnup measure-ment
30AD05	2,783	2,802	HBU region	✓	✓	✓	
30AD05	3,240	3,259	Highest oxide	✓	✓	✓	
30AE14	2,675	2,694	HBU at oxide peak	✓	✓	✓	
30AE14	3,399	3,418	Highest oxide thickness	✓	✓	✓	
3A1F05	2,735	2,754	High oxide thickness at HBU	✓	✓	✓	
3A1F05	3,105	3,124	Peak oxide thickness	✓	✓	✓	
3D8E14	2,655	2,674	HBU with oxide spike	✓	✓	✓	
3D8E14	3,206	3,225	Highest oxide thickness	✓	✓	✓	✓
3F9N05	2,863	2,882	HBU with higher oxide	✓	✓	✓	
3F9N05	3,331	3,350	Peak oxide thickness, spalling oxide, pellet banding	✓	✓	✓	
F35P17	2,735	2,754	Oxide thickness, spalling oxide, pellet banding	✓	✓	✓	
F35P17	3,050	3,069	Peak oxide thickness, spalling oxide, pellet banding	✓	✓	✓	✓
3D8E14	1,375	1,450	Pellet-pellet gap, oxide thickness	✓	✓	✓	✓
30AD05	2,410	2,429	HBU region with higher oxide	✓	✓	✓	
6U3K09	2,616	2,635	CIRFT correlating data	✓		✓	
6U3K09	3,506	3,525	CIRFT correlating data	✓		✓	✓
3F9N05	700	719	Oxide thickness	✓		✓	
3F9N05	1,425	1,444	Oxide thickness	✓	✓	✓	
3F9N05	2,300	2,329	Oxide thickness	✓		✓	
3D8E14	2,303	2,322	Oxide thickness	✓		✓	
3D8E14	700	719	Oxide thickness	✓		✓	✓
3A1F05	2,383	2,402	HBU with higher oxide thickness, spalling oxide, pellet banding	✓	✓	✓	
30AE14	2,203	2,222	High burnup at oxide peak	✓			
30AD05	678	697	Oxide thickness	✓			
30AD05	1,280	1,299	Oxide thickness	✓	✓		
30AE14	653	672	Oxide thickness	✓			
30AE14	1,677	1,696	Oxide thickness	✓	✓		
3A1F05	1,260	1,279	Oxide thickness	✓		✓	
3A1F05	1,585	1,604	Oxide thickness	✓			
3A1F05	2,006	2,025	Oxide thickness	✓	✓	✓	
F35P17	911	930	Oxide thickness	✓			
F35P17	1,300	1,319	Oxide thickness	✓	✓		
F35P17	2,008	2,027	HBU with higher oxide thickness	✓			
F35P17	2,383	2,402	Oxide thickness, spalling oxide	✓		✓	✓
3D8E14	1,178	1,331	Fretting mark depth (post CIRFT)	✓		✓	

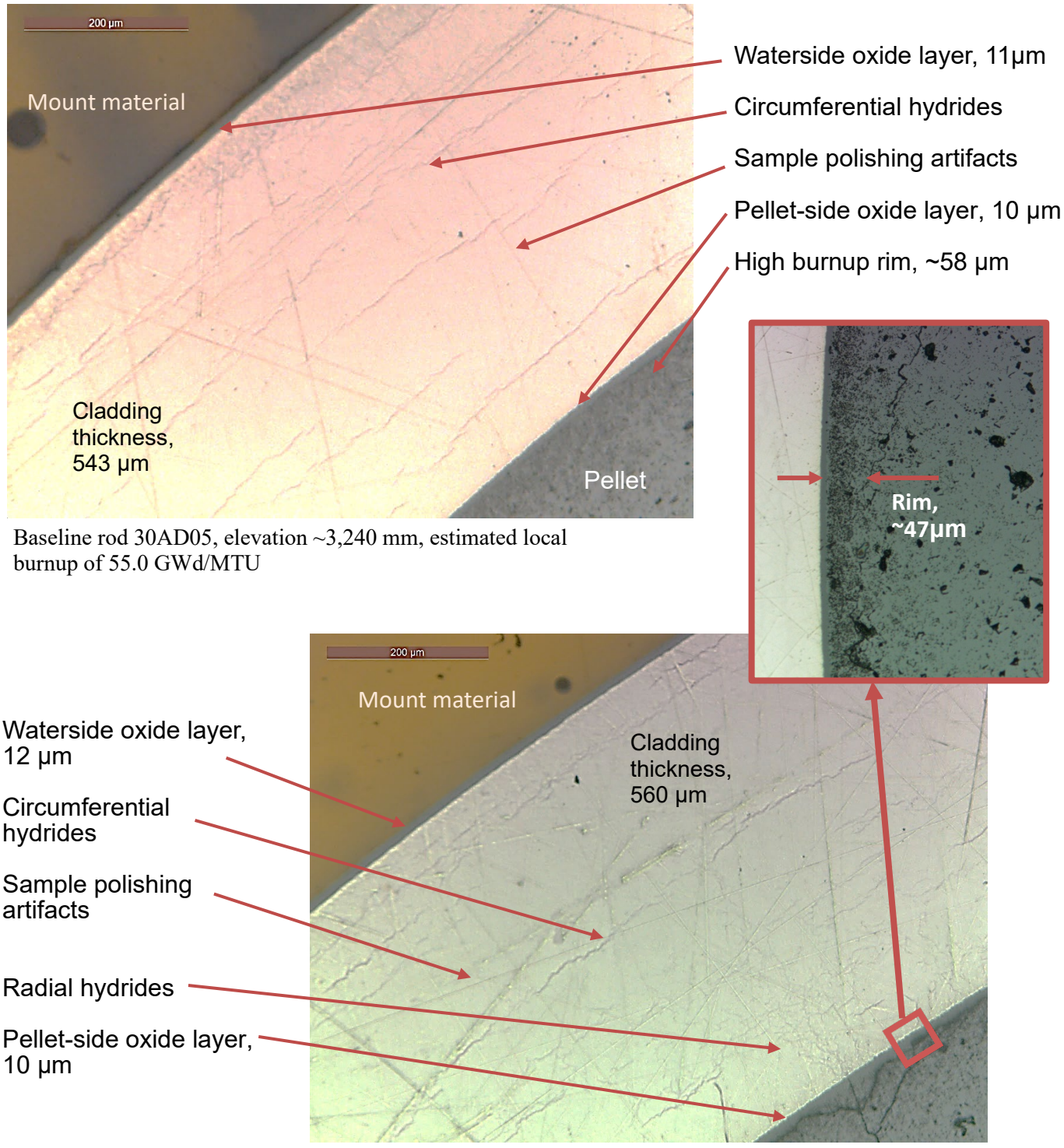

Baseline rod 30AD05, elevation ~3,240 mm, estimated local burnup of 55.0 GWd/MTU

Heat-treated rod 30AE14, elevation ~3,399 mm, estimated local burnup of 50.1 GWd/MTU

Figure 32. Selected MET Views of M5-clad Sister Rods 30AD05 (Baseline) and 30AE14 (Heat-Treated).

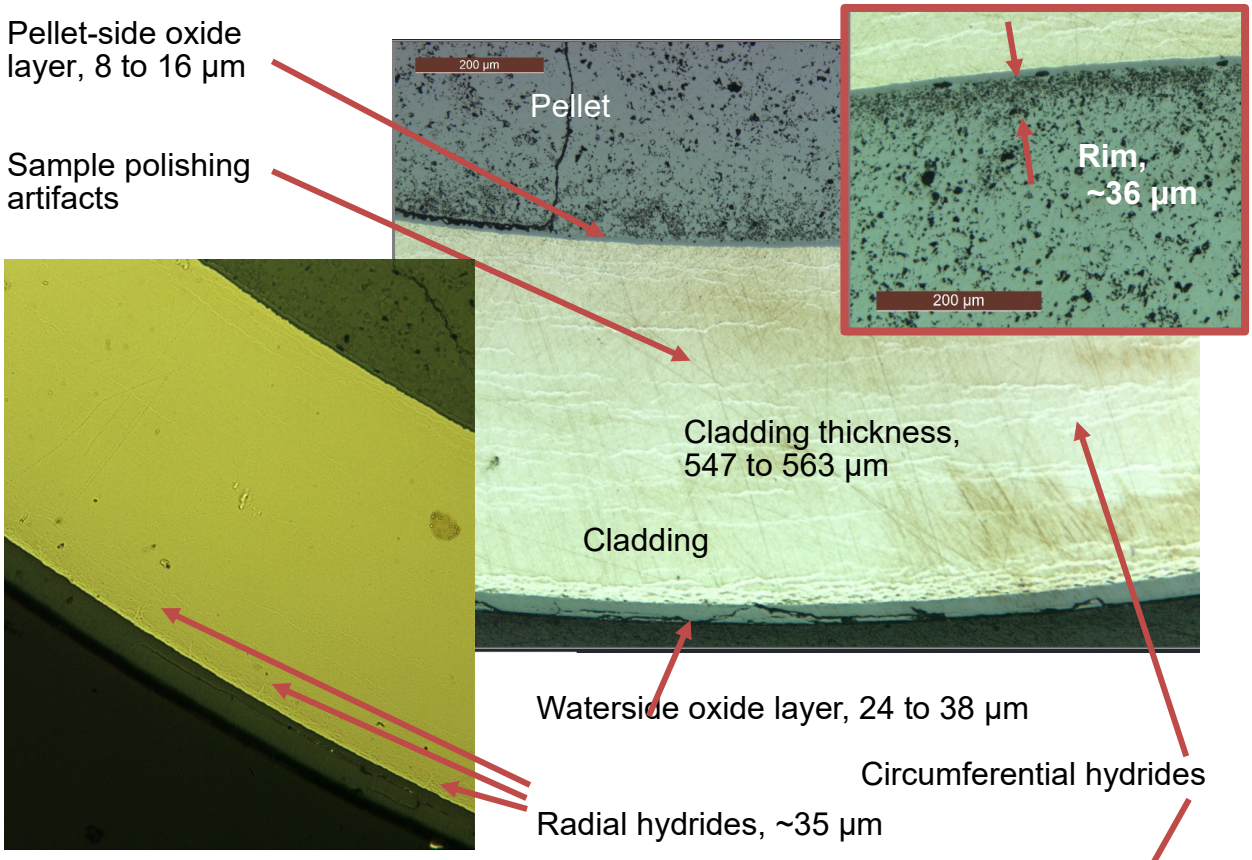

Heat-treated rod, elevation ~3,331 mm, local estimated burnup of 50.6 GWd/MTU

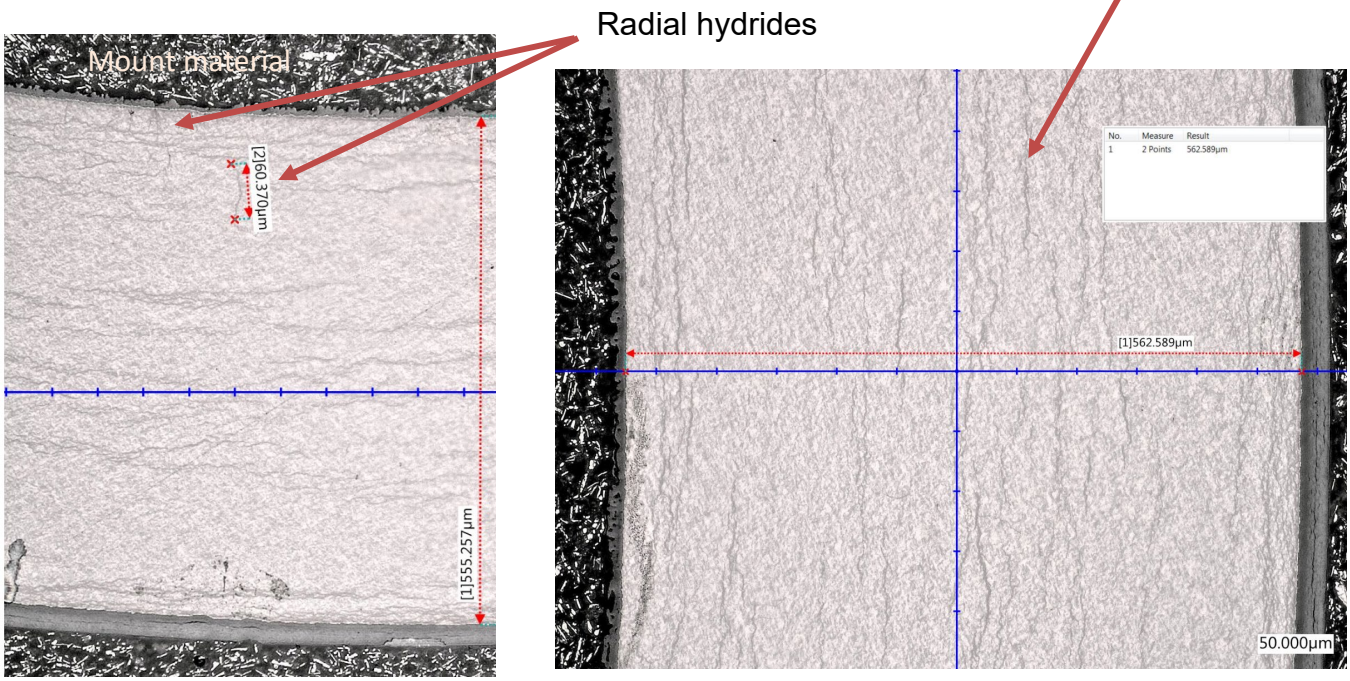

Heat-treated rod, elevation ~2,863 mm, local estimated burnup of 57.8 GWd/MTU

Figure 33. Selected MET Views of ZIRLO-clad Sister Rod 3F9N05 (Heat-Treated).

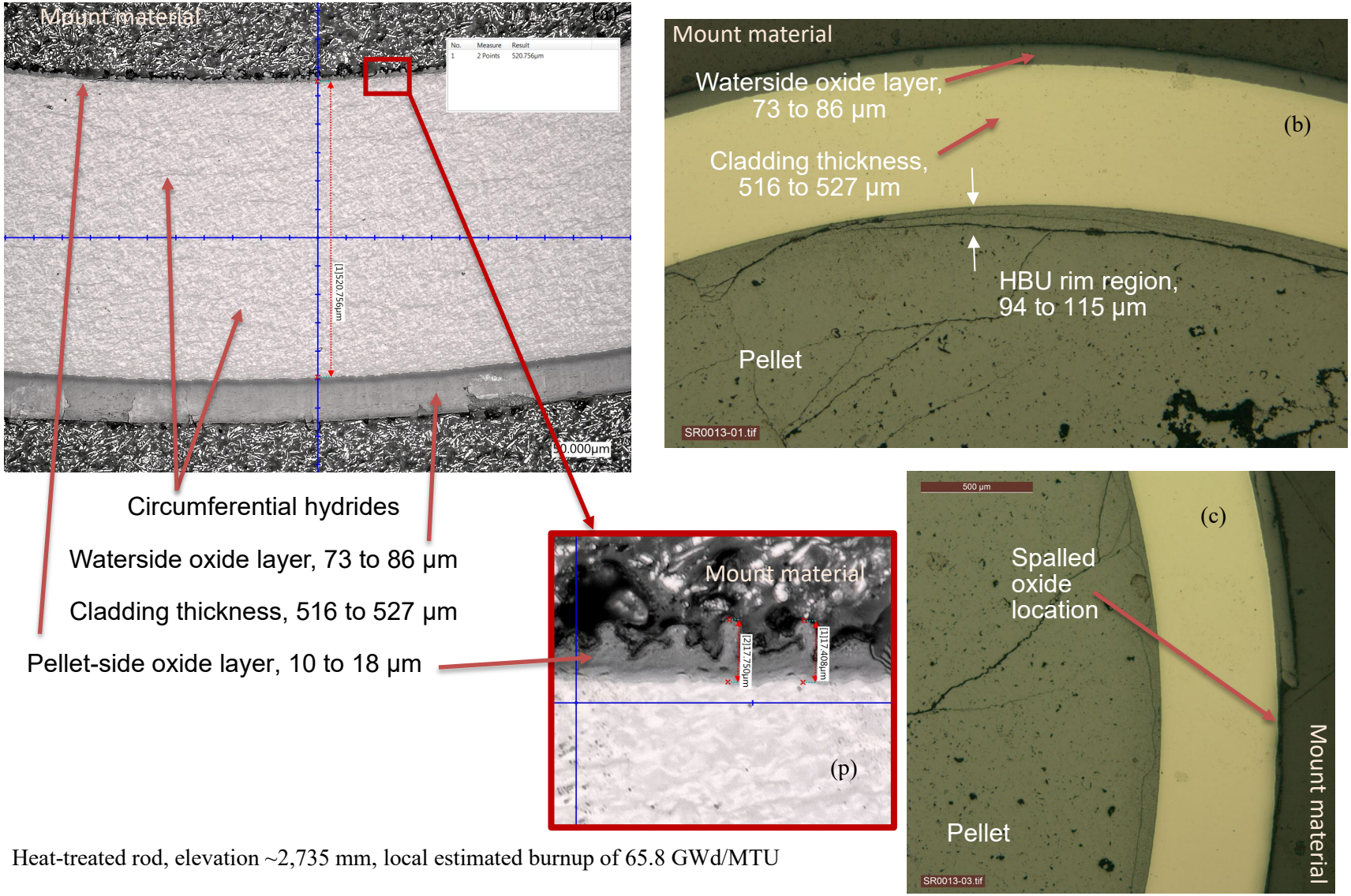

Heat-treated rod, elevation ~2,735 mm, local estimated burnup of 65.8 GWd/MTU

Figure 34. Selected MET Views of Heat-treated Zirc-4-clad Sister Rod F35P17

This page is intentionally left blank.

9. CLADDING HYDROGEN MEASUREMENTS (DE.03)

Table 15 lists the segments that were sub-sectioned to include cladding total hydrogen specimens. The specimens to be used for total hydrogen analysis are 4 mm long. The specimens for total cladding hydrogen analysis will be cut, defueled, and sectioned azimuthally into 4 quadrants to obtain a minimum sample size of 0.1 g.

As mentioned previously, approximately ⅓ of the Phase 1 DE-02 segments have been sub-sectioned. The higher priority specimens (shown in blue shading in Table 15) and segments with specimens slated for burnup measurements have been sub-sectioned. The total cladding hydrogen specimens are available, and defueling has begun. As soon as defueling of the priority specimens is complete, the total cladding hydrogen measurements will begin (estimated start, last quarter 2019).

This page is intentionally left blank.

10. CIRFT TESTING (DE.05)

Table 16 lists the segments selected for CIRFT. Testing began in January 2019 and is expected to continue into FY2020 for the Phase 1 sister rods. All CIRFT tests are completed at room temperature.

Wang et al [30,31] describes the conditions and implications of the various parameters used within the CIRFT. For the reader's convenience, a short description of the test is provided here. ORNL developed the CIRFT in 2012 and has accumulated a significant amount of data for rods having Zirc-4, M5, and Zirc-2 cladding. As illustrated in Figure 35, the test rig consists of a U-frame with two rigid arms, connecting plates, and universal testing machine links. A rod specimen (cladding with pellets) is coupled to the test rig arms with two specially designed grips. The U-frame is oriented in a horizontal plane and is driven by Bose dual linear motors based on electromagnetic force. Linear motions applied at the loading points of the rigid arms impose a bending moment on the sister rod specimen at a frequency of 5–10 Hz. Three linear variable differential transformers (LVDTs) are used to measure the deflection of the rod specimen at three points along its longitudinal axis, and they are also used to determine the curvature of the rod during the test. The specimen curvature imposed during the test is correlated to the applied moment to characterize the mechanical properties of the rod and to calculate the alternating stress and strain on the cladding.

In specifying the loading conditions for the CIRFT tests, the previous body of data for M5 and Zirc-4 clad fuel rods was surveyed. The following hypothesis was constructed as an approach to selecting the test parameters:

- The M5 and Zirc-4 clad sister rod fatigue performance is consistent with the data given in the established database for those cladding alloys, and the sister rod test results should fit within existing data.
- FHT does not change the response mode of the cladding/rod to the fatigue test, and when compared with non-FHT segments, the results of the FHT segments should be within test uncertainty.
- Grid-to-rod fretting (GTRF) marks do not result in a reduced fatigue lifetime, even when they are aligned with the maximum cladding strain during the test.
- ZIRLO cladding fatigue performance is consistent with the data given in the established database for other cladding alloys, and the ZIRLO sister rod test results should fit within the extents of existing CIRFT data.

The tests were prescribed to provide data that can prove or disprove the hypotheses listed above, and paired baseline/heat-treated samples are provided as needed. Rod 6U3K09 was used to fill in other loads for the ZIRLO cladding material. Specimens with GTRF marks were prepared to align the GTRF marks with the maximum strain location, as possible. Specimens with pellet-pellet gaps will be tested also.

As mentioned previously, the sister rods are tested statically and dynamically as paired samples having similar burnup and oxide thicknesses:

a. **Baseline rod specimens:** 1 specimen tested statically followed by a dynamic test at a relatively high load (~175 N-m); 1 specimen tested dynamically at a moderate load (~10 to 12 N-m), and 1 specimen tested dynamically at a low load (~5–6 N-m);

b. **Heat-treated rod specimens:** 1 specimen tested statically followed by a dynamic test at the same load used for the baseline specimen; 1 specimen tested dynamically at the same moderate load used for the baseline specimen, and 1 specimen tested dynamically at the same low load used for the baseline specimen.

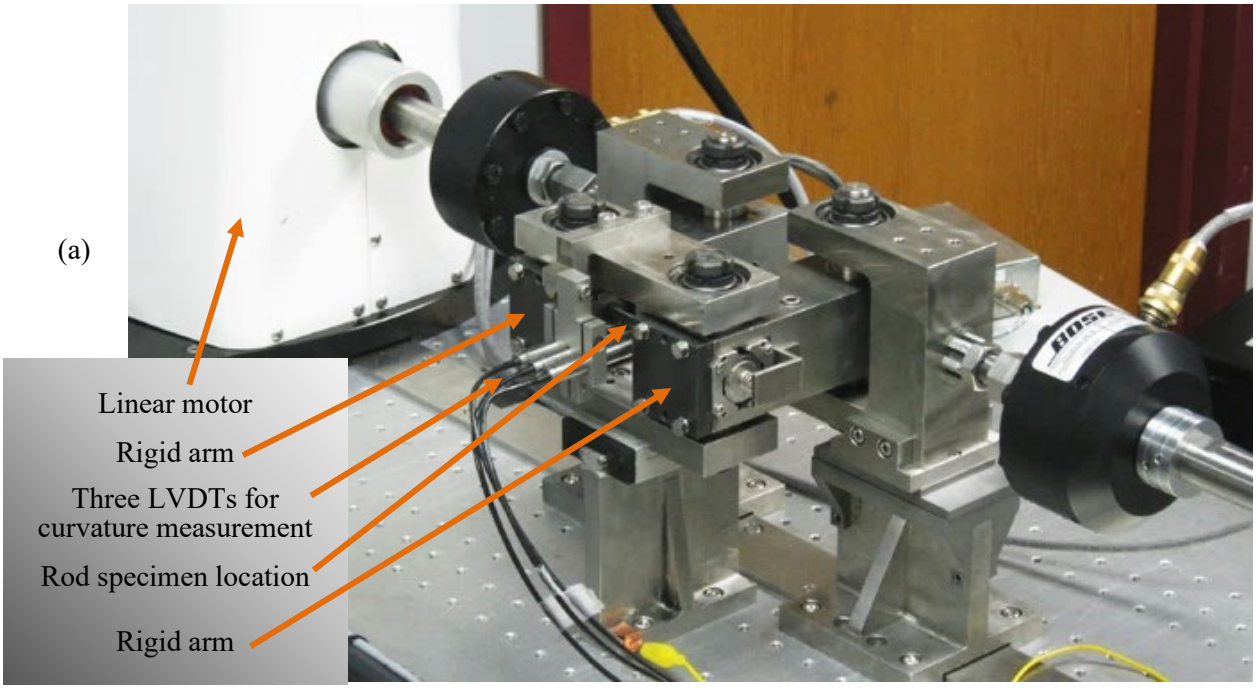

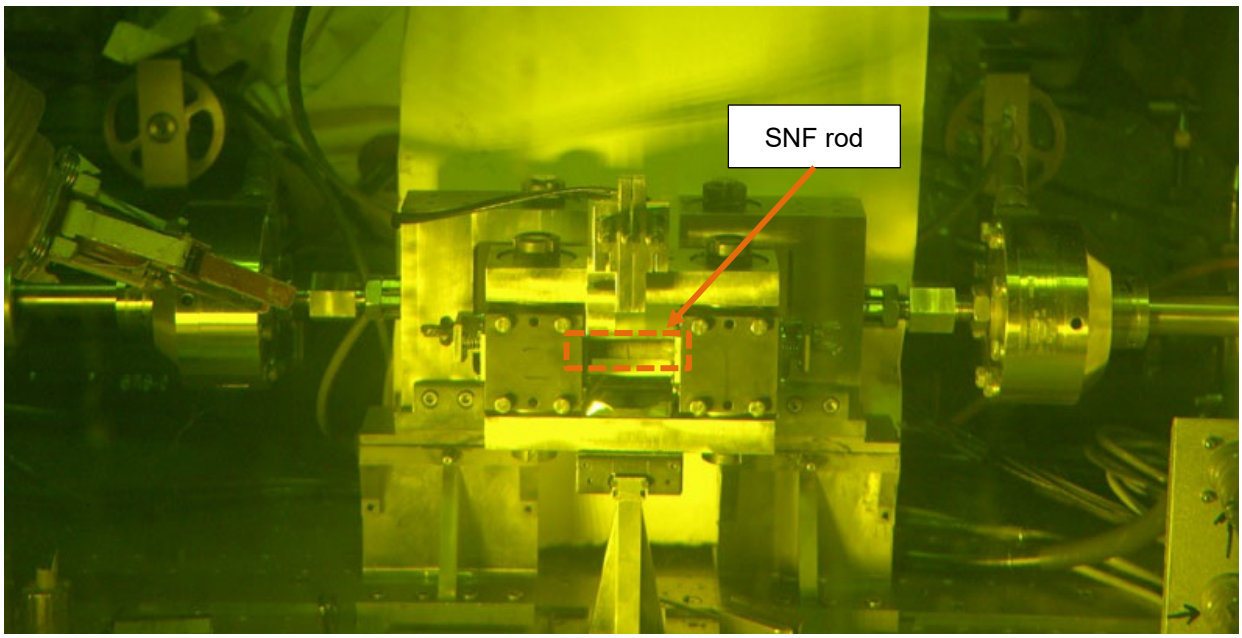

(b)

Figure 35. Two Views of the ORNL CIRFT: (a) a Surrogate Rod Specimen Undergoing Out-of-Cell Testing with 3 LVDTs in Place for Curvature Measurements and (b) an SNF Rod Being Tested in the Hot Cell.

At this time, 13 tests of 28 planned tests for Phase 1 have been completed, and initial results are available for all cladding types except the heat-treated ZIRLO cladding; however, additional tests must be completed before the complete range of applied bending moments are available. Figure 36 plots the applied bending moment with the number of cycles to failure measured for completed tests with the available previous data [30,31]. Figure 37 plots the strain amplitude versus the number of cycles to failure for those tests where an extended analysis of the test data is available (10 of the 13 tests). The results appear to be consistent with previous data for the same size of fuel rods (17×17). Upon inspection, it appears that there could be an effect related to the heat treatments, as in all cases to-date the heat-treated rods fractured at fewer cycles than in the corresponding baseline rod. One specimen with visible GTRF marks was tested with the marks aligned (as possible) with the highest cladding strain location, and the GTRF marks did not reduce the fatigue lifetime. Note that the GTRF marks on this particular specimen are not considered representative or bounding; the specimen was selected based on availability only.

The static test is performed to measure the flexural rigidity of representative specimens for each sister rod category – M5-clad, ZIRLO-clad, Zirc-4 or LT Zirc-4-clad, both baseline and heat-treated. The static test applies a larger deflection than is typically applied during dynamic tests. The flexural rigidity is also measured during each dynamic test at the applied load for the test. While the static specimens are tested in dynamic mode following the static test, it should be noted that the results are not strictly comparable to the dynamic-only test results, as the static specimens are flexed prior to the dynamic test, and the applied flexure may reduce the flexural strength of the rod. The results are provided for information.

The flexural rigidity of each rod specimen tested can be evaluated based on the CIRFT data, and this has been completed for 10 of the 13 tests completed to date. The flexural rigidity measured for the sister rod specimens at the beginning of the test are plotted with the estimated specimen burnup given in Figure 38, along with the measured flexural rigidity of other rods tested at ORNL using CIRFT [30,31]. The sister rod data are consistent with data from other 17×17 rods and appears to be relatively constant with burnup. There are not enough data available at this time to assess any effects on flexural rigidity of the heat-treatments applied to three of the sister rods. It should be noted that the flexural rigidity of the specimens does change over the CIRFT test, and a rod that has been subjected to many bending cycles is expected to have a lower flexural rigidity, based on past CIRFT data.

The stress amplitude can be plotted as a function of the number of cycles to failure to map the fatigue lifetime of the rods, as shown in Figure 39 for the 10 tests where an extended analysis has been completed. The sister rod fatigue lifetime appears to be on the lower side of other lifetime estimates [32-34], with the heat-treated sister rods below all other estimates. Some of the data are below the simulation-based fatigue curve [34].

Equipment for performing the cumulative shock tests has been developed and is currently being tested out of cell. The design, shown in Figure 40, incorporates an electromagnet and weight and uses gravity to deliver one or more impacts to the CIRFT specimen prior to fatigue testing. The parameters for the impact (impact load, number of impacts) have not yet been established. Cumulative tests are planned to begin in FY20.

Table 16. CIRFT test pairing and results to date

Specimen ID (parent rod – lower elevation – upper elevation in mm)			Cladding type	Heat treat-ment	Zone	Load applied (N-m)	Measured Cycles to failure	Comments/Notes
30AD05	697	850	M5	None	zone1	17.8	3,368	Dynamic test followed static (extended analysis results not yet available)
30AD05	2,050	2,203	M5	None	zone1	6.1	133,000	Dynamic test
30AD05	2,630	2,783	M5	None	zone1	12.2	22,315	Dynamic test
30AD05	3,732	3,886	M5	None	Zone 3			Dynamic test with pellet-pellet gaps
30AE14	672	825	M5	FHT	zone1	17.8	1,717	Dynamic test followed static
30AE14	2,850	3,003	M5	FHT	zone1	12.2	8,795	Dynamic test
30AE14	3,156	3,309	M5	FHT	zone1	6.1	112,000	Dynamic test
3A1F05	1,853	2,006	LT Zirc-4	None	zone1	17.8	1,300	Dynamic test followed static (extended analysis results unavailable)
3A1F05	2,025	2,178	LT Zirc-4	None	zone1			Dynamic test
3A1F05	3,214	3,367	LT Zirc-4	None	grid6			Dynamic test, no grid marks visible.
F35P17	2,027	2,180	Zirc-4	FHT	zone1	5.1	1,300,000	Dynamic test
F35P17	1,855	2,008	Zirc-4	FHT	zone1	17.8	525	Dynamic test followed static; cycled twice (extended analysis results unavailable)
F35P17	3,159	3,312	Zirc-4	FHT	zone1	10.2	773	Dynamic test
3D8E14	719	872	ZIRLO	None	zone1	17.8	9,589	Dynamic test to follow static (extended analysis results unavailable)
3D8E14	2,412	2,565	ZIRLO	None	zone1	6.1	191,156	Dynamic test
3D8E14	2,963	3,116	ZIRLO	None	zone1			Dynamic test
3D8E14	1,178	1,331	ZIRLO	None	Grid2	6.1	211,000	Dynamic test, GTRF mark expected to be visible
3F9N05	719	872	ZIRLO	FHT	zone1			Dynamic test to follow static
3F9N05	2,329	2,482	ZIRLO	FHT	zone1			Dynamic test
3F9N05	2,710	2,863	ZIRLO	FHT	grid5			Dynamic test, fretting mark difficult to see.
6U3K09	2,310	2,463	ZIRLO	None	zone1			If necessary, static test followed by dynamic test; otherwise, dynamic test
6U3K09	2,463	2,616	ZIRLO	None	zone1			Dynamic test
6U3K09	2,635	2,788	ZIRLO	None	zone1			Dynamic test
6U3K09	3,200	3,353	ZIRLO	None	grid6			Dynamic test, fretting marks not visible
6U3K09	3,353	3,506	ZIRLO	None	zone2			Dynamic test
30AD05	3,452	3,605	M5	None	Zone3			Cumulative damage test
30AE14	3,003	3,156	M5	FHT	zone1			Cumulative damage test
3A1F05	3,367	3,520	LT Zirc-4	None	zone2			Cumulative damage test
3D8E14	3,225	3,378	LT-Zirc-4	None	Zone 1			Cumulative damage test
3F9N05	3,440	3,593	ZIRLO	FHT	Zone2			Cumulative damage test
F35P17	3,312	3,465	Zirc-4	FHT	zone2			Cumulative damage test

Colors = test pairs

GTRF marks will be oriented with maximum strain if possible.

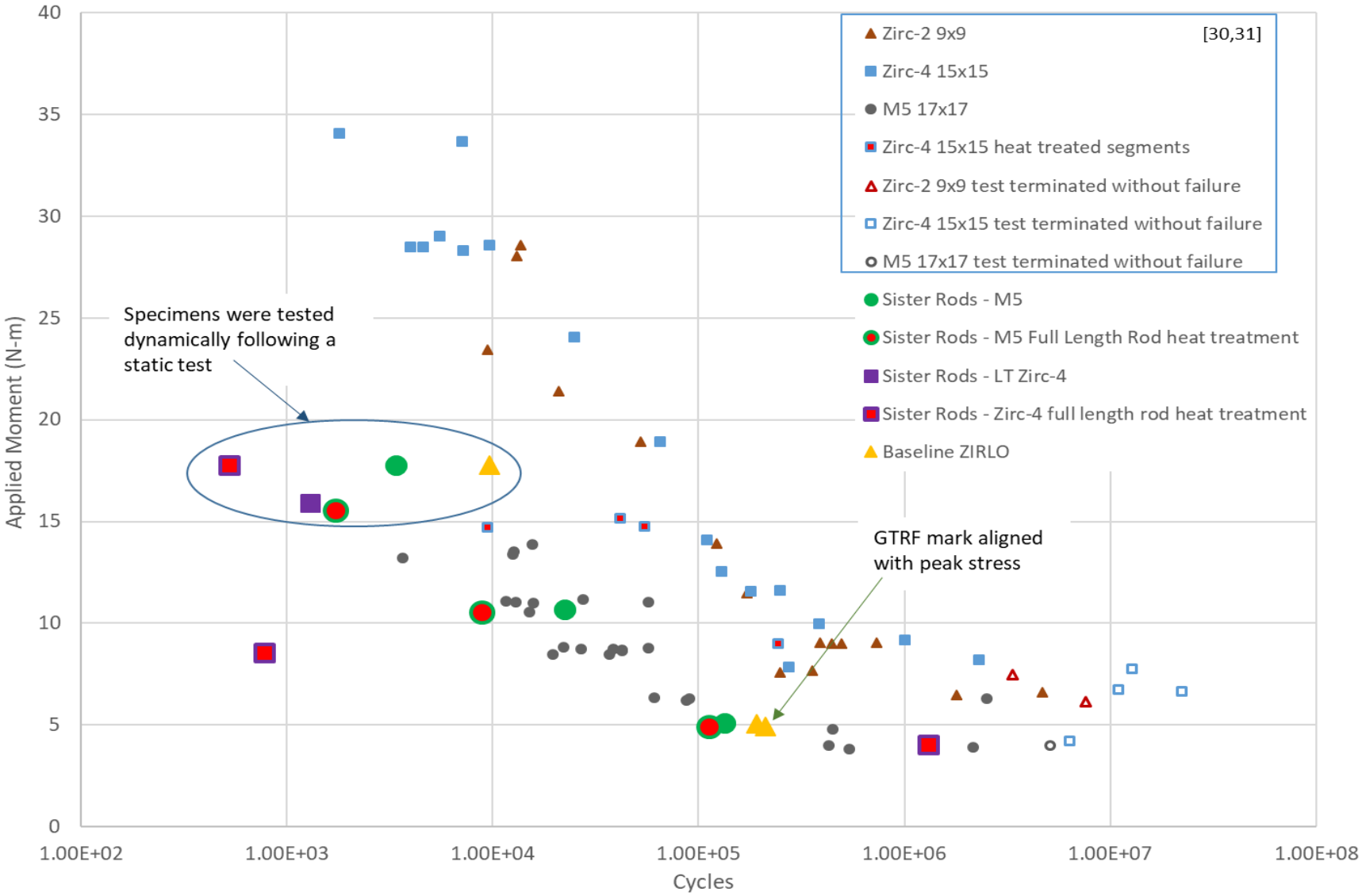

Figure 36. Results of CIRFT Tests Completed to Date, Applied Moment vs. Cycles to Failure.

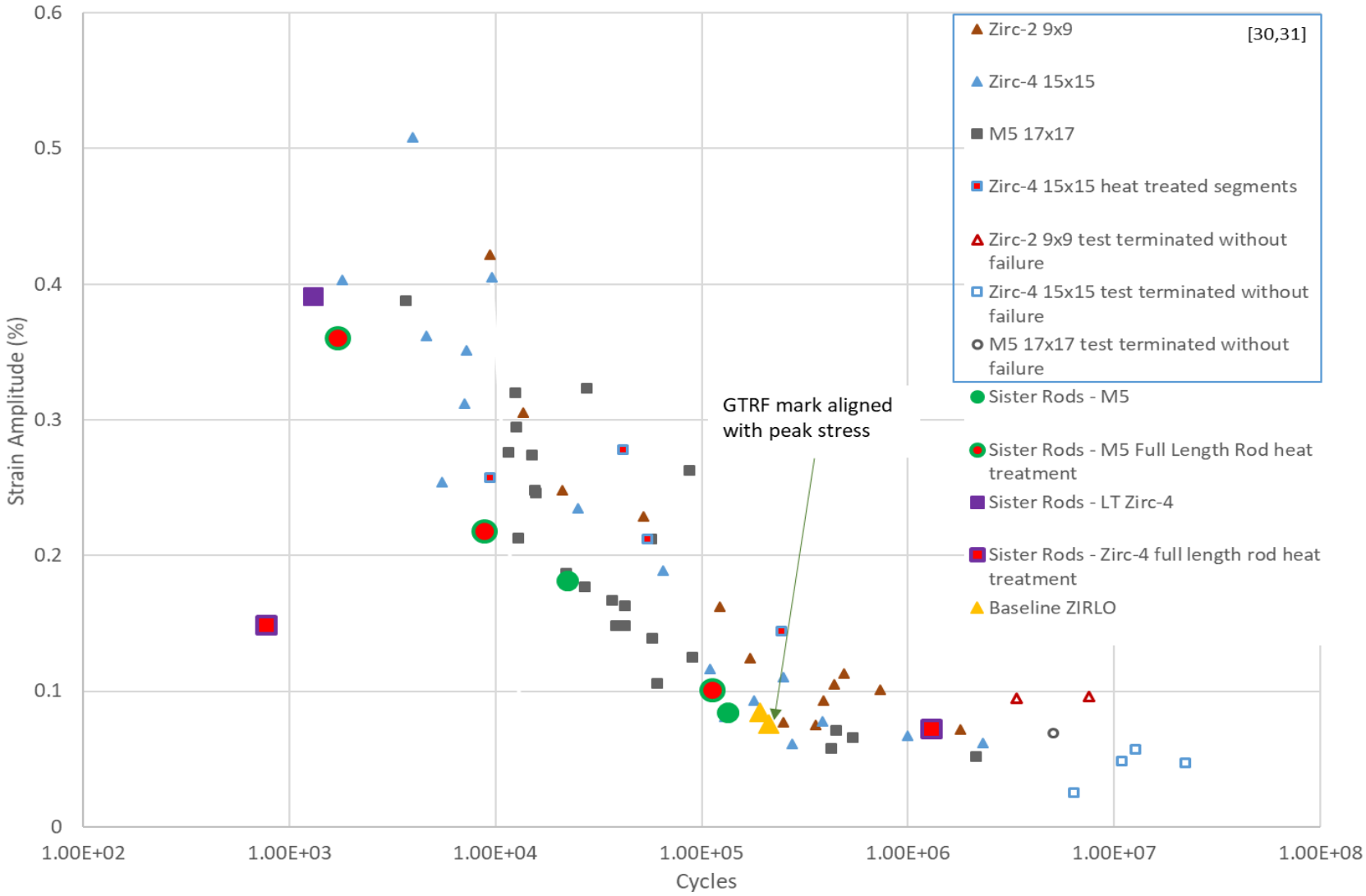

Figure 37. Results of CIRFT Tests Completed to Date, Strain Amplitude vs. Cycles to Failure.

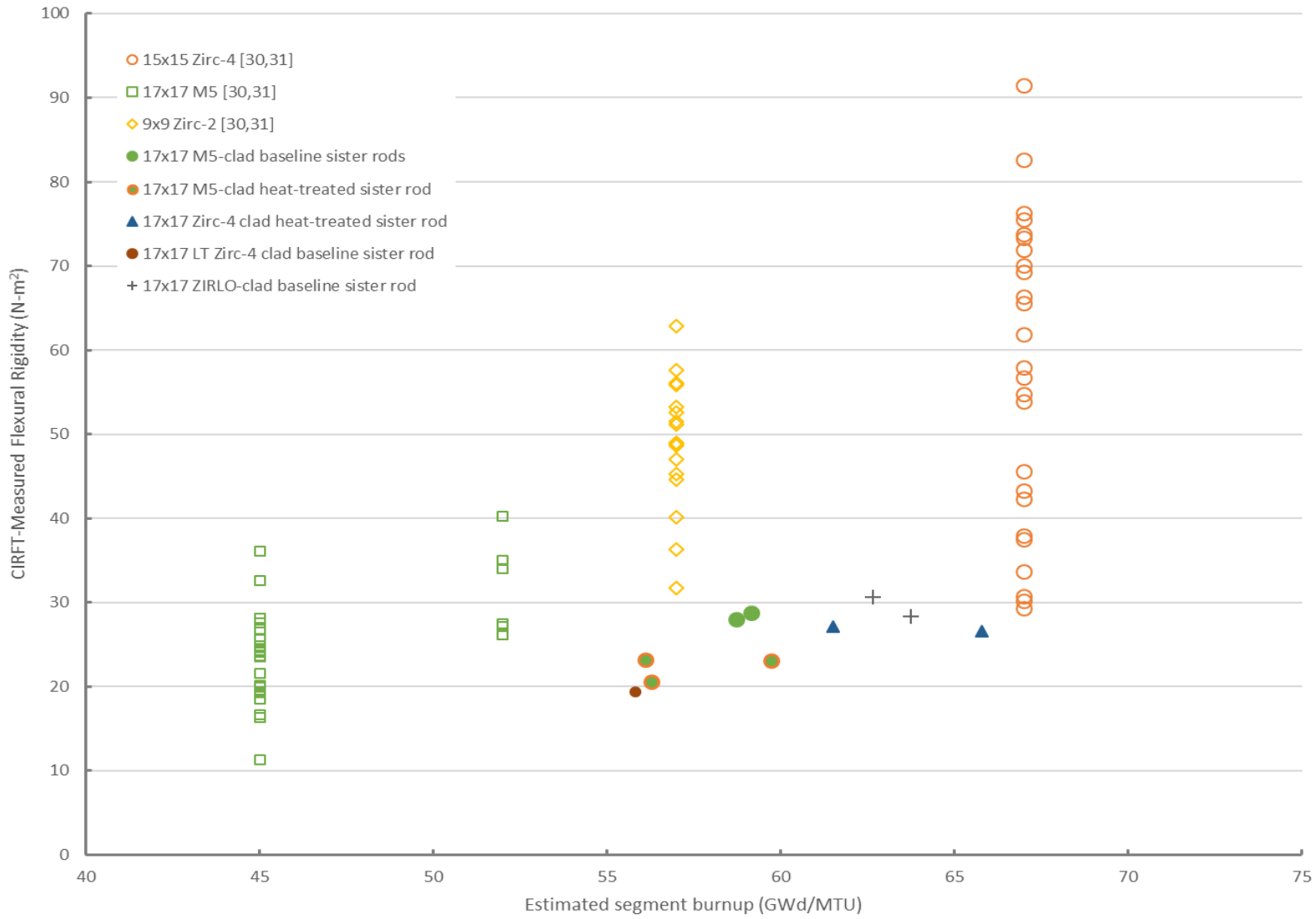

Figure 38. CIRFT-Measured Flexural Rigidity of the Sister Rod Segments Tested as a Function of Estimated Segment Burnup Plotted with Previous CIRFT Data.

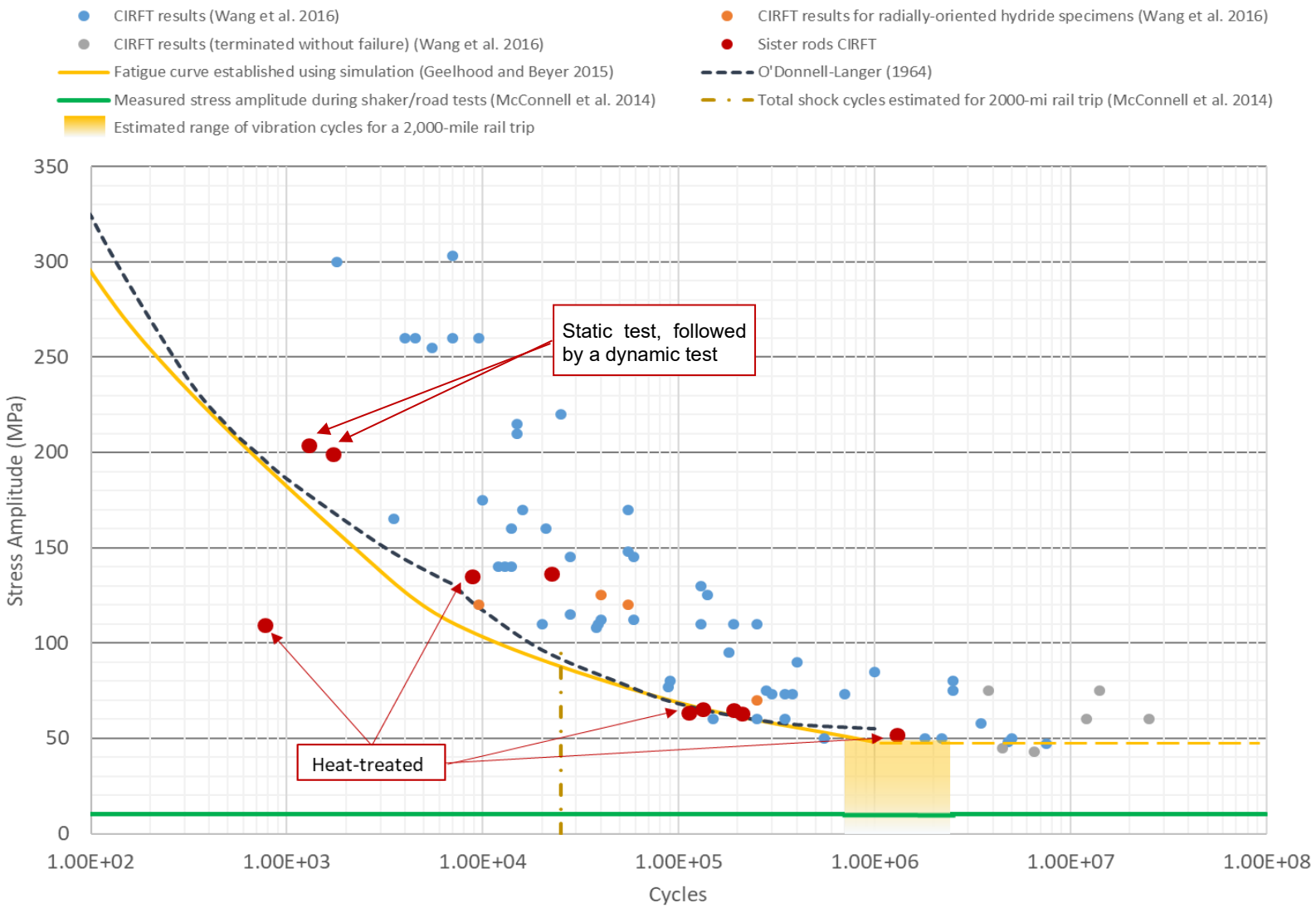

Figure 39. Stress amplitude as a function of cycles to failure for the sister rods.

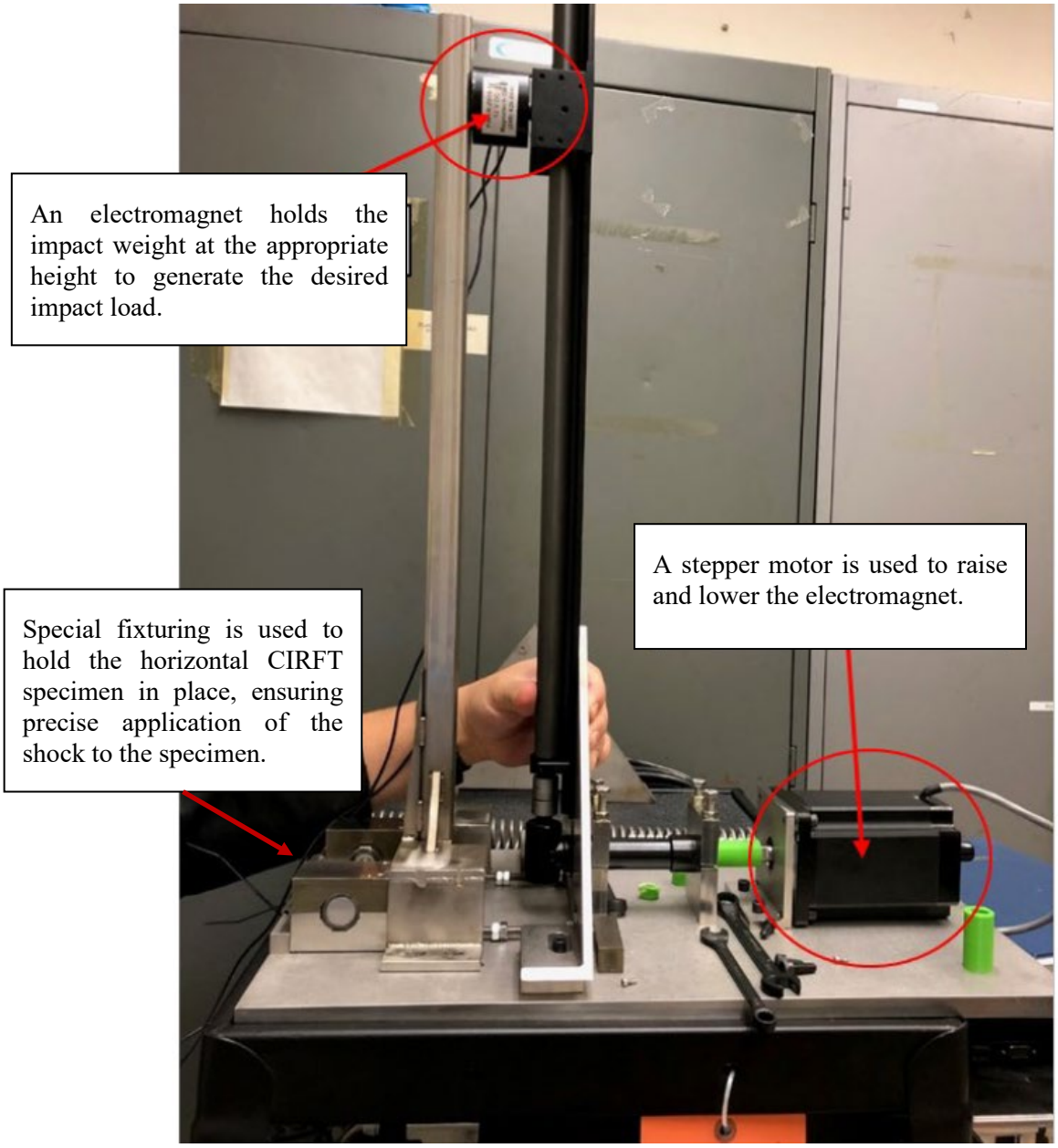

Figure 40. Cumulative Shocks Will Be Applied to CIRFT Specimens Prior to Fatigue Testing to Simulate the Normal Transport Condition Vibrations of a Fuel Rod against Its Fuel Assembly Spacer Grid.

This page is intentionally left blank.

11. FOUR-POINT BEND TESTS (DE.07)

The rough-cut segments can be used directly for four-point bend tests, and specimens are therefore ready to test. The tests will be completed on the Instron load frame, which is being prepared for insertion into the hot cell. Both room temperature and 200°C tests are planned. Four-point bend testing is expected to begin in FY2020, following the RCTs.

12. AXIAL TENSION TESTING (DE.08)

To perform axial tension testing, a small amount of fuel must be dissolved from each end to allow for insertion of a grip. The grip is used to prevent crushing of the specimen at the load point. Therefore, while the rough-cut segments are available, they must be further processed to prepare them for the test. The tests will be completed on the Instron load frame, which is being prepared for insertion into the hot cell. Both room temperature and 200°C tests are planned. Axial testing is expected to begin as soon as the load frame is available in the hot cell.

13. MICROHARDNESS TESTS (DE.09)

Microhardness testing will be completed in a glove box, and the equipment needed for the work has been installed in the glove box. Specimens must be prepared for testing, which will commence once the priority METs are completed, as the microhardness preparation uses the same equipment and personnel. Both room temperature and 200°C tests are planned.

14. RING COMPRESSION TESTS (DE.10)

A significant body of data on cladding hydride reorientation and associated effects on cladding ductility has been developed by ANL over the last decade, with the most recent summary of results documented by Billone in 2018 [35]. Several baseline and heat-treated sister rod specimens have been shipped to ANL for cladding RCT.

ORNL will provide supplementary data on intact fuel rods (cladding and pellets). Rough cut segments can be used directly for fueled ring compression tests, and specimens are therefore ready to test. The tests will be completed on the Instron load frame, which is being prepared for insertion into the hot cell. Room temperature tests are planned and are expected to follow the axial tension testing in FY2020.

15. BURST TESTS (DE.14)

No progress has been made on configuring the available equipment for burst tests.

16. SUMMARY OF RESULTS

Table 17 provides a summary of the testing completed to date and give details on the tests that still need to be completed. The planned DEs include full-length rod heat treatments simulating dry storage cladding temperatures, rod internal pressure and void volume measurements, fission gas analysis and release ratios, fuel burnup, gas transmission testing, metallography, cladding total hydrogen measurements, four-point bend and axial tension tests, microhardness tests, ring compression tests, and burst tests. The mechanical testing will be performed using fueled segments and is expected to complement previous and current mechanical test results using defueled cladding segments.

Table 17. DE Status

Planned DE		Status	Comments
FHT	Heat treat whole rods to 400°C, cool at ≤5°C/hr 1 ZIRLO, 1 M5 and 1 Zirc-4 rod	Complete	Three fuel rods have been heat-treated: one Zirc-4-clad (F35P17), one ZIRLO-clad (3F9N05), and one M5-clad (30AE14) rod. The target heat-up rates, soak temperatures and times, and cool-down rates were successfully achieved with the exception of the spent fuel rod heat treatment oven (SFRHTO) Zone 1 for rod 30AE14 (the upper ~550 mm), which reached temperatures as high as 485°C for approximately 1.75 h during the thermal soak. 30AE14's Zone 1 average temperature during the soak period was 452°C. At the higher average temperature imposed, the pressure was ~7.6 MPa, about 8% higher than planned. The maximum pressure during the soak was estimated as 8.0 MPa at the 485°C peak temperature for ~1.75 h. The rod's temperature was corrected prior to cool-down, and cool-down was as expected.
RS	Segment 3 baseline and 3 FHT rods, and segment 1 additional ZIRLO rod to provide additional CIRFT specimens.	Complete	Initial test segments have been rough cut from 7 Phase 1 sister rods and placed into individual storage capsules. The segments are taken from the initial 4 baseline rods (1 of which provides additional ZIRLO CIRFT specimens only) and 3 heat-treated rods. The rough segments are stored in labeled aluminum capsules in the hot cell; they are not stored in an inert gas atmosphere. The segments are further sectioned in preparation for testing as needed.
DEF	Defuel segments for ANL	Complete	Twelve segments slated for testing at Argonne National Laboratory (ANL) have been defueled and shipped.
AERO	Collect aerosol particles released during selected tests	In progress	An aerosol collection system with fixturing and sampling devices was designed to characterize and quantify the respirable fraction of UO_2 particles released during rod fracture. The fixture is used in conjunction with four-point bend tests. The aerosol collection system is currently being tested out of cell and is expected to be ready for use when four-point bend tests begin.
DE.01	Measure internal pressure of 5 baseline and 3 heat treated rods	Complete	The rod internal pressure and the void volume available inside the rod were measured for 8 sister rods at room temperature, and all pressures are within the publicly available database envelope. There is a clear correlation between the post-irradiated rod internal pressure and the as-designed fill pressure. The fission gas partial pressure trends well with the rod average burnup. The pressure and void volumes measured are consistent for rods from the same fuel vendor. The product of the partial pressure of the

Planned DE		Status	Comments
			fission gas and the void volume, P_fV, is consistent from lab to lab for sister rods from the same assembly, except for the two rods from assembly F35. A comparison of P_fV indicates the ZIRLO-clad rods may have experienced some change in pressure, void volume, or both due to the heat treatment applied, but the M5-clad rods do not exhibit the same effects. Comparisons with predictions from fuel rod performance codes FAST and BISON indicate a tendency for FAST to underpredict pressure and BISON to overpredict pressure.
	Measure rod void volume of 5 baseline and 3 heat treated rods	Complete	Eight rods have been measured. All measured volumes are on the lower side of the publicly available database envelope but are consistent with other rods of their design type. Comparing the measured volumes of the baseline and heat-treated ZIRLO-clad rods, as well as the P_fV for all ZIRLO-clad sister rods, it appears that the heat treatment resulted in an increase in void volume. The heat-treated M5-clad rod is within measurement uncertainty of the baseline rod, and the heat-treatment did not appear to affect the void volume. No conclusions could be made about the effects of the heat-treatment on the Zirc-4-clad rod based on a comparison with the LT Zirc-4 baseline rod or the PNNL Zirc-4-clad rod. Comparisons with predictions from fuel rod performance codes FAST and BISON indicate a tendency for FAST to overpredict void volume and BISON to underpredict void volume.
	Measure the transmissibility of gas along the pellet stack	Complete	Pellet stack gas transmissibility at room temperature was measured using depressurization tests on eight rods and transmission tests on three rods. In all cases, gas was transmissible through the pellet stack at room temperature, requiring between 30 min and 24 h to reach equilibrium conditions, depending upon the pressure differential applied. The data correlates well using the Muskat-Poiseuille porous media method. The permeability of the pellet stack varied over less than an order of magnitude for this set of rods and may indicate some common feature about HBU fuel. Graphs of the data with burnup, lifetime maximum HDCI, and operating lifetime average assembly middle-of-cycle predicted fuel temperature appear to indicate that the derived permeability is correlated to fuel operating temperature and maximum HDCI but is not correlated to the rod average burnup. The permeability does appear to be closely related to the rod's manufacturer and it seems that the pellet

Planned DE		Status	Comments
			manufacturing process may be important in determining the permeability of the pellet stack. While the flow regimes associated with the pellet stack transmissibility did not change significantly for the heat-treated fuel rods, it appears that the heat treatments may have induced a shift to higher evaluated permeability. The role of the cladding in the resulting permeability shift is unclear.
	Collect fission gas samples and analyze	Complete	Fission gas samples have been collected and analyzed. Results are consistent with publicly available database. Code-predicted fission gas production is not available; therefore, the fission gas release ratio is not available. ORNL and Pacific Northwest National Laboratory (PNNL) fission gas analyses are consistent with one another, and the data are as expected when differences in fission gas partial pressure are considered.
DE.02	Perform optical microscopy (MET)	In progress	Fueled and defueled specimens are being prepared for MET views. The Phase 1 specimens have been cut and specimen preparation/polishing is in progress. Cladding/pellet views are available of 1 M5-clad baseline rod, 1 M5-clad heat-treated rod, 1 heat-treated ZIRLO-clad rod, and 1 heat-treated Zirc-4 rod. Although some of the views are not as polished as intended, it is possible to see the cladding hydrides and fuel pellet high burnup (HBU) rims. Radial hydrides are visible in the heat-treated M5 and ZIRLO cladding and some radial hydrides located at the cladding inner diameter may have nucleated at a pellet crack. Measurements of the waterside oxide, pellet-side oxide, remaining cladding thickness, and HBU pellet rim are provided for the specimens available.
DE.03	Measure hydrogen content	In progress	Specimen preparation is in progress, and it involves dissolving the fuel from the cladding. A dissolution column has been designed and installed in the Irradiated Fuels Examination Laboratory (IFEL) hot cell and 13 specimens have been defueled.
DE.05	Perform CIRFT tests to determine static, dynamic, and cumulative effects and fatigue lifetime	In progress	Tests using the Cyclic Integrated Reversible-Bending Fatigue Tester (CIRFT) were completed on 13 specimens. The preliminary results indicate that the baseline sister rod's fatigue lifetime is consistent with other rods of the same type that were tested in the past. The 17x17 sister rods fall on the lower side of the existing CIRFT database.

Planned DE		Status	Comments
			It appears that the heat treatments resulted in a shorter fatigue lifetime, as the results for the heat-treated rods resulted in a shorter fatigue lifetime for all three heat-treated test specimens. A test on a specimen with a grid-to-rod-fretting (GTRF) mark in the maximum strain location did not result in a reduced fatigue lifetime. A specimen having multiple pellet-pellet gaps will be tested to determine if they have an impact on the fatigue lifetime. The initial flexural rigidity measured for the sister rods are consistent with previously tested 17x17 specimens and do not appear to be a function of burnup, at least over the range of available data. Data reduction on the available test datasets is in progress. Specimens from other Phase 1 sister rods are being prepared. The cumulative effects test fixture is being evaluated out of cell.
DE.07	Conduct 4-point bend tests	Not started	The Instron load frame has not yet been installed into the hot cell. All preparatory activities, including calibration and verification tests are complete.
DE.08	Conduct axial tensile tests	Not started	The Instron load frame has not yet been installed into the hot cell. All preparatory activities, including calibration and verification tests are complete.
DE.09	Test for ASTM microhardness	Not started	The microhardness tester has been installed and is ready to begin testing. Specimen preparation is in progress.
DE.10	Conduct RCTs	Not started	The Instron load frame has not yet been installed into the hot cell. All preparatory activities, including calibration and verification tests are complete.
DE.14	Perform burst tests	Not started	The existing in-cell equipment that was proposed for this purpose was evaluated and it was found that it is not capable of reaching predicted burst pressures at the temperatures of interest. Additional equipment will need to be developed to perform in-cell burst tests on fueled specimens.

This page is intentionally left blank.

REFERENCES

1. *High Burnup Dry Storage Cask Research and Development Project: Final Test Plan*, contract no. DE-NE-0000593, Electric Power Research Institute, Palo Alto, California (2014).
2. Saltzstein, Sylvia, et al., *Visualization of the High Burnup Spent Fuel Rod Phase 1 Test Plan*, SAND2018-8042-O (2018).
3. Montgomery, R. A. et al., "Post-irradiation Examination Plan for High Burnup Demonstration Project Sister Rods," SFWD-SFWST-2017-000090 ORNL/SR-2016/708, Oak Ridge National Laboratory (2016).
4. Montgomery, R. A. et al., "Sister Rod Nondestructive Examination Final Report," SFWD-SFWST-2017-000003 Rev. 1 (M2SF-17OR010201021) / ORNL/SPR-2017/484 Rev. 1 (ORNL/SPR-2018/801), Oak Ridge National Laboratory (2019).
5. US Nuclear Regulatory Commission, Spent Fuel Project Office, Interim Staff Guidance 11 Revision 3, *Cladding Considerations for the Transportation and Storage of Spent Fuel*, SFST-ISG-11 Revision 3 (2003).
6. Fort, J. A. et al. *Thermal Modeling of Proposed TN-32B CASK for High Burnup Fuel Storage Demonstration Project*, FCRD-UFD-2014-000490 PNNL-24549 Rev.0 (2015).
7. Bourdiliau, B. et al., "Impact of Irradiation Damage Recovery During Transportation on the Subsequent Room Temperature Tensile Behavior of Irradiated Zirconium Alloys," *J. ASTM Int.*, **7**, No. 9 Paper ID JAI103006 (2010).
8. B. V. Cockeram et al., *J. Nucl. Mater*. **461**, 244–264 (2015).
9. NUREG-2125, Spent Fuel Transportation Risk Assessment, Final Report, 2014, pp. E21-22.
10. *End-of-Life Rod Internal Pressures in Spent Pressurized Water Reactor Fuel*, 3002001949, Electric Power Research Institute, Palo Alto, California (2013).
11. R.W. Shimskey et al. PNNL Phase 1 Update on Sister Rod Destructive Examination Results, SFD-SFWST-M2SF-19PN010201037, Pacific Northwest National Laboratory, September 2019 [pending release].
12. K. Geelhood, "Sister Rod Thermomechanical Modeling with FAST," PNNL-28224 (2018).
13. S. Stimpson, "Sister Rod Predictions of End-of-Life Rod Internal Pressure and Void Volume," ORNL/SPR-2019/1173 M4SF-19OR0102010210, Oak Ridge National Laboratory, (2019).
14. Park, S. D. et al., "Distribution characteristics of fission gas along the axial direction for an irradiated fuel rod of a pressurized water reactor (PWR)," *J. Radioanal. Nucl. Chem.* **298**, 679, (2013). https://doi.org/10.1007/s10967-013-2574-z.
15. Bandyopadhyay, G. T. A. Roberts, "Crack Healing and Strength Recovery in UO_2," *J. Am. Ceram. Soc*. **59**, 415 (2005), 419. 10.1111/j.1151-2916.1976.tb09508.x.
16. Cuta, J. M., S. R. Suffield, J. A. Fort, and H. E. Adkins, "Thermal Performance Sensitivity Studies in Support of Material Modeling for Extended Storage of Used Nuclear Fuel," Pacific Northwest National Laboratory, FCRD-UFD-2013-000257 PNNL-22646 (2013).
17. Muskat, M., "The Flow of Compressible Fluids Through Porous Media and Some Problems in Heat Conduction," *Physics* **5**, 71–94, (1934), doi: 10.1063/1.1745233.
18. Desgranges, L., M. Faure, and A. Thouroude, "A New Apparatus for Determination of the Void volume of a Fuel Rod Using the Double Expansion Method," *Nucl. Technol.* **149**, 14–21 (2005).

19. Dagbjartsson, S. J. et al., "Axial Gas Flow in Irradiated PWR Fuel Rods," TREE-NUREG-1158 (1977).

20. Calogivic, V., "Gas Permeability Measurement of Porous Materials (Concrete) by Time-Variable Pressure Difference Method," *Cement and Concrete Research* **25**. No. 5.1054–l062 (1995).

21. Rondinella, V. V. et al., "Measurement of Gas Permeability Along the Axis of a Spent Fuel Rod," Top Fuel 2015, Zurich, Switzerland (2015).

22. PWR Axial Offset Anomaly (AOA) Guidelines, Revision 1, EPRI, Palo Alto, CA, 1008102 (2004).

23. M.G. Balfour et al. "Corrosion of Zircaloy-Clad Fuel Rods in High-Temperature PWRs" Measurement of Waterside Corrosion in North Anna Unit 1, TR-100408 Tier 2, Research Project 2757-1, Westinghouse Electric Corporation for Electric Power Research Institute, March 1992.

24. Katco, S., "Fission-Product Yields from Neutron-Induced Fission," *Nucleonics*. **18** (11):201–208 (1960).

25. Speight, M. V., "A Calculation on the Migration of Fission Gas in Material Exhibiting Precipitation and Re-solution of Gas Atoms Under Irradiation," *Nucl. Sci. Eng*. **37**, 180–185 (1969).

26. Turnbull, J. A., "Distribution of Intragranular Fission Gas Bubbles in UO2 During Irradiation," *J. Nucl. Mater*. **38** (2), 203 (1971).

27. Topical Report on Reactivity Initiated Accident: Bases for RIA Fuel and Core Coolability Criteria, 3-1 – 3-9, EPRI, Palo Alto, CA, 1002865 (2002).

28. Laboratory BN National Nuclear Data Center. http://www.nndc.bnl.gov/.

29. Pan, G., et. al. "Performance Characteristics of High Burnup ZIRLO Cladding Fuel Rods," Proceedings of TopFuel/Global Fuel Performance Meeting, Seattle, WA (2019).

30. Wang, J.-A. and H. Wang, "FY 2017 Status Report: CIRFT Data Update and Data Analyses for Spent Nuclear Fuel Vibration Reliability Study, Revision 1," ORNL/SPR-2017/521, SFWD-SFWST-2017-000030/R1 (2017).

31. Wang, J.-A. and H. Wang, "Mechanical Fatigue Testing of High Burnup Fuel for Transportation Applications," NUREG/CR-7198/R1 (2017).

32. W. J. O'Donnell and B. F. Langer, Fatigue Design Basis for Zircaloy Components, Nuclear Science and Engineering, Vol. 20, pp. 1-12, 1964.

33. P. McConnell et al. "Normal Conditions of Transport Truck Test of a Surrogate Fuel Assembly," SAND2014-20495/FCRD-UFD-2014-000066, Revision 0.1, Sandia National Laboratory, December 2014.

34. K. Geelhood et. al. "Modeling Structural Loading of Used Nuclear Fuel under Conditions of Normal Transportation," Ceramic Materials for Energy Application IV, The American Ceramic Society, 2015.

35. M.C. Billone. "Ductility of High-Burnup-Fuel ZIRLO™ following Drying and Storage," ANL-19/14, M2SF-19AN010201011 Rev. 3, Argone National Laboratory, June 30, 2019.

36. Juan J. Serna et al. "Experimental Observations on Fuel Pellet Performance at High Burnup," Journal of Nuclear Science and Technology, 43:9, 1045-1053, 2006.

37. S.D. Park et. al. “The measurement of compositions and the isotopic distribution of relased fission gas in the fuel rods of pressurized water reactors (PWR) of Korea,” Journal of Radioanalytical Nuclear Chemistry, 284:287-295 (2010).

38. Yu. K. Bibilashvili et al. “Development of the Fission Gas Behaviour Model in the START-3 Code and its Experimental Support,” Seminar Proceedings, Fission Gas Behaviour in Water Reactor Fuels, Cadarache, France, 2000.

This page is intentionally left blank.

Appendix A Puncture System: System operation, System Testing, Test Protocol Parameters, and Experimental Uncertainty Quantification

A rod internal pressure and void volume measurement system was developed specifically for the sister rod application. The system was optimized for the sister rods and the ORNL IFEL hot cell and was configured to accommodate the F35 fuel rods, which were loaded in the ORNL hot cell backwards (due to the orientation they were loaded into the shipping container at the North Anna spent fuel pool). The system also incorporated the necessary equipment to perform gas transmission testing.

The system relies on the ideal gas law to measure rod internal pressure and rod void volume. The system is also used to collect a fission gas sample from the rod, and to test whether the fission gases can move freely through the pellet stack at room temperature. The following sections describe the system operation, system testing, the test protocol used, and establishes the method for quantification of the measurement uncertainties. Figure 11 in the main document specifies valve identification and system components. Figures A-1 and A-2 include photos and schematics of the system for reference.

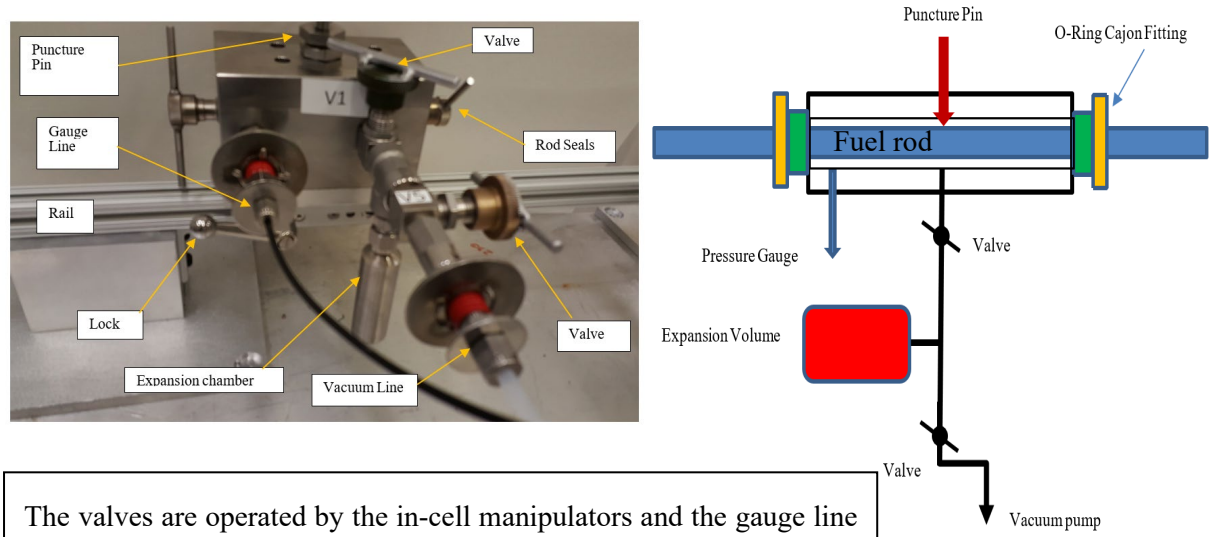

The valves are operated by the in-cell manipulators and the gauge line is a small-diameter, low-volume line that connects to a gauge outside the hot cell.

Figure A-1 Photo and Schematic of the In-Cell Portion of the Fuel Rod Puncture Apparatus.

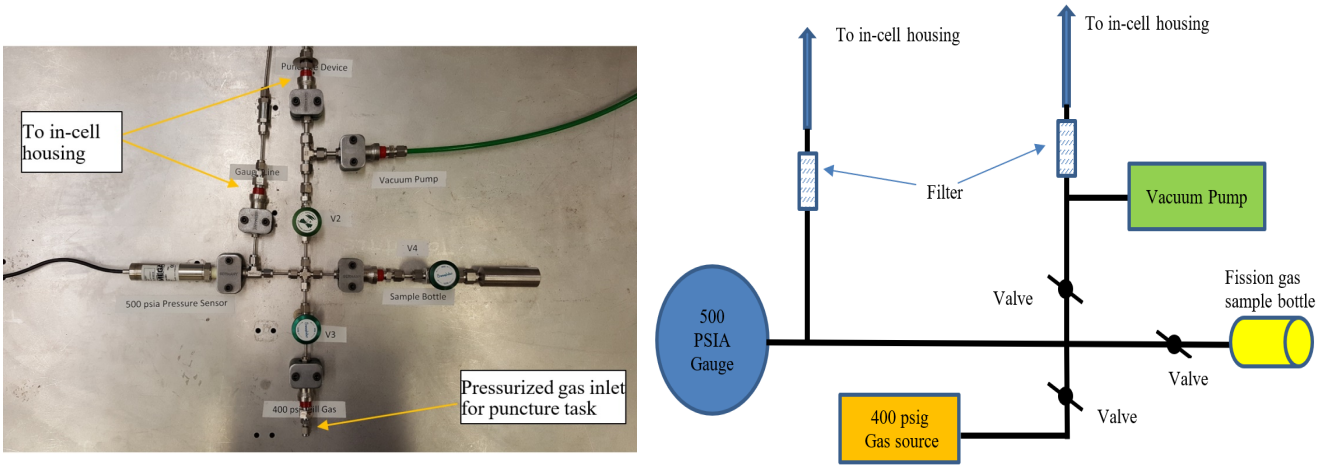

These valves are manually operated, and the pressure is computer-monitored. The operations are monitored by a radiation control technician during a puncture. The sample bottle serves as both a reference volume and a gas sample capture.

Figure A-2. Photo and Schematic of the Out-of-Cell Portion of the Puncture System.

A.1 Puncture System Operation and Calculation of Void volume and Pressure

Throughout the puncture process, gas is redistributed within the puncture system and the rod being punctured. It is necessary to pause at each redistribution event to allow for stabilization time. This is monitored at each gas redistribution event using the system gauge, and stabilization is considered to be achieved when the pressure change with time is small (<0.1 psig [0.7 kPa]) over a few seconds.

Step 1: Determine puncture system tare volume.

To determine the system's **tare volume**, V_t, (the volume of the apparatus and connecting lines), the fuel rod is inserted into the puncture unit and sealed by tightening the Cajon fittings. The system is then checked for leaks, both under vacuum and pressure.

Next, valves V1, V2, V4, and V5 are opened, and the system is pumped down to vacuum. Valves V1 and V2 are then closed, and V3 is opened, filling the fission gas sample bottle, the system connecting lines, and the clearance between the fuel rod and the puncture housing with inert gas at ~415 psia (2.86 MPa). The expansion volume, which was determined by previous out-of-cell measurements, and the vacuum pump are valved out of the system. Valves V3 and V4 are then closed, and the system pressure is recorded. V1 and V2 are then opened, and the system is pumped down to vacuum. Note that the fission gas sample bottle valve is not opened, and the recorded pressure is retained in the fission gas sample bottle's known volume. Once a stable vacuum is reached, V1 and V2 are closed. Finally, V4 is opened, expanding the known pressure and volume of inert gas from the fission gas sample bottle to the system volume. The system pressure is recorded after a few seconds, once the system has stabilized. Because the puncture unit and connecting lines are brought down to vacuum (except for sample bottle [V_s], which has a known volume), the moles of gas in the system at the sample bottle starting pressure (P_{st}) for a constant temperature are determined using the ideal gas law $PV = nRT$, as follows:

$$P_{st}V_s. \qquad \text{(A-1)}$$

When valve V4 is opened, the sample bottle's ending pressure P_{et} is lower because the gas expands to fill both the bottle and the tare volume (V_t) (constant temperature) so that the moles of gas in each volume sum to the total:

$$P_{st}V_s = P_{et}(V_s + V_t). \quad \text{(A-2)}$$

Solving gives

$$V_t = V_s\left(\frac{P_{st}}{P_{et}} - 1\right). \quad \text{(A-3)}$$

All sample bottles have known volumes measured prior to use.

Step 2: Collect puncture data

To puncture a rod, valves V1, V2, V4, and V5 are first opened to pump the system down to vacuum. Then all four valves are closed, and the sharp end of the puncture pin is slowly advanced to punch the rod cladding. Penetration is observed by a jump in system pressure; the pin is then backed out a small amount to allow an unimpeded gas path. Once the pressure stabilizes over several minutes or more, the pressure, P_{pun}, is recorded. Next, valve V1 is opened and the system pressure is allowed to stabilize over several minutes or more, usually longer than the first measurement. This new pressure, P_{exp}, is recorded. If the pressure is greater than 16 psia (0.11 MPa), then the punch pin is slowly unscrewed to allow gas to escape the puncture unit until the pressure is about 16 psia (0.11 MPa). The pin is then screwed back in, and the system is allowed to stabilize for much longer than the previous times, and this pressure is then recorded, P_{sys}. Valve V4 is then opened to capture a gas sample; when the pressure stabilized, it is recorded, P_{bot}.

At this point, there are enough data available to calculate the rod's void volume and internal pressure using the *double expansion* method. Since the puncture unit and connecting lines were evacuated, the moles of gas in the system at the rod volume V_p and the rod pressure P_p for a constant temperature are determined by:

$$P_pV_p. \quad \text{(A-4)}$$

When the rod is punctured, the pressure Pp drops as the gas expands to fill the tare volume (V_t), and the system pressure (constant temperature) drops so that the moles of gas in each volume sum to the total:

$$P_pV_p = P_{pun}(V_p + V_t). \quad \text{(A-5)}$$

When the valve V1 is opened to allow the gas to flow into the expansion volume (V_{exp}), the pressure drops even more, resulting in:

$$P_pV_p = P_{exp}(V_p + V_t + V_{exp}). \quad \text{(A-6)}$$

Equations A-5 and A-6 can be solved for P_p and V_p:

$$V_p = \frac{P_{exp}V_{exp}}{(P_{pun} - P_{exp})} - V_t, \text{ and} \quad \text{(A-7)}$$

$$P_p = \frac{P_{pun}(V_p + V_t)}{V_p}. \quad \text{(A-8)}$$

Step 3: Collect a fission gas sample for analysis

To capture a fission gas sample, first it is necessary to reduce the system pressure to ensure that the fission gas sample dose will be low enough for transfer outside the hot cell. To achieve this, the puncture pin is backed out of the housing enough to vent some of the fission gas to the hot cell's atmosphere as

previously noted. At a pressure reading of ~16 psia (0.11 MPa), which is slightly above local atmospheric pressure, the pin is again advanced into the housing to seal it, and the valve to the fission gas sample volume is opened. This low-pressure fission gas sample is expected to have the same mole ratio of gases as the original mixture contained within the fuel rod plenum, and the total number of gas moles can be calculated based on the measured total system volume and pressure.

When valve V4 is opened to the fission gas sample bottle at constant pressure and temperature, the moles of gas are distributed via the volume fraction. When the pressure is bled off, the amount in the bottle is the fraction of the new pressure over the original pressure. This gives

$$F = \frac{V_s}{(V_p+V_t+V_s+V_{exp})}\frac{P_{sys}}{P_{exp}} \tag{A-9}$$

Step 4: Perform the two-step method to measure the rod void volume

As a complementary measurement to the double expansion method outlined above, after the rod has been punctured and the fission gas has been removed, the rod's volume can be determined in a manner similar to that used to measure the tare volume. The tare volume and fuel pin's void volume (V_p) are evacuated. A fission gas sample bottle (V_s) is pressurized with an inert gas (P_{sp}), and the number of moles for a constant temperature is

$$P_{sp}V_s. \tag{A-10}$$

When the valve to the rest of the puncture system is opened, the inert gas expands to fill the tare volume and the spent fuel rod's void volume. Using the ideal gas law (assuming constant temperature), the relationship between the starting and ending pressures can be related to the system volumes of interest, as follows:

$$P_{sp}V_s = P_{ep}\left(V_s + V_p + V_t\right). \tag{A-11}$$

Solving gives

$$V_p = V_s\left(\frac{P_{sp}}{P_{ep}} - 1\right) - V_t. \tag{A-12}$$

Thus, using the two-step method eliminates some uncertainties from the measurement by eliminating the reliance on the measured puncture pressure in favor of the known inert gas pressure and by using the smaller fission gas sample bottle instead of the larger expansion volume. The rod's internal pressure is re-evaluated using the two-step method for rod internal volume:

$$P_p = \frac{P_{pun}(V_p+V_t)}{V_p}. \tag{A-13}$$

It should be noted, however, that the system's tare volume remains an important term in the calculation that must be specifically measured for each rod punctured. Additionally, incomplete evacuation of fission gas trapped within the fuel stack influences the result.

Note two steps are necessary before the equations can be solved: (1) first the fuel pin is punctured, and the puncture values are recorded, and then (2) the pin is backfilled to determine the volume, V_p. This two-step process contrasts with the double expansion method, which uses a second expansion to provide the information needed to determine both rod pressure and volume in a coupled system of equations. By using both methods, results can be checked for consistency and reduced uncertainty.

A.2 Puncture Device Behavior with a Fuel Rod

An example of fuel rod gas transmission behavior during the puncture phase can be seen by examining the pressure history of sister rod 3F9N05. As shown in Figure A-3, after puncture, the expansion of the gas in the plenum is relatively quick. The expansion of gas from the pellet stack is slower and some time is required until an equilibrium is reached. Next, the valve to the expansion chamber is opened, and the pressure quickly drops, followed by a slight rise in pressure as the pellet stack gas expands, with equilibrium requiring a noticeably longer time. After the punch is opened to relieve the gas pressure and then closed, the pressure slowly increases as more gas works its way through the stack over a much longer time. Finally, the valve to the sample bottle is opened, and allowed to reach equilibrium again. The final equilibrium state can be difficult to resolve, since, consistent with theory, the time constant is longer for the lower pressures. This demonstrates why it is advantageous to operate the system at the highest possible pressure, optimizing system volumes for uncertainty and rise times.

Two-Step Volume Measurement

An example of the time history for the Two-Step measurement is shown in Figure A-4. The sample bottle (reference volume) is filled to the working pressure. Because of the design of the unit, the fuel stack is also subjected to this pressure for a short period of time, and some of the argon gas moves into the pellet stack. The sample bottle is then valved off, and the system, including the pellet stack, is pumped down to vacuum. While it is difficult to see in Figure A-4, a couple of hundred seconds are required to draw the gas out of the stack. Note that for this step the pellet stack only sees the working pressure for a short time (minutes not hours) limiting the amount of gas penetrating into the stack and presenting less of a pump down challenge than if the system was pumped down from an equilibrium high pressure in the stack.

To perform the two-step volume measurement, the sample bottle valve was opened, and the gas flowed into the plenum and fuel stack. Note that it took 150 seconds or so for the system to come to equilibrium at 167 psia (1.15 MPa). By comparing the pressure immediately after the valve opening to the pressure after the system reaches equilibrium, one may be able to estimate both the plenum volume using the instantaneous pressure and the plenum-plus-pellet-stack volume using the equilibrium pressure if the pressure sensor valve combination can respond fast enough.

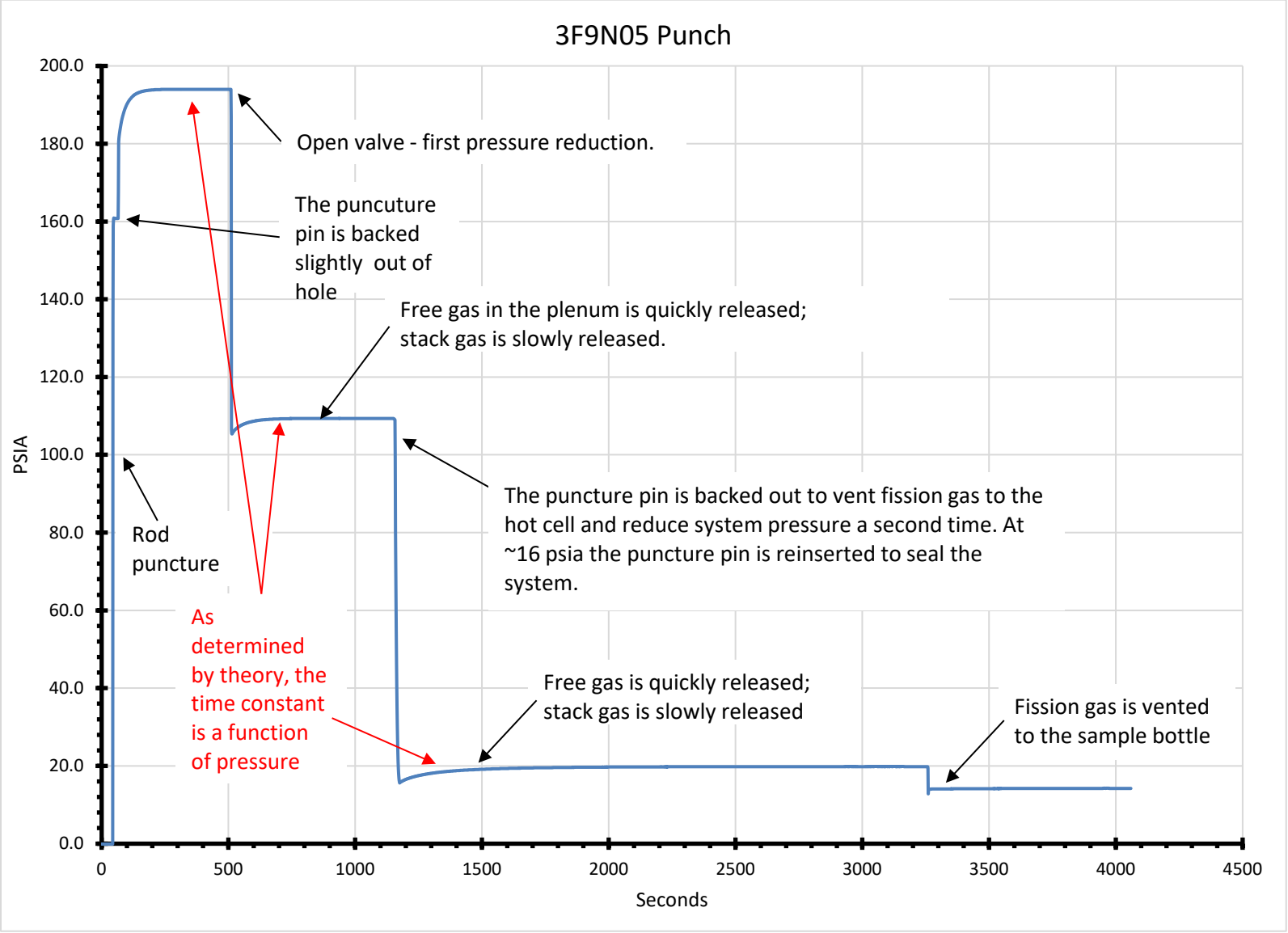

Figure A-3. Pressure History of a Rod Puncture.

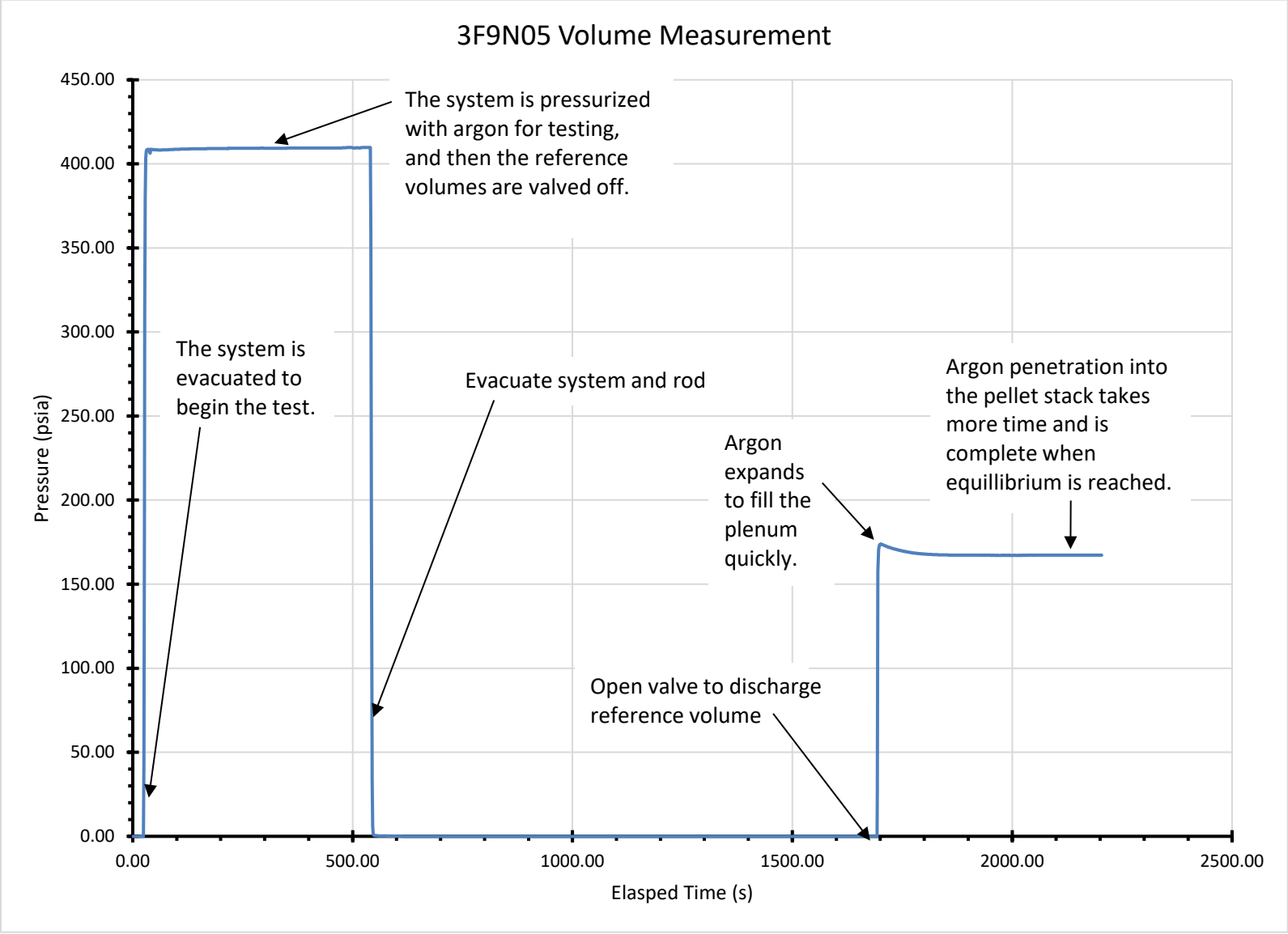

Figure A-4. Pressure History of a Rod using the Two-Step Method.

A.3 System Testing

The puncture apparatus was designed and fabricated using estimated design parameters. The as-fabricated apparatus is slightly different in actual measurement, but it is reasonably close so that the uncertainty estimates are not markedly different. The design goal was to achieve a 4–6% 2σ uncertainty range.

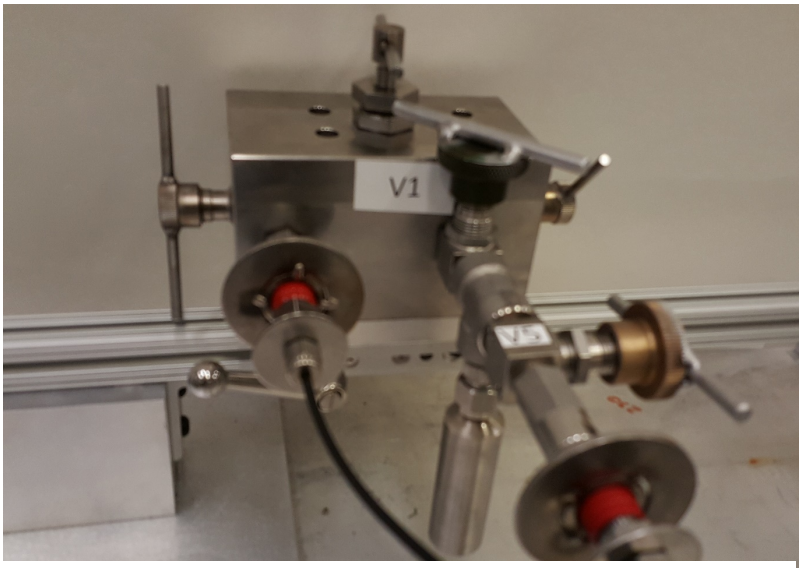

Figure A-5. In-Cell Portion of the Puncture Apparatus.

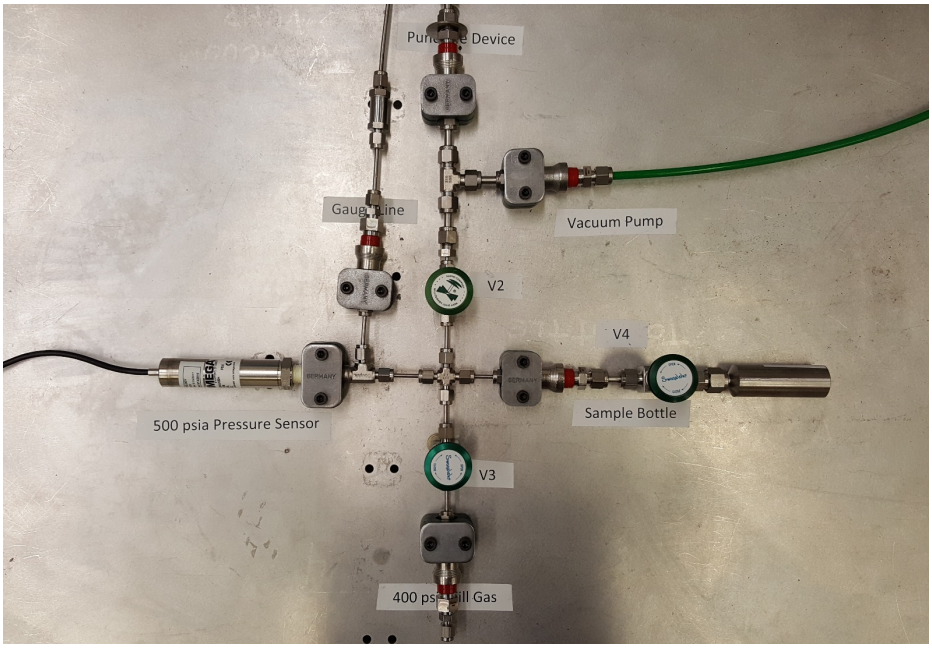

Figure A-6. Out-of-cell Portion of the Puncture Apparatus Containing the Control Valves, Pressure Sensor, and Sample Bottle.

As an example, the as-fabricated values for one set of reference volumes are:

V_{ref} = 26.1 cc Typical, several were used and transferred to the radiochemical laboratory
ΔV_{ref} = 0.21 cc
V_{exp} = 29.34 cc
ΔV_{exp} = 0.23 cc
V_{tare}= 25 cc Typical, varies with test
$P_{fill} \approx$ 400 psia (2.76 MPa) varied somewhat between tests, actual value used

The volumes of each reference volume were determined by filling the containers with water and weighing them 3 or more times. The volume of the expansion chamber was slightly refined by using the test rod specimens (see below) to reduce an unavoidable assembly tolerance.

To test the functionality of the system and to verify the uncertainty estimates, ORNL procured twelve stainless steel surrogate pins for puncture. The pins were all ⅜ inches in diameter and ranged in length from 7–10 inches to simulate the expected range of rod void volume. They were pressurized between 500–1,500 psia (3.45–10.34 MPa) to simulate the expected range of pressure using an inert gas. Five of the surrogates were punctured out of cell, and three others were punctured in cell. The remainder of the surrogate rods are held in reserve and will be used when additional punctures of the sister rods are completed to verify functionality of the system (see Table A-1).

Table A-1. Results of puncture apparatus testing.

Test	Fabricated pressure corrected for temperature (psia) <1%	Fabricated volume (cc) <1%	Measured volume, double expansion method (cc)	Volume difference, double expansion method	Measured pressure, double expansion method (psia)	Pressure Difference, double expansion method	Measured volume, two-step method (cc)	Volume difference, two-step method	Measured pressure, two-step method (psia)	Pressure difference, two-step method	Comments
Test01a	495	10.48	9.91	-5.4%	490	-1.1%	10.39	-0.9%	474	-4.4%	Lowest pressure
Test02	993	7.86	7.54	-4.1%	904	-9.0%	7.83	-0.4%	878	-11.6%	Smallest volume, suspect specimen leak
Test03	494	9.17	8.56	-6.7%	498	0.7%	9.22	0.6%	471	-4.7%	Lowest pressure
Test04	1,475	11.79	11.77	-0.2%	1,470	-0.3%	11.72	-0.6%	1,475	0.0%	Largest volume
Test05	987	11.79	11.42	-3.1%	982	-0.5%	11.76	-0.2%	962	-2.5%	Largest volume
Test06	1,474	7.86	7.83	-0.4%	1,505	2.1%	8.09	3.0%	1,467	-0.5%	Smallest volume
HT01	998	10.48	10.49	0.1%	972	-2.6%	10.59	1.0%	966	-3.2%	In hot cell
HT03	502	11.79	11.27	-4.4%	488	-2.7%	11.47	-2.7%	481	-4.1%	In hot cell
Test07	506	7.86	7.37	-6.2%	494	-2.2%	7.83	-0.3%	471	-6.8%	In hot cell

A-4 Experimental Uncertainty Associated with the Measured Rod's Internal Pressure and Void Volume Measurements

The 2σ uncertainty associated with the rod's internal pressure and void volume measurements can be estimated by taking the square-root-sum-squares (SRSSs) of the partial derivatives of the appropriate variable multiplied by its measurement uncertainty (negligible measurement correlation).

For example, for the uncertainty associated with the two-step rod void volume, V_p, the measurement can be evaluated as follows:

$$V_p = V_s\left(\frac{P_{sp}}{P_{ep}} - 1\right) - V_t, \tag{A-14}$$

$$\frac{\partial V_p}{\partial V_s} = \frac{P_{sp}}{P_{ep}} - 1, \tag{A-15}$$

$$\frac{\partial V_p}{\partial P_{sp}} = \frac{V_s}{P_{ep}}, \tag{A-16}$$

$$\frac{\partial V_p}{\partial P_{ep}} = -V_s\frac{P_{sp}}{P_{ep}^2}, \text{ and} \tag{A-17}$$

$$\frac{\partial V_p}{\partial V_t} = -1, \tag{A-18}$$

and the uncertainty of the rod void volume measurement can be estimated as

$$\Delta V_p = \left[\left(\frac{\partial V_p}{\partial V_s}\Delta V_s\right)^2 + \left(\frac{\partial V_p}{\partial P_{sp}}\Delta P_{sp}\right)^2 + \left(\frac{\partial V_p}{\partial P_{ep}}\Delta P_{ep}\right)^2 + \left(\frac{\partial V_p}{\partial V_t}\Delta V_t\right)^2\right]^{1/2}. \tag{A-19}$$

The pressure gauge accuracy, the volume of the fission gas sample bottle, and the system tare volume are significant factors within the equation. The form of the rod void volume uncertainty can be rewritten in terms of the parameters of interest:

$$\Delta V_p = \left[\left(\left(V_p + V_t\right)\frac{\Delta V_s}{V_s}\right)^2 + \left(\left(V_p + V_t + V_s\right)\frac{\Delta P_{sp}}{P_{sp}}\right)^2 + \left(\frac{\left(V_p+V_t+V_s\right)^2}{V_s}\frac{\Delta P_{ep}}{P_{sp}}\right)^2 + \left(\Delta V_t\right)^2\right]^{1/2}. \tag{A-20}$$

In this form, it can easily be observed that the system tare volume, the fission gas sample bottle volume, and the pressure gauge uncertainty are the primary parameters to be controlled and minimized in the design of the puncture system.

For the double expansion method, the uncertainty of the rod void volume measurement is different:

$$V_p = \frac{P_{exp}V_{exp}}{\left(P_{pun} - P_{exp}\right)} - V_t, \tag{A-21}$$

$$\frac{\partial V_p}{\partial V_t} = -1, \tag{A-22}$$

$$\frac{\partial V_p}{\partial V_{exp}} = \frac{P_{exp}}{\left(P_{pun} - P_{exp}\right)}, \tag{A-23}$$

$$\frac{\partial V_p}{\partial P_{exp}} = \frac{V_{exp} P_{pun}}{\left(P_{pun} - P_{exp}\right)^2}, \text{ and} \tag{A-24}$$

$$\frac{\partial V_p}{\partial P_{pun}} = -\frac{V_{exp} P_{exp}}{\left(P_{pun} - P_{exp}\right)^2}, \tag{A-25}$$

and the uncertainty of the rod void volume measurement can be estimated as follows:

$$\Delta V_p = \left[\left(\frac{\partial V_p}{\partial V_t}\Delta V_t\right)^2 + \left(\frac{\partial V_p}{\partial V_{exp}}\Delta V_{exp}\right)^2 + \left(\frac{\partial V_p}{\partial P_{exp}}\Delta P_{exp}\right)^2 + \left(\frac{\partial V_p}{\partial P_{pun}}\Delta P_{pun}\right)^2\right]^{1/2}. \tag{A-26}$$

Again, the uncertainty can be written in terms of the parameters of interest:

$$\Delta V_p = \left[(\Delta V_t)^2 + \left(\left(V_p + V_t\right)\frac{\Delta V_{exp}}{V_{exp}}\right)^2 + \left(\frac{\left(V_p+V_t\right)\left(V_p+V_t+V_{exp}\right)^2}{P_p V_p V_{exp}}\Delta P_{exp}\right)^2 + \left(\frac{\left(V_p+V_t\right)^2\left(V_p+V_t+V_{exp}\right)}{P_p V_p V_{exp}}\Delta P_{pun}\right)^2\right]^{1/2}. \tag{A-27}$$

By inspection, the important parameters to control and minimize are the expansion volume uncertainty, the system tare volume, and the pressure gauge uncertainty.

The uncertainty of rod internal pressure measurement, *Pp*, for both the double expansion and two-step methods is:

$$P_p = \frac{P_{pun}}{V_p}\left(V_p + V_t\right), \tag{A-28}$$

$$\frac{\partial P_p}{\partial P_{pun}} = 1 + \frac{V_t}{V_p}, \tag{A-29}$$

$$\frac{\partial P_p}{\partial V_t} = \frac{P_{pun}}{V_p}, \text{ and} \tag{A-30}$$

$$\frac{\partial P_p}{\partial V_p} = -P_{pun}\frac{V_t}{V_p^2}, \tag{A-31}$$

and the uncertainty of the rod internal pressure measurement can be estimated as

$$\Delta P_p = \left[\left(\frac{\partial P_p}{\partial P_{pun}}\Delta P_{pun}\right)^2 + \left(\frac{\partial P_p}{\partial V_t}\Delta V_t\right)^2 + \left(\frac{\partial P_p}{\partial V_p}\Delta V_p\right)^2\right]^{1/2}. \tag{A-32}$$

Rewriting in terms of the parameters of interest gives

$$\Delta P_p = \left[\left(\left(1+\frac{V_t}{V_p}\right)\Delta P_{pun}\right)^2 + \left(\frac{P_p}{(V_p+V_t)}\Delta V_t\right)^2 + \left(\frac{P_p V_t}{V_p(V_p+V_t)}\Delta V_p\right)^2\right]^{1/2}. \quad \text{(A-33)}$$

To design the puncture system with minimal uncertainty, the pressure gauge uncertainty and the system tare volume are important. Also, since the measured rod's void volume is included in the 2σ uncertainty, all of the terms associated with the rod's void volume must also be considered.

A.5. Selection of Puncture System Hardware to Achieve Functionality While Minimizing Measurement Uncertainty

Based on the system's uncertainty analysis (see section A.4), the system's tare volume must be minimized to reduce measurement uncertainty for the rod's internal pressure and void volume. However, the puncture system lines must reach from the fuel rod plenum location in the hot cell to the pressure gauge and sample bottles outside the cell, and the length of the tubing and valve volumes primarily dictate the required minimum system tare volume. Therefore, there is a lower limit to the system's tare volume associated with the cell requirements, and the expected tare volume is ~25 cc.

To select the appropriate sizes for the other critical system features—fission gas sample bottle, the expansion volume, the inert gas pressure, and the pressure gauge uncertainty—the terms within the uncertainty expressions were further expanded, and the sensitivity was evaluated.

For example, the uncertainty associated with the system tare volume, V_t, measurement can be evaluated as follows:

$$V_t = V_s\left(\frac{P_{st}}{P_{et}} - 1\right), \quad \text{(A-34)}$$

$$\frac{\partial V_t}{\partial V_s} = \frac{P_{st}}{P_{et}} - 1, \quad \text{(A-35)}$$

$$\frac{\partial V_t}{\partial P_{st}} = \frac{V_s}{P_{et}}, \text{ and} \quad \text{(A-36)}$$

$$\frac{\partial V_t}{\partial P_{et}} = -V_s\frac{P_{st}}{P_{et}^2}, \quad \text{(A-37)}$$

and the uncertainty of the system tare volume measurement can be estimated as

$$\Delta V_t = \left[\left(\frac{\partial V_t}{\partial V_s}\Delta V_s\right)^2 + \left(\frac{\partial V_t}{\partial P_{st}}\Delta P_{st}\right)^2 + \left(\frac{\partial V_t}{\partial P_{et}}\Delta P_{et}\right)^2\right]^{1/2}. \quad \text{(A-38)}$$

Rewriting in terms of the parameters of interest results in

$$\Delta V_t = \left[\left(V_t\frac{\Delta V_s}{V_s}\right)^2 + \left((V_s+V_t)\frac{\Delta P_{st}}{P_{st}}\right)^2 + \left(\frac{(V_s+V_t)^2}{V_s}\frac{\Delta P_{et}}{P_{st}}\right)^2\right]^{1/2}. \quad \text{(A-39)}$$

Noting that in practice, V_t is fixed, a reduction in the uncertainty measurement relies on a large starting pressure. The denominator of the expression generally includes the volume of the fission gas sample bottle, but it is also present in the numerator.

Therefore, to design the puncture device, the volumes V_s and V_{exp} were selected to minimize the uncertainties and to ensure that the before and after pressure readings would be in the gauge range. The tare volume of the apparatus and connecting lines were fabricated to be as small as practical.

Sensitivity studies varied for the fission gas sample bottle volume, the expansion volume, the inert gas pressure, and pressure gauge uncertainty to select an optimum combination for use in the puncture system. Based on the results of these sensitivity studies, the selected parameters for testing are as follows:

V_t = 25 cc (fixed based on tubing and valving requirements)

P_{st} = 400 psia (2.76 MPa)

$\Delta P_{sp} = \Delta P_{ep}$ = 0.4 psia (2.8 kPa)

V_s = 25 cc

ΔV_s = 0.01* V_s cc

Note that in a practical device, the actual value for V_s is a compromise value.

A.6. Estimated Time Required for Pumping Out the Rod

The boundary conditions for pumping out the rod are different because the vacuum pump is essentially an infinite sink at zero pressure. In this case, it is assumed that the fuel rod is being pumped out through the plenum side so that the volume of interest is the pellet stack volume, and the starting pressure is essentially the rod pressure. In that case, the equation developed for the rod transmission can be used, with the fixed pressure set equal to zero (See Eq. (B-4) in Appendix B).

The equation starts with

$$\frac{dP_2}{dt} = \frac{KA}{2\mu LV_2}(P_1^2 - P_2^2), \tag{A-40}$$

where V_2 is assumed to be the pellet stack volume, and P_2 is assumed to be the stack pressure. Setting P_1 equal to zero and dropping the subscripts gives

$$\frac{dP}{dt} = -\frac{KA}{2\mu LV}P^2, \text{ and} \tag{A-41}$$

integrating gives

$$\frac{1}{P} = \frac{KA}{2\mu LV}t + \frac{1}{P_{rod}}. \tag{A-42}$$

Finally,

$$P = \frac{P_{rod}}{1+\frac{P_{rod}KA}{2\mu LV}t}. \tag{A-43}$$

It is useful to estimate the time required to pump the rod down to 10% of the initial starting pressure:

$$\frac{10}{P_{rod}} - \frac{1}{P_{rod}} = \frac{KA}{2\mu LV}t, \tag{A-44}$$

$$t_{0.1} = \frac{18\mu LV}{KAP_{rod}}\ , \tag{A-45}$$

with:

$A = 5 \times 10^{-5}$ m^2,

$\mu = 2.4 \times 10^{-5}$ Pa •s,

$L = 4$ m,

$V = V_{stack} = 2 \times 10^{-6}$ m^3,

$P_{rod} = 2.8 \times 10^6$ Pa (lower pressure or fill for volume determination), and

$K = 2 \times 10^{-14}$ m^2,

resulting in a time of about 1,200 seconds. Note that this is once again a function of the rod pressure.

A-7. Estimating the Volume of Gas That Could Be Trapped in the Pellet Stack Following Pump-Down of the Rod

If the rod were to be pumped down and then switched into the both-chambers sealed mode, an estimate of the trapped gas can be obtained by monitoring the pressure increase using the primary equation for the gas flow:

$$\frac{dP_2}{dt} = \frac{KA}{2\mu LV_2}[P_1^2 - P_2^2]. \tag{A-46}$$

In this case, P_1 is the gas in the stack, and $P_2 \approx 0$. This results in an equation that is applicable over short time periods:

$$\frac{dP_2}{dt} = \frac{KA}{2\mu LV_2}P_1^2. \tag{A-47}$$

Solving for the stack pressure, P_1, gives

$$P_1 = \sqrt{2\frac{dP_2}{dt}\frac{\mu LV_2}{KA}}, \tag{A-48}$$

where

$A = 5 \times 10^{-5}$ m^2,

$\mu = 2.4 \times 10^{-5}$ Pa •s,

$L = 4$ M,

$V_2 = V_{apparatus} + V_p = (25+9) \times 10^{-6}$ M^3 $= 34 \times 10^{-6}$ m^3,

$K = 2 \times 10^{-14}$ m^2, and

$dP_2/dt = 0.01$*psi in 5 s = 13.8 Pa/s*,

resulting in about 3×10^5 Pa, or 44 psia, for the trapped pellet stack pressure, which indicates the minimum pressure change that can be reliable detected with the gauge and setup. Thus, at low pressure, it may be difficult to determine when the pellet stack is truly pumped down, as system outgassing or gauge limitations could mask this small measurement. The next section discusses how operating at high pressures with small volumes are used to mitigate this situation.

A-8. Effects on the Rod's Void volume Determination If There Is Gas Trapped in the Pellet Stack

The volume of the rod is often determined by evacuating it, backfilling it with a known volume at a known pressure, and then measuring the pressure of the combined system as detailed in above:

$$P_{fill}V_{ref} = P_{final}\left(V_{ref} + V_{rod} + V_{tare}\right), \text{ giving} \tag{A-49}$$

$$\frac{P_{fill}V_{ref} - P_{final}\left(V_{ref}+V_{tare}\right)}{P_{final}} = V_{rod}. \tag{A-50}$$

However, if some the gas were to remain trapped in the pellet stack due to incomplete pump down, Eqs. A-49 and -50 would become:

$$P_{fill}V_{ref} + P_{res}V_{stack} = P_{final}(V_{ref} + V_{rod} + V_{tare}), \text{ and} \tag{A-51}$$

$$\frac{P_{fill}V_{ref} + P_{res}V_{stack} - P_{final}(V_{ref}+V_{tare})}{P_{final}} = V_{rod}. \tag{A-52}$$

Where P_{res} is the unknown residual pressure left in the pellet stack and V_{stack} is the volume of the pellet stack (a fraction of V_{rod}). To estimate the impact of this residual pressure we can examine its incremental effect by taking the derivative of Eq. A-52:

$$\frac{\partial V_{rod}}{\partial P_{res}} = \frac{V_{stack}}{P_{final}} - \frac{\left(P_{fill}V_{ref}+P_{res}V_{stack}-P_{final}(V_{ref}+V_{tare})\right)}{P_{final}^2}\frac{\partial P_{final}}{\partial P_{res}}, \tag{A-53}$$

simplifying:

$$\frac{\partial V_{rod}}{\partial P_{res}} = \frac{V_{stack}}{P_{final}} - \frac{V_{rod}}{P_{final}}\frac{\partial P_{final}}{\partial P_{res}}, \text{ and} \tag{A-54}$$

Next,

$$\frac{\partial P_{final}}{\partial P_{res}} = \frac{V_{stack}}{(V_{ref}+V_{rod}+V_{tare})} - \frac{(P_{fill}V_{ref}+P_{res}V_{stack})}{(V_{ref}+V_{rod}+V_{tare})^2}\frac{\partial V_{rod}}{\partial P_{res}}, \tag{A-55}$$

and simplifying,

$$\frac{\partial P_{final}}{\partial P_{res}} = \frac{V_{stack}}{(V_{ref}+V_{rod}+V_{tare})} - \frac{P_{final}}{(V_{ref}+V_{rod}+V_{tare})}\frac{\partial V_{rod}}{\partial P_{res}}. \tag{A-56}$$

Combining Eqs A-54 and A-56,

$$\frac{\partial V_{rod}}{\partial P_{res}} = \frac{V_{stack}}{P_{final}} - \frac{V_{rod}}{P_{final}}\left[\frac{V_{stack}}{(V_{ref}+V_{rod}+V_{tare})} - \frac{P_{final}}{(V_{ref}+V_{rod}+V_{tare})}\frac{\partial V_{rod}}{\partial P_{res}}\right]. \tag{A-57}$$

Simplifying further:

$$\frac{\partial V_{rod}}{\partial P_{res}}\left[1 - \frac{V_{rod}}{(V_{ref}+V_{rod}+V_{tare})}\right] = \frac{V_{stack}}{P_{final}} - \frac{V_{rod}V_{stack}}{P_{final}(V_{ref}+V_{rod}+V_{tare})} \tag{A-58}$$

$$\frac{\partial V_{rod}}{\partial P_{res}}\left[1 - \frac{V_{rod}}{(V_{ref}+V_{rod}+V_{tare})}\right] = \frac{V_{stack}}{P_{final}}\left[1 - \frac{V_{rod}}{(V_{ref}+V_{rod}+V_{tare})}\right], \text{ and} \tag{A-59}$$

finally,

$$\frac{\partial V_{rod}}{\partial P_{res}} = \frac{V_{stack}}{P_{final}} = \frac{V_{stack}(V_{ref}+V_{rod}+V_{tare})}{(P_{fill}V_{ref}+P_{res}V_{stack})}. \tag{A-60}$$

Examining around P_{res}= 0 gives

$$\Delta V_{rod} \approx \frac{V_{stack}(V_{ref}+V_{rod}+V_{tare})}{P_{fill}V_{ref}}\Delta P_{res}. \tag{A-61}$$

Thus, a small, unaccounted-for residual pressure in the fuel stack results in an apparent increase in rod volume. For some typical values:

V_{stack} = 2 cc,

V_{ref} = 25 cc,

V_{tare} = 25 cc,

V_{rod} = 11 cc,

P_{fill} = 400 psia (2.76 MPa), and

P_{res} = 40 psia (0.28 MPa)– assume 10% trapped gas in pellet stack.

This gives 0.49 cc excess volume for an incompletely pumped down system. Note that an incompletely pumped down system results in an apparent increase in volume assuming enough time has been allowed for the system to be close to equilibrium. For these values, the uncertainty due to measurement (see previous sections) is about the same, so some target pump-down times, residual gas levels, and fill pressures can be seen. A large tare volume and a low fill pressure relative to the residual pressure makes the situation worse. Also, comparing the two-step and double expansion methods provides some indication of the success of the methods, as a much larger two-step volume would cast doubt on the efficiency of the pump-down for its volume measurement.

A-9. Impact of Different Rod and Reference Volume Temperatures

For the volume measurements, the fuel rod and tare volumes are pumped down to zero pressure, and the reference volume is filled to known pressure P_s. There may be a small difference between the hot cell and the operating area, so the temperature must be included when summing moles of gas. To perform the measurement, the valve is opened as described in the previous sections, and the system is allowed to come to equilibrium (see Figure A-7):

$$P_f\left(\frac{V_p}{T_p}+\frac{V_t}{T_t}+\frac{V_r}{T_r}\right)=\frac{P_sV_r}{T_r}. \tag{A-62}$$

Thus,

$$\frac{V_p}{T_p} =\frac{P_sV_r}{P_fT_r}-\left(\frac{V_t}{T_t}+\frac{V_r}{T_r}\right). \tag{A-63}$$

The case of interest is when T_p and T_t are about the same, and somewhat different from T_r. Thus,

$$V_p =T_p\left[\frac{P_sV_r}{P_fT_r}-\left(\frac{V_t}{T_t}+\frac{V_r}{T_r}\right)\right]=\frac{T_pP_sV_r}{P_fT_r}-V_t-\frac{T_pV_r}{T_r}=\frac{T_p}{T_r}\left[\frac{P_sV_r}{P_f}-V_r\right]-V_t. \tag{A-64}$$

Note that V_r is effectively increased by the temperature ratio

$$V_p =V_r\frac{T_p}{T_r}\left[\frac{P_s}{P_f}-1\right]-V_t. \tag{A-65}$$

Therefore, a first approximation correction to the temperature difference is to multiply the reference volume by the temperature ratio. A small temperature gradient will exist along the lines that connect the in-cell equipment to the out-cell equipment, but the volume of these lines is small compared to the other volumes.

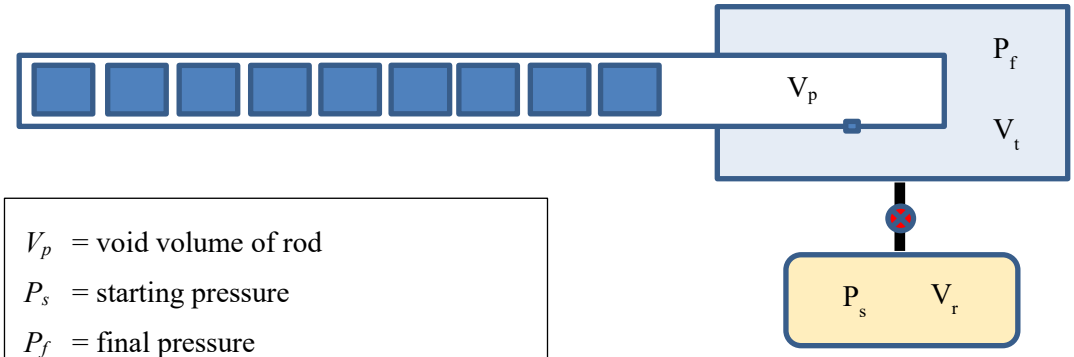

V_p = void volume of rod
P_s = starting pressure
P_f = final pressure
V_t = tare volume
V_r = reference volume
T_p = temperature of rod
T_t = temperature of tare volume
T_r = temperature of reference volume

Figure A-7. System Used to Estimate the Effects of Small Temperature Differences between the Fuel Rod in the Hot Cell and the Test Control Apparatus on the Outside.

Appendix B Depressurization and Gas Transmission Testing

B-1 Depressurization and Gas Transmission Test

The movement of gas through a fuel rod pellet stack can be modeled as a pressure source connected to one end of the fuel rod and a pressure-monitored fixed volume reservoir connected at the other end, with both ends open to the fuel stack, as shown in Figure 22. At the start of the gas transmission test, the reservoir end is at near zero pressure, and the source is essentially at a fixed pressure for the duration of the test (see Figure 22b). For the depressurization test, the reservoir end starts at a positive pressure, while the other end is at atmospheric pressure, and the reservoir is slowly discharged (see Figure 22c).

All rods undergo depressurization testing, as it is simple and is not expected to apply flow loads greater than that experienced during puncture. Following measurement of the rod's internal pressure and void volume, the rod is left sealed in the puncture housing. The rod is typically at ~170 psia (1.17 MPa) with argon after this test, and V1, V3, and V4 are closed (V4 had been open for an earlier test). The bottom end of the rod is then clamped in place, and the ADEPT saw is used to cut off the end of the rod approximately 5 mm above the end cap weld. The time vs. pressure is recorded until the pressure measured is near equilibrium. The end cap that was cut off is saved in a labeled container.

Only selected rods undergo gas transmission testing, as the differential pressure applied can be relatively large and may dislodge pellet particles. Following depressurization testing, a support is placed over the open bottom end of the fuel rod and clamped in place (see Figure B-1). The support includes a pressurizing unit with a large mechanical gauge that can be monitored through the hot cell window. A brace is placed at the top end of the rod to prevent any axial motion as the rod is pressurized (See Figure B-2).

Valves V1, V2, and V5 are opened to pump the system down, and the pressure to the support is turned on and adjusted. Valves V1, V2, and V5 are then closed. The pressure at the source end is monitored manually by viewing the mechanical gauge. The pressure in the rod plenum is recorded with time using the digital gauge until an equilibrium has been reached or until essentially full pressure is obtained.

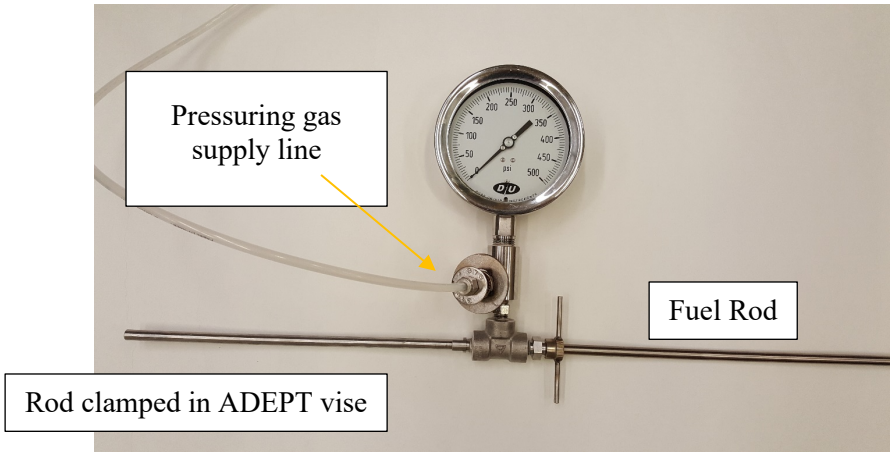

Figure B-1. Rod Inserted into the Gas Transmission Support Fixture with the Pressure Gauge and Pressure Supply Line.

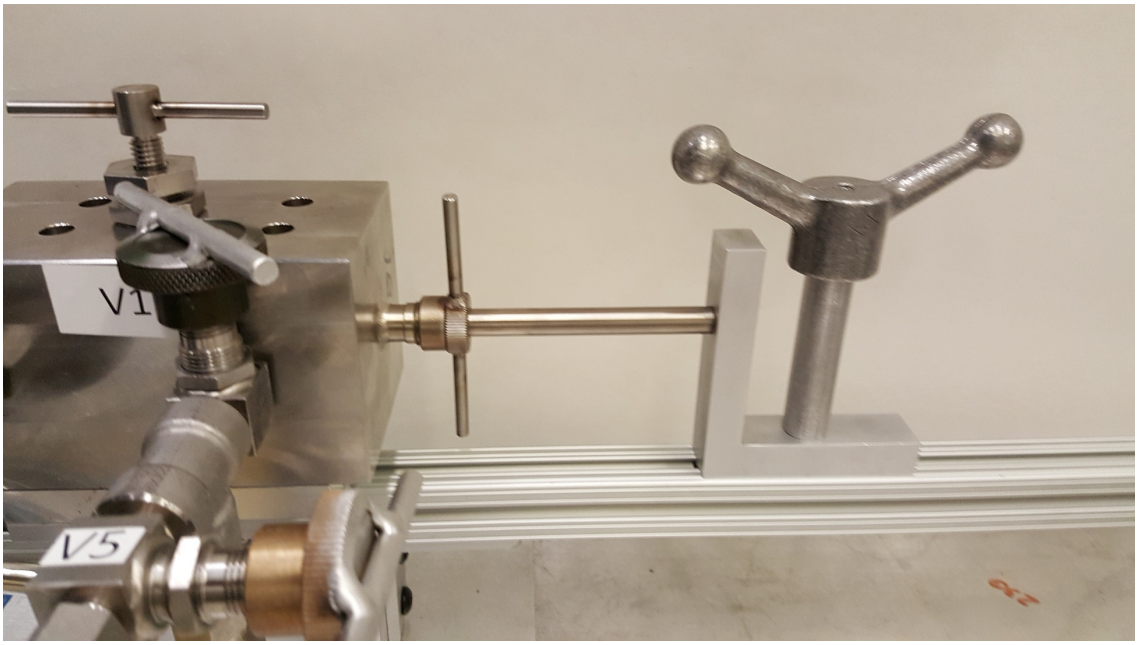

Figure B-2. Plenum End Support Brace in Place to Prevent the Rod from Moving Forward.

B-2 Depressurization and Gas Transmission Test Data Analysis and Fitting

The flow through the fuel rod is modeled as Muskat's application of Poiseuille flow through a porous media (see Section 7.2). This pressure-driving force is related to the difference between the squares of the two volumes' pressures; the steady-state mass flow solution for two connected reservoirs at different pressures and constant temperatures through a flow impedance is (constant pressure, steady state conditions) [15,16,17]:

$$\frac{dm_2}{dt} = \frac{KAM}{2\mu LRT}(P_1^2 - P_2^2), \tag{B-1}$$

where:

dm_2/dt mass flow rate into V_2 (Kg/s),
K permeability coefficient (m^2) for a homogenous medium,
A cross sectional flow area of the flow (m^2), in this application, the cross-sectional area of the space inside the fuel rod where the bulk flow is along the longitudinal axis of the rod,
M molecular mass of the gas (Kg/mol),
L length over which pressure drop occurs (m), in this application, the pellet stack length,
μ dynamic viscosity (Pa·s),
P_i pressure in volume i (Pa),
R gas constant, and
T temperature.

From the ideal gas law for Volume 2:

$$n_2 = \frac{m_2}{M} = \frac{P_2 V_2}{RT}. \tag{B-2}$$

Taking the derivative of Eq. (B-2) gives:

$$\frac{dm_2}{dt} = \frac{MV_2}{RT}\frac{dP_2}{dt}. \tag{B-3}$$

Combining Eqs. (B-1) and (B-3) gives us:

$$\frac{dP_2}{dt} = \frac{KA}{2\mu LV_2}(P_1^2 - P_2^2). \tag{B-4}$$

This can be integrated to give ($P_1 \neq 0$):

$$\frac{P_1 - P_2}{P_1 + P_2} = P_{0p}e^{-K\eta t}, \tag{B-5}$$

where P_{0p} is a constant of integration and $\eta = \frac{P_1 A}{V_2 \mu L}$. At $t=0$,

$$\frac{P_1 - P_2(t=0)}{P_1 + P_2(t=0)} = P_{0p}. \tag{B-6}$$

Finally,

$$P_2 = \frac{P_1\left(1 - P_{0p}e^{-K\eta t}\right)}{\left(1 + P_{0p}e^{-K\eta t}\right)}. \tag{B-7}$$

In Section 7-2 the Darcy solution (linear pressure differential) is mentioned for comparison to incompressible flow conditions. A derivation similar to that provided here for the Muskat-Poiseuille application can also be carried out but is not included here. Darcy's law provides a simple proportional relationship between the fluid flow rate and the pressure drop for an incompressible flow through a porous medium. In the case of the HBU fuel rod geometry, Darcy's Law is

$$Q = -\frac{K\,A\,(P_1 - P_2)}{\mu\,L}, \tag{B-8}$$

where:

Q is volumetric flow rate (m^3) or dV/dt,
K is permeability (m^2) of a homogenous porous medium,
A is the cross-sectional flow area of the flow (m^2), in this application, the cross-sectional area of the space inside the fuel rod where the bulk flow is along the longitudinal axis of the rod,
L is the length over which the pressure drop occurs (m), in this application, the pellet stack length,
μ is dynamic viscosity (Pa·s),
P_1 is pressure (Pa) in volume V1 (see Figure 22), and
P_2 is pressure (Pa) in volume V2 (see Figure 22).

Because Darcy's Law is only valid for single-phase incompressible laminar flows, it is not expected to produce a good fit for the HBU fuel rods. Darcy's Law solution is provided here for comparison.

The Darcy's Law solution to evaluate the permeability from the data is [18,19]:

$$P_2 = P_1 - (P_1 - P_2\ (t=0))e^{-K\eta t}. \tag{B-9}$$

B-3 Application to Sealed Rods

It is expected that most fuel rods will be sealed during transport. If road vibrations cause additional pellet cracking or pellet clad debonding which releases gas trapped in sealed voids or pores, the rod will no longer be at a constant equilibrium pressure, and gas will move from one end of the rod to another. This section presents further examination of the expected response given the proposed model.

If both end chambers are sealed, then the volumes are constant with time, and the total system moles do not change, even though the pressure can, thus resulting in (for constant temperature):

$$V_1P_1 + V_2P_2 = \mathbb{Z}. \tag{B-10}$$

This can be inserted into Eq. (B-4):

$$\frac{dP_2}{dt} = \frac{KA}{2\mu LV_2}\left[\left(\frac{\mathbb{Z}-V_2P_2}{V_1}\right)^2 - P_2^2\right] = \frac{KA(V_2^2-V_1^2)}{2\mu LV_1^2V_2}\left[P_2^2 - \frac{2\mathbb{Z}V_2P_2}{(V_2^2-V_1^2)} + \frac{\mathbb{Z}^2}{(V_2^2-V_1^2)}\right]. \tag{B-11}$$

Factoring gives:

$$\frac{dP_2}{dt} = \frac{KA(V_2^2-V_1^2)}{2\mu LV_1^2V_2}\left[P_2 - \frac{\mathbb{Z}(V_2+V_1)}{(V_2^2-V_1^2)}\right]\left[P_2 - \frac{\mathbb{Z}(V_2-V_1)}{(V_2^2-V_1^2)}\right], \tag{B-12}$$

or:

$$\frac{dP_2}{\left[P_2-\frac{\mathbb{Z}(V_2+V_1)}{(V_2^2-V_1^2)}\right]\left[P_2-\frac{\mathbb{Z}(V_2-V_1)}{(V_2^2-V_1^2)}\right]} = \frac{KA(V_2^2-V_1^2)}{2\mu LV_1^2V_2}dt\ . \tag{B-13}$$

Put into a form for integration:

$$\left\{\frac{1}{\left[P_2-\frac{\mathbb{Z}(V_2+V_1)}{(V_2^2-V_1^2)}\right]} - \frac{1}{\left[P_2-\frac{\mathbb{Z}(V_2-V_1)}{(V_2^2-V_1^2)}\right]}\right\}dP_2 = \frac{\mathbb{Z}KA}{\mu LV_1V_2}dt\ . \tag{B-14}$$

Integrating gives:

$$ln\left[P_2 - \frac{\mathbb{Z}(V_2+V_1)}{(V_2^2-V_1^2)}\right] - ln\left[P_2 - \frac{\mathbb{Z}(V_2-V_1)}{(V_2^2-V_1^2)}\right] = \frac{\mathbb{Z}KA}{\mu LV_1V_2}t - ln(-P_0)\ , \tag{B-15}$$

where P_0 is a constant of integration. Finally:

$$\frac{\left[\frac{\mathbb{Z}(V_2-V_1)}{(V_2^2-V_1^2)}-P_2\right]}{\left[-\frac{\mathbb{Z}(V_2+V_1)}{(V_2^2-V_1^2)}+P_2\right]} = P_0e^{-K\omega t}, \tag{B-16}$$

with

$$\omega = \frac{\mathbb{Z}A}{\mu LV_1V_2}. \tag{B-17}$$

Solving for P_2,

$$P_2 = \frac{\mathbb{Z}}{(V_2^2-V_1^2)}\frac{[(V_2-V_1)+(V_2+V_1)P_0e^{-K\omega t}]}{[1+P_0e^{-K\omega t}]}. \tag{B-18}$$

Note that for $V_1 \rightarrow \infty$, $\omega \rightarrow \eta$ as expected and Eq. (B-7) is recreated. P_0 can be determined from Eq. B-16 at $t=0$.

The case of most interest for the puncture application is when P_1 is the rod pressure, P_2 is the vacuum of a puncture unit, V_1 is the volume of the pellet stack, and V_2 is the volume of the rod plenum and puncture unit. This is the approximate situation a fuel rod is being punctured or when a volume measurement is being taken. In this case, a zero-dimensional approximation can be made for the starting condition by assuming that the rod's pressure and pellet stack interstitial volume is at the bottom of the rod, the pellets form the impedance path, the top plenum is punctured and instantly connected to the puncture apparatus, and the combined volume of the apparatus and plenum is at the now-expanded plenum pressure. The goal is to compute the approximate equilibrium time for the pellet stack to come to equilibrium with the plenum plus the apparatus pressure. Thus,

$$\mathbb{Z} = P_{rod}V_{stack} + P_{pun}(V_{apparatus} + V_p) \tag{B-19}$$

It is useful to estimate the time constant for parameters of interest:

$A = 5 \times 10^{-5}\ \mathrm{M}^2$

$\mu = 2.4 \times 10^{-5}$ Pa •s

$L = 4$ M

$V_1 = \mathrm{V}_{\mathrm{stack}} = 2 \times 10^{-6}\ \mathrm{M}^3$

$V_2 = \mathrm{V}_{\mathrm{apparatus}} + \mathrm{V}_{\mathrm{p}} = (25+9) \times 10^{-6}\ \mathrm{M}^3 = 34 \times 10^{-6}\ \mathrm{M}^3$

$P_{rod} = 4 \times 10^6$ Pa

$P_{pun} = 1.06 \times 10^6$ Pa

$Z = V_1 \times P_{rod} + V_2 \times P_{pun} = 2 \times 10^{-6}\ \mathrm{M}^3 \times 4 \times 10^6\ \mathrm{Pa} + 34 \times 10^{-6}\ \mathrm{M}^3 \times 1.06 \times 10^6\ \mathrm{Pa} = 44\ \mathrm{M}^3 \bullet\ \mathrm{Pa}$

$K = 2 \times 10^{-14}\ \mathrm{M}^2$

The time constant for a case in which all the stack volume is at the very end of the rod, away from the puncture point (it might be more reasonable to use half the rod length), is

$$T_c = \frac{\mu L V_1 V_2}{\mathrm{KA}\mathbb{Z}}, \tag{B-20}$$

or about 150 s, or just about 2.5 minutes for what might be considered the worst case; using half the rod length for the estimate gives half the time. Note that low system pressures and large apparatus volumes take much longer. Thus, taking rod measurements using the highest practical pressures and the smallest apparatus volumes is a goal.